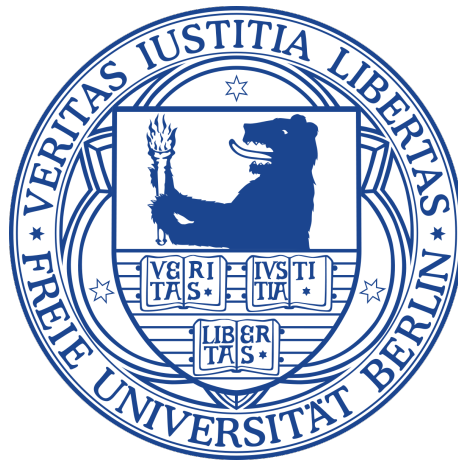


X-ray Absorption Spectroscopy of Transition Metal and Lanthanide Magnetic Molecules



Im Fachbereich Physik der Freien Universität Berlin
eingereichte Dissertation zur Erlangung des Grades eines
Doktors der Naturwissenschaften (Dr. rer. nat.)
vorgelegt von

Lucas Machado Arruda

Berlin, 2019

1. Gutachter: Prof. Dr. Wolfgang Kuch
2. Gutachter: Prof. Dr. Paul Fumagalli
Tag der Disputation: 27. Mai 2019

ABSTRACT

In this thesis the electronic, structural, and magnetic properties of metal complexes are studied, with a focus on the different properties that arise from their interaction with a variety of substrates. The thermal-activated ring-closure reaction that transforms octaethylporphyrin (OEP) metal complexes into tetrabenzoporphyrin (TBP) ones is investigated with x-ray absorption spectroscopy (XAS) and x-ray magnetic circular dichroism (XMCD) for different molecules composed of one of two metal centers, Fe or Co. The changes to the magnetic properties of the complexes are discussed as a result of their interaction with the different substrates (Au(111), Au(100), Cu(111), Cu(100), and graphene on Ni/W(110)). Spin-Hamiltonian formalism is applied in order to obtain further magnetic information about the ion and a comparison to density functional theory (DFT) is also done. The magnetic measurements, performed usually at a temperature $T = 4$ K and external field $B = 6$ T, evidenced clear modifications to the uniaxial anisotropy and magnetic moments of the molecules before and after the ring-closure reaction, as well as among the different substrates. The FeOEP uniaxial anisotropy changes from $D = 1.72$ meV to $D = 0.39$ meV within the plane of the molecules after the ring-closure reaction on Au(111), while the magnetic moment remains constant. In the CoOEP molecule the change is even more striking, with the spin magnetic moment being completely quenched after ring closure on the Cu(100) substrate. No spin moment is observed for either Co molecule when deposited on Cu(111).

The same techniques are applied to the study of another set of metal complexes, based on lanthanides. Two tris(tetramethylheptanedionate) ((TMHD)₃) molecules, with Dy and Er as lanthanide metal centers, were investigated. Sharp variation in the direction and intensity of the uniaxial magnetic anisotropy of the two molecules were identified on different substrates (graphene/Ir(111), graphene/Ni/W(110), HOPG (highly ordered pyrolytic graphite), and Au(111)), with no substantial variation in their magnetic moments. The flexibility of these molecules enables the quantization axis of their $4f$ orbitals to be rotated, depending on the substrate, so that the Dy molecule exhibits a quantization axis that lays parallel to the substrate when it is deposited on graphene/Ir(111), but rests at an intermediary position on the HOPG substrate, not fully parallel or perpendicular to it. For the Er molecule a similar situation is observed, this time with the substrates graphene/Ni/W(110) and Au(111).

KURZFASSUNG

In dieser Arbeit werden elektronische, strukturelle und magnetische Eigenschaften von Metallkomplexen untersucht, wobei der Fokus auf den unterschiedlichen Eigenschaften liegt, welche durch die Wechselwirkung mit verschiedenen Substraten hervorgerufen werden. Die thermisch aktivierte Ringschlussreaktion, welche Octaethylporphyrin (OEP) Metallkomplexe in Tetrabenzoporphyrin (TBP) umwandelt, wird mithilfe von Röntgenabsorptionsspektroskopie (X-Ray Absorption Spectroscopy, XAS) und zirkularem magnetischem Röntgen-Dichroismus (X-Ray Magnetic Circular Dichroism, XMCD) für unterschiedliche Moleküle mit einem Metallzentrum aus Eisen oder Cobalt untersucht. Die magnetischen Eigenschaften dieser Komplexe werden hinsichtlich ihrer Wechselwirkung mit verschiedenen Substraten (Au(111), Au(100), Cu(111), Cu(100) und Graphen auf Ni/W(110)) diskutiert. Ein Spin-Hamiltonian-Formalismus wird angewendet, um weitere magnetische Information über das Ion zu erhalten. Diese wird mit Ergebnissen aus der Dichtefunktionaltheorie (Density Functional Theory, DFT) verglichen. Die magnetischen Messungen, welche in der Regel bei einer Temperatur von $T = 4\text{ K}$ und einem externen Feld von $B = 6\text{ T}$ durchgeführt wurden, belegen klare Modifikationen der uniaxialen Anisotropie und des magnetischen Moments der Moleküle durch die Ringschlussreaktion sowie durch die verschiedenen Substrate. Die uniaxiale Anisotropie von FeOEP auf Au(111) ändert sich nach dem Ringschluss von $D = 1.72\text{ meV}$ zu $D = 0.39\text{ meV}$ mit leichter Richtung in der Ebene der Moleküle, während ihr magnetisches Moment konstant bleibt. Im CoOEP-Molekül ist der Unterschied sogar noch deutlicher, dort wird das magnetische Moment nach dem Ringschluss auf Cu(100) komplett unterdrückt. Auf Cu(111) wird für keines der Co-Moleküle ein Spinnmoment gemessen.

Die gleichen Techniken werden angewendet um ein weiteres Set an Metallkomplexen, basierend auf Lanthaniden, zu untersuchen. Zwei tris(tetramethylheptanedionate) ((TMHD)₃)-Moleküle, mit Dy oder Er als lanthanidischen Metallzentren, wurden untersucht. Starke Variationen der Richtung sowie der Intensität der uniaxialen magnetischen Anisotropie der beiden Moleküle wurden auf verschiedenen Substraten (Graphen/Ir(111), Graphen/Ni/W(110), HOPG (hochgeordnetes pyrolytisches Graphit) und Au(111)) gefunden, während ihr magnetisches Moment kaum Änderung zeigt. Die Flexibilität der Moleküle erlaubt es, die Quantisierungsachse ihrer $4f$ Orbitale zu drehen, so dass, abhängig vom Substrat, die Dy-Moleküle auf Graphen/Ir(111) eine Quantisierungsachse parallel zum Substrat aufweisen, während diese auf HOPG in einer Zwischenposition bleibt, weder parallel noch senkrecht. Für die Er-Moleküle wird eine ähnliche Situation beobachtet, diesmal mit den Substraten Graphen/Ni/W(110) und Au(111).

CONTENTS

Abstract	i
Kurzfassung	iii
Introduction	1
1 X-ray absorption spectroscopy of transition metals and lanthanides	9
1.1 Introduction	9
1.2 Interactions of x-rays with matter	9
1.2.1 Light-matter interaction events	10
1.2.2 The x-ray absorption cross section	14
1.3 X-ray absorption spectroscopy	17
1.3.1 X-ray natural linear dichroism	19
1.3.2 X-ray magnetic circular dichroism	22
1.3.3 Sum Rules	24
1.4 Ligand field theory	28
1.5 Spin Hamiltonian formalism	32
2 Experimental details	35
2.1 Introduction	35
2.2 Synchrotron radiation facilities	35
2.2.1 Generation of x-rays	37
2.2.2 Beamline Optics	40
2.3 VEKMAG	41
2.4 Sample preparation	45
2.4.1 Cleaning Au and Cu substrates	45
2.4.2 Cleaning Ir and W substrates	46
2.4.3 Graphene growth	47
2.4.4 Molecule deposition	49
2.5 X-ray absorption measurements	51
3 On-surface reaction of metalloporphyrin molecules	53
3.1 Introduction	53

Contents

3.2	Fe porphyrins	56
3.2.1	Fe porphyrins on Au(111)	56
3.2.2	Fe porphyrins on graphene	67
3.3	Co porphyrins	73
3.3.1	Co porphyrins on graphene	73
3.3.2	Co porphyrins on metallic substrates	77
4	Lanthanide magnetic molecules	91
4.1	Introduction	91
4.2	Dy(TMHD) ₃	94
4.3	Er(TMHD) ₃	107
	Conclusions	115
	Bibliography	119
	List of Acronyms	129
	List of Publications	131
	Acknowledgments	133
	Selbstständigkeitserklärung	135

INTRODUCTION

Magnetism has been a pivotal element in technology for centuries. The unique characteristics of the interactions between magnetic materials has led to many of the scientific breakthroughs in history, from the compass to magnetic storage devices. Lately, a large part of these new applications have been related to the latter, and a surge in scientific interest is directed towards the creation and improvement of these ever more minuscule apparatus and related technology. From this trend stemmed an interest in the magnetic properties of molecules, mainly for three reasons. The first is that the logical culmination of the size reduction in the magnetic domains of these devices is that one should arrive at the atom as the smallest entity capable of storing magnetic information. This, however, entails a strict separation between the magnetic properties of individual atoms involved, such that each can be tuned independently from the others as well as enabling its individual state to be read. This can be achieved by attaching the isolated magnetic atoms to additional non-magnetic ligands that act, in addition to other things, as a way to isolate the interatomic interactions between magnetic centers while stabilizing them on a surface. Secondly, the ligands allow for a direct way to tune the properties of the magnetic center that is not available for individual atoms or magnetic clusters. The tuning may enhance desirable magnetic properties or, ideally, reversibly modify the magnetic state of the molecule, thus enabling access to fast manipulation of magnetization. Finally, the use of magnetic molecules brings a simple and elegant answer to the difficulty of manufacturing the tiny devices, with the possibility of employing the self-assembly of the molecules into desirable macrostructures without the need for individually adding every building block of the final device. The molecules will often arrange themselves in near-perfectly-ordered structures that are ideal for precise spatial resolution required in technological applications.

The disadvantages of magnetic molecules must not be ignored, however, and must in fact be better understood in order to minimize their effects in technological applications. In this regard, one of the main disadvantages of the use of magnetic molecules is closely related to their main advantages. The high susceptibility of the ligands to manipulation and the strong dependency of the properties of the magnetic center to the ligand configuration leaves the overall magnetic properties of the molecules highly vulnerable to small modifications

of the outer ligands. Such modifications will more often than not come as a result of chemical reactions between the molecule and the environment, and raises doubts as to the long term applicability of these structures in magnetic devices. This is, however, a hurdle rather than a wall, and simply means that the final components of such devices must be constructed in a way that isolates them from undesired environmental interactions, either by making them inert to most common gas reactions or enclosing them in a controlled atmosphere. In other applications of magnetic molecules these interactions may be desired, such as magnetic-based sensors. In those cases the problem shifts to being able to either revitalize the molecules to their initial state or mass produce them in a significantly cheaper way in order to justify their limited lifetime.

The main obstacle in the deployment of magnetic molecules in technological applications at the moment, however, is their usually very low critical temperature, above which they lose their magnetic character. Advancements in this regard were achieved in 1991, when the synthesis of $V[TCNE]_x$, the first room-temperature molecular magnet, was reported [1]. This compound resulted in an instant reaction that produced a highly reactive to air and insoluble black powder. A low-temperature chemical vapor deposition (CVD) route was later developed, which allowed for the production of thin films of the amorphous material [2]. An all-organic spin-valve based on this material has been reported [3]. Magnetic bistability was achieved later with another class of magnetic molecules. The azo-functionalized porphyrin molecule in homogeneous solution [4] is reported to be reversibly switchable between two magnetic states at room temperature through light interaction. More recently, a series of publications has shown the use of magnetic molecules (Fe(Salen)) room temperature applications for simultaneous drug delivery and magnetic resonance imaging in cancer treatment [5, 6, 7].

The growth of the interest in magnetic molecules is in many ways related to the emergence of the field of spintronics. The idea that spintronics will revolutionize technology in a way akin to what happened with the advent of electronics is commonly held among the proponents of the field. In spintronics the electron's spin is an information carrier in addition to their charge. This, besides adding an important degree of freedom to the information carried by the electron, theoretically enables faster information transfer, as only the spin state information is required to travel, rather than the electrons themselves. It also points to a reduction in the energy dissipated in reading and writing a state, for the same reason. Magnetic molecules are perfect for spintronic applications because spin manipulation is the basis of their research since its early stages.

The research area aimed at exploring how the unique properties of the organic world can match the requirements of spin devices is called "Molecular spintronics" [8].

The magnetism of atoms and molecules has some peculiarities when compared to the magnetism of bulk materials. In these materials the magnetism usually comes from the combination of several magnetic domains that produce the final magnetization. The magnetism of an atom is generated by the motion of its electrons around the nucleus as well as the combination of their unpaired spins. This is the origin of the orbital and spin moment components of the magnetization of materials. In bulk and in molecules, however, this atomic high-spin state is easily quenched by the crystal field, the ligand field, or by bond formation between individual ions. The split of the energy levels of a transition metal in the presence of a ligand field, for instance (to be further discussed in Chapter 1), may break their magnetic high-spin state, if the ligand field is strong enough, leading to a reduction or complete quench of the magnetization in molecules that contain transition metals. This is not so relevant for other blocks of the periodic table, such as the lanthanides, since the ligand field is usually too weak to overcome the spin-orbit coupling. In order for magnetism to persist in complex structures, a fine balance between the external forces acting on the electrons and their natural repulsion needs to be reached. This fine balance is what leads to the various possibilities of molecular magnetism, where small modifications to the environment of the magnetic center lead to significant changes to the magnetic properties. It is one of the main reasons for the quick development of this field, as more unique molecules and systems are discovered, as well as more interesting reactions and interactions, with numerous applications, particularly in the emerging field of spintronics.

One aspect of atomic magnetism that results in significant magnetic properties lies in the presence of an exchange hole (or Fermi hole) in the effective density felt by the electrons that belong to the spin majority. Pauli's principle determines that electrons with the same spin orientation are forbidden from occupying the same region in space, which generates a repulsion between electrons with the same spin orientation, the exchange repulsion, in addition to the normal electrostatic one between charged bodies of the same sign. For a given spin-up electron, there is then a dip in the perceived electron density around it for spin-down electrons and vice versa. This is referred to as the exchange hole and it is not present in the spin density perceived between same-spin electrons. Due to this difference in perceived density, same-spin electrons do not shield themselves as well from the influence of the nucleus as different-spin electrons, resulting in a differential

shielding for those types of electrons in systems with unpaired spins. This entails that the majority spin species will experience on average less shielding from the nucleus than the minority spin species. The difference in perceived nucleus charge between the two spin species leads to variations in the energies of the orbitals associated with each of them [9]. The exchange splitting that results from this energetic difference also causes the lower-lying orbital to become less spatially diffuse than the higher-lying orbitals, which become less contracted. This theory can be applied to molecules as well as to atoms, and is useful in the understanding of the physical mechanism behind the preference for high-spin states in atoms and molecules, very important in molecular magnetism.

The first examples of studies focused on molecule-based magnetic systems are from the mid-20th century. These pioneering investigations sought to elucidate the magnetic properties of bulk materials composed of molecular building blocks. These materials mostly evaded the downside of molecular magnets relating to the environmental dependency of their magnetic properties, since they come from the interaction between the molecules' metallic centers, which are mostly protected by the bulk material. For the same reason they presented no immediate advantage over regular metallic bulk materials that were easier to produce with varying magnetic domain sizes for different applications. One of the first examples of these systems is the $\text{Fe}(\text{Diethyldithiocarbamato})_2\text{Cl}$, shown in Fig. 1(a). The crystal formed from this molecule displayed a $3/2$ spin and a ferromagnetic behavior below a temperature of 2.5 K. The unusual spin configuration of this iron complex, commonly found in either high- or low-spin states ($S = 5/2$ or $1/2$, respectively), was attributed in part to the changes in the ligand field induced by the low-symmetry C_{2V} configuration of the central iron ion in the bulk crystal.

An important breakthrough in magnetic molecules research came with the advent of single-molecule-magnets (SMMs). These compounds are characterized by the fact that their magnetic properties don't come from the long-range interactions between the individual molecules in the bulk material, but stem instead from within the single molecule itself and the interactions between the metal centers and the ligands. $\text{Mn}_{12}\text{O}_{12}(\text{O}_2\text{CPh})_{16}(\text{H}_2\text{O})_4$, shown in Fig. 1(b), is an example. This molecule was investigated in 1993 [11], while the first molecules of this type were synthesized in the 1980s [14]. It exhibits an unusually high total spin moment, $S = 10$, from the combination of the multiple manganese ions of the molecule, and has a high magnetic anisotropy. It is a very complex molecule, however, and the isolation of the individual molecules for deposition in different environments or substrates is not trivial, limiting their applicability.

In order to overcome these difficulties, simpler molecules with fewer central

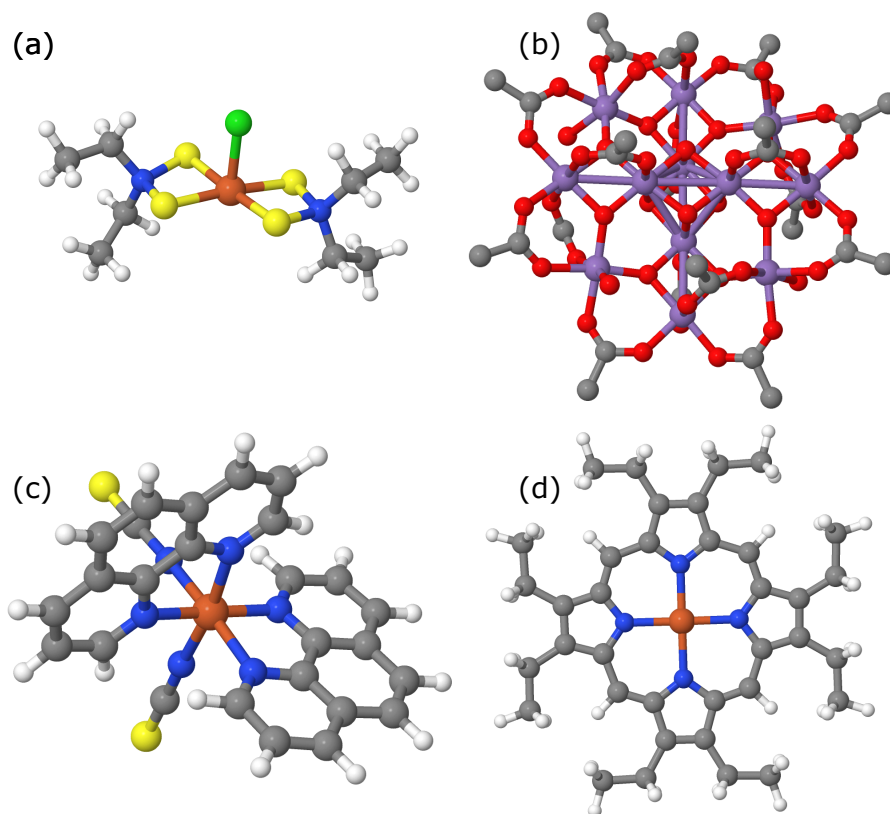


Figure 1: Magnetic molecules. The elemental composition is hydrogen (white), carbon (gray), nitrogen (blue), sulfur (yellow), chlorine (green), iron (orange), oxygen (red), and manganese (purple). a) $\text{Fe}(\text{diethyldithiocarbamate})_2\text{Cl}$ [10] b) $\text{Mn}_{12}\text{O}_{12}(\text{O}_2\text{CPh})_{16}(\text{H}_2\text{O})_4$ (hydrogens omitted) [11] c) $\text{Fe}(\text{phen})_2(\text{NCS})_2$ [12] d) FeOEP [13].

magnetic centers were synthesized in subsequent years, the trade-off being in the lowering of the spin moments in order to achieve a higher degree of control and flexibility in the molecules and their possible applications. Fig. 1(c) and (d) show two of the molecules that are the focus of active research in recent years. The first one is $\text{Fe}(\text{phen})_2(\text{NCS})_2$ [12], a spin crossover (SCO) molecule, meaning that it can be switched between high- and low-spin states through some external interaction, enabling magnetic switches on a molecular scale. Fig. 1(d) depicts the FeOEP molecule [13], one of the molecular systems studied in an upcoming chapter of this thesis. It is of high interest mainly given its high chemical flexibility and stability on single-crystal substrates. Both of these molecules can be thermally evaporated onto different substrates in order to study the distinct interactions between the molecules and the surfaces on which they are deposited.

The focus of this work is on molecular magnets deposited on crystalline substrates. The molecules' deposition onto the substrates and the experiments are performed under ultra-high vacuum conditions to ensure minimal contamination from gas particles. In order to understand predominantly the interactions between the substrate and the molecules, the molecular coverage is kept at submonolayer levels. Depending on the strength of the molecule-substrate interaction, the molecules will usually be able to migrate on the surface, leading in many cases to a natural arrangement of the molecules, the aforementioned self-assembly, where the individual magnetic molecules organize themselves into complex periodic structures on the crystalline surfaces. This is commonly referred to as the bottom-up approach, and is considered an attractive alternative to the usual top-down approach, where lithographic methods are employed in order to arrive at the desired structures. In addition to molecule-substrate interactions, on-surface reactions are employed as a way to alter the chemical structure and composition of some of the molecules, and the resulting changes to the magnetic properties of the molecules is discussed.

On-surface reactions are a promising way of modifying molecules and obtaining new molecular arrangements, frequently difficult or impossible to obtain otherwise. These reactions are usually irreversible [15, 16], be it an intermolecular reaction that forms new covalently bound macrostructures or intramolecular reactions resulting in new covalent bonds within the molecules. This can be an advantage, but only when the reaction processes are understood to the point one can control them to the required level of precision. These reactions often change the conformation of a molecule or molecular array [17, 18, 19, 20], leading to different electronic and magnetic properties, and depend on several different aspects of the system environment. It has been shown that different thermal conditions lead to alternative results on a surface [21], with intermolecular or intramolecular reactions being favored depending on the temperature of the substrate. The molecule-substrate interaction is another important factor. Experiments show that substrate atoms can act as components or catalysts of molecular reactions [22, 23, 24]. In the case of porphyrins, a class of molecules that will be discussed in an upcoming chapter, while the reactions and molecular arrangements of the molecules often do not depend on the central ion, the change caused by these factors and the substrate interaction affect strongly its magnetic and electronic properties [25, 26, 27, 28].

In this thesis, molecular systems will be investigated with x-ray absorption spectroscopy (XAS) and x-ray magnetic circular dichroism (XMCD) in order to ascertain their magnetic and electronic properties, particularly how these

properties vary with the change of the substrate the molecules are deposited on, and when the molecule itself is modified by means of intramolecular reactions activated by heat. A description of the required theoretical background of XAS and the magnetism of molecules is given in the first chapter. The following chapter describes the experimental methods and setups used throughout the experiments. Porphyrin molecules containing Fe (FeOEP) and Co (CoOEP) are investigated in the third chapter, with a focus on their transition to FeTBP and CoTBP, respectively, through a ring-closure reaction. The final chapter investigates the [TMHD]₃ class of molecules with two different lanthanide metal centers, Dy and Er. The modifications to the electronic configuration and magnetic moments experienced by the molecules investigated under different conditions is discussed with the application of the sum rules. The spin-Hamiltonian model is used to gain more information about their magnetization and these properties are compared to density functional theory in order to clarify their orbital occupation.

1

X-RAY ABSORPTION SPECTROSCOPY OF TRANSITION METALS AND LANTHANIDES

1.1 Introduction

The understanding of the physical properties that govern the interactions between individual molecules, bulk substrates, thin films, and electromagnetic fields requires the employment of several different topics of condensed matter and surface science fields. In this chapter I will give a background to some of the most relevant aspects of these topics, starting with the fundamentals of XAS and light-matter interactions, particularly when it relates to the magnetic properties of the materials studied. The field of magnetic molecules will then be presented with some of the historic and contemporary highlights in this field, as well as an introduction to molecular orbital theory. In the last section the spin Hamiltonian formalism will be introduced. It is a magnetic model that can help explain the configuration of the measured samples, in particular when it comes to the fit of the magnetization curves obtained from the experiments.

1.2 Interactions of x-rays with matter

Visible light interacts predominantly with the valence and free electrons of materials, given that their photons' low energy is unable to overcome the binding energy of core electrons. The higher-energy x-rays, however, are capable of interacting with these electrons, leading to a variety of phenomena that were not

possible before the advent of x-rays. Additionally, x-ray photons with an energy in the order of kiloelectronvolts (keV) have wavelengths comparable to the typical distances between the atoms of materials. This has encouraged the initial use of x-ray radiation as a diffraction tool to determine the crystallographic structure of various samples. The widespread use of x-ray sources led to the development of ever more advanced techniques to produce these beams, culminating in the modern synchrotron radiation facilities, enormous equipment dedicated exclusively to the production of x-rays for materials research. A discussion of synchrotron radiation facilities will be presented in the next chapter, but it is interesting to note how much these sources have evolved, with an increase of brilliance, basically the photon flux density, available to researchers by a factor of more than 10^{14} [29].

1.2.1 Light-matter interaction events

The improvements to x-ray radiation facilities made it clear that x-rays could be used in a variety of experiments other than just diffraction. The photon energies were seen to be enough to excite core electrons of the sample to higher orbitals or outright ionize the atoms. If the emitted electron is the expected result, the technique is called x-ray photoemission spectroscopy (XPS). This technique enables the study of the electronic characteristics of a given element based on the binding energies of their core electrons of the different species of that element that are present in the sample. Alternatively, if the energies are enough only to excite the core electron to higher orbital vacancies, the technique is called x-ray absorption spectroscopy (XAS), and is used to extract detailed information about the electronic structure of the unoccupied states of the given element, as well as its environment and bonding characteristics [30]. Since the core electron binding energy depends on the element, XAS is an element-specific technique, which entails that one can selectively probe just one of the elements of the sample by tuning the photon energy to the appropriate binding energy. The edge being investigated in an XAS measurement is named after the orbital of the excited core electron according to Table 1.1. In XAS, however, species differentiation within elements is not trivial, since the spectrum of a given energy range is composed of multiple excitations of core electrons to the different unoccupied states of that atom, generating several features for the same element, while in XPS the atoms are all ionized, resulting in the same energy being absorbed, with the difference between the photon energy and the binding energy being transferred to the kinetic energy of the electrons. The differentiation between

species then becomes a simple matter of measuring the kinetic energy of the ejected electrons. The higher energies required for XPS measurements accentuate the damage caused to the sample, which may be relevant for molecular samples as will be discussed in the next chapter. If it is required, a common technique used for species differentiation in XAS is the linear combination analysis (LCA), where the spectrum is compared to reference spectra in order to determine the species contained within the sample. This is possible due to the sensitivity of the XAS to the local environment of the elements, but is not as straightforward as in XPS.

Table 1.1: Correspondence between the absorption edge nomenclature and electronic configurations of the relevant core shell for the most common edges. Taken from [29].

Edge	Configuration	Edge	Configuration
K	$1s$	N_1	$4s$
L_1	$2s$	N_2	$4p_{1/2}$
L_2	$2p_{1/2}$	N_3	$4p_{3/2}$
L_3	$2p_{3/2}$	N_4	$4d_{3/2}$
M_1	$3s$	N_5	$4d_{5/2}$
M_2	$3p_{1/2}$	N_6	$4f_{5/2}$
M_3	$3p_{3/2}$	N_7	$4f_{7/2}$
M_4	$3d_{3/2}$	O_1	$5s$
M_5	$3d_{5/2}$	O_2	$5p_{1/2}$

The different degrees of interaction between x-rays and the components of a material are called cross sections. Different interaction phenomena have varying cross sections depending on the elements involved. Fig. 1.1 shows the cross sections of the most relevant phenomena that result from x-ray interaction with the element copper. In the region of interest for the present thesis the photoabsorption is the most significant phenomena, and dominates the total cross section of the material. This makes techniques that seek to exploit photoabsorption interactions in these materials particularly suitable for synchrotron radiation facilities, although Thomson and Compton scatterings are also relevant to a certain degree.

These three events of relevance are schematically portrayed in Fig. 1.2. In the Thomson the incoming photon is elastically scattered, while inelastically scattered x-rays are a result of the Compton effect, where the absorbed energy

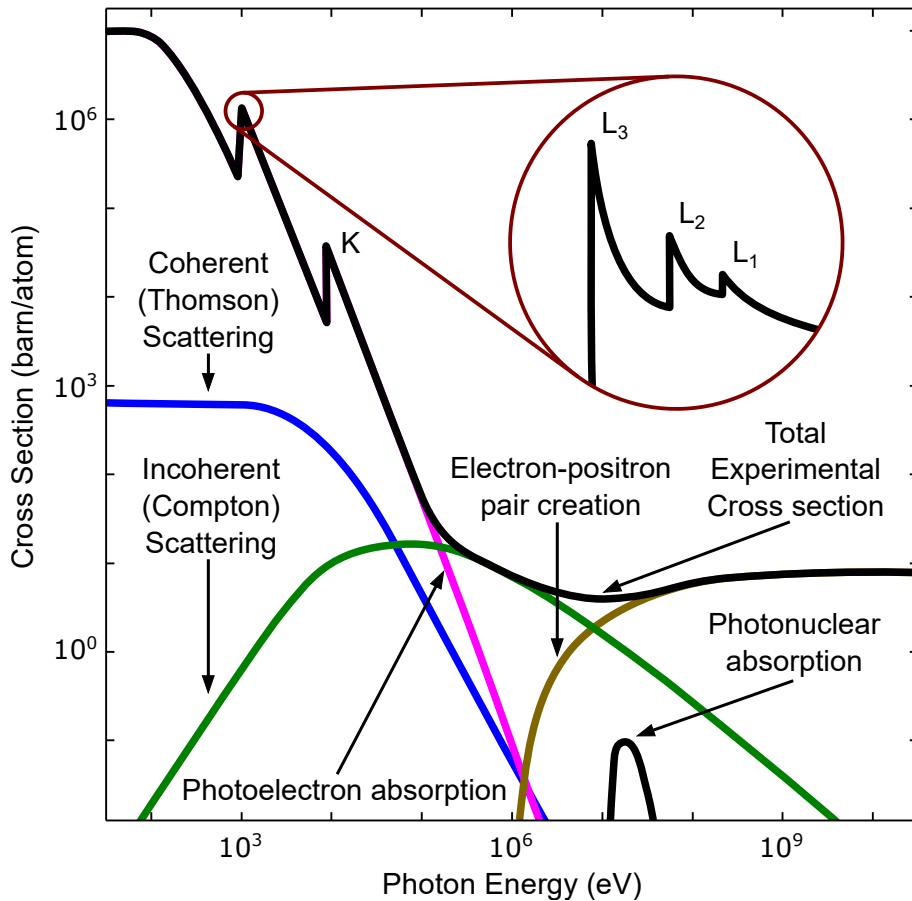


Figure 1.1: Absorption cross sections for various light-matter interactions of relevance close to the energy range of x-rays for the element copper ($Z=29$). The total experimental cross section, shown as a black solid line, is dominated in most of the x-ray energy range by photoelectron absorption events. The inset shows a more detailed view of the fine structure of the L edge. Adapted from [31].

is transferred as kinetic energy to the electron. In a photoabsorption event the photon energy is completely absorbed by the core electron of the atom, which is then excited into a higher-energy orbital or even directly emitted from the atom. This is the relevant effect for XAS and I will focus on it in this chapter. The highest occupied state in molecules is usually referred to as "highest occupied molecular orbital" (HOMO), while the "lowest unoccupied molecular orbital" (LUMO) is the first accessible state in the valence orbitals for excited electrons to occupy. The variations in the occupation of these orbitals is critical for the magnetic properties of the materials.

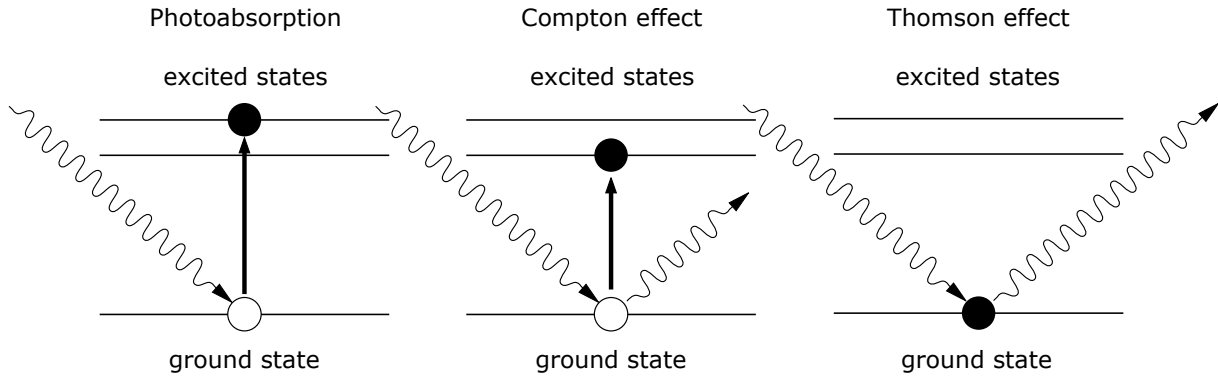


Figure 1.2: Three of the most relevant X-ray/matter interaction events in the energy range of x-rays. In a photoabsorption event, the absorbed energy of the photon is used to excite a core electron to higher energy states. In the Compton effect, the energy required for the excitation of the core electron is lower than the incoming photon energy, resulting in the inelastic scattering of the photon. In the Thomson effect there is no excitation of core electrons, only the elastic scattering of the incoming photon.

The excitation that follows a photoabsorption event generates a core hole in the atomic orbitals, which is soon filled by a second electron from another orbital. From this configuration two different events may occur, fluorescence and Auger emission. These two possibilities are portrayed in Fig. 1.3. In a fluorescence event, after the hole generated by the excitation of the core electron is filled, the left-over energy is expelled from the atom in the form of an x-ray photon that can be subsequently measured with a photon detector to determine its energy. The method of detection used throughout this thesis, however, is the total electron yield (TEY), which relies on the Auger emission in order to record the total current generated in the sample by the emitted electrons. This method is favored mainly because of the simplicity of the setup and the larger cross section of Auger emission in relation to fluorescence for low- Z elements.

In Auger emission, the ejected electron is labeled according to the orbitals involved. For instance, if the the electron is labeled KLM, K represents the orbital of the initially excited core electron, L is the orbital of the electron that fills the core hole left by the previous electron, and M is the initial orbital of the Auger electron. In TEY we are interested in the first of these electrons, as it defines the energy necessary to initiate the Auger process.

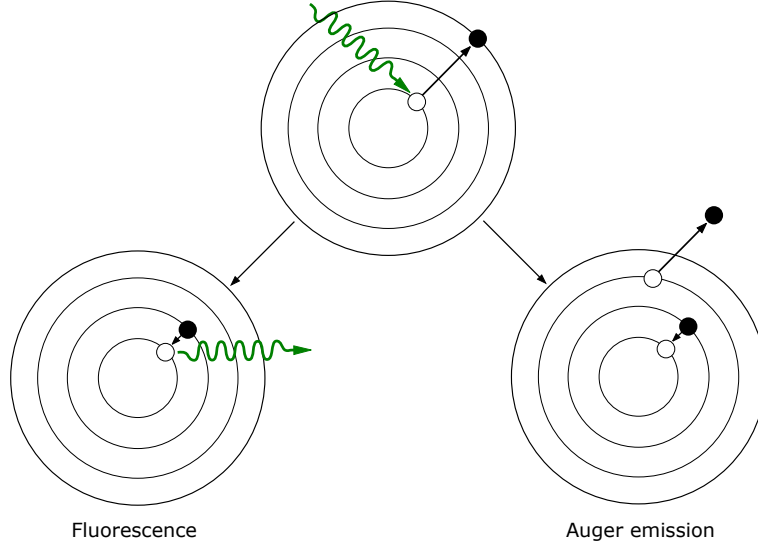


Figure 1.3: Two possible events that follow the photoabsorption of x-rays in a sample. In the fluorescence event, there is the emission of a photon, while in the Auger emission, an electron is ejected from the sample. Adapted from [29].

1.2.2 The x-ray absorption cross section

When x-rays traverse bulk materials, their intensity is reduced along their path due to absorption, depending on the linear absorption coefficient μ_x of the material, according to the *Beer-Lambert's law* for linear absorption:

$$I = I_0 e^{-x\mu_x}, \quad (1.1)$$

where I_0 is the initial intensity of the x-rays propagating in the x direction. This law generally holds very well for x-ray absorption, with deviations usually the result of interactions between molecules, disturbance of the sample's thermal equilibrium by intense light sources or when the state populated by the absorption is long-lived, resulting in a reduced population of the ground state [32]. The linear absorption coefficient is related to the atomic absorption cross section, σ , according to [33]:

$$\mu_x(\hbar\omega) = n_V \sigma(\hbar\omega), \quad n_V = \frac{n_m N_0}{A}, \quad (1.2)$$

where n_V is the atomic volume density of the sample, calculated from the mass density n_m , the Avogadro's number $N_0 = 6.022 \times 10^{23}$, and the atomic weight A .

In the Coulomb gauge we may represent the vector potential \mathbf{A} of an electro-

magnetic plane wave as:

$$\mathbf{A}(\mathbf{r}, t) = \boldsymbol{\epsilon} A_0 e^{i(\mathbf{k} \cdot \mathbf{r} - \omega t)}, \quad (1.3)$$

where \mathbf{k} is the wavevector and $\boldsymbol{\epsilon}$ is the unit vector of the polarization. Here we show only the part of the vector potential that is relevant for absorption events. The omitted part would describe photon generation events, which we are not interested in for x-ray absorption.

Since the absorption event is possible via the excitation of a core electron to an unoccupied higher state, the atomic absorption cross section may also be obtained from the transition probability per unit time between two states, P_{if} , and the photon flux density, F_{ph} , with the relation [33]:

$$\sigma(\hbar\omega) = \frac{P_{if}}{F_{ph}}, \quad F_{ph} = \frac{A_0^2 \omega \epsilon_0}{2\pi \hbar c}, \quad (1.4)$$

with P_{if} given by Fermi's golden rule:

$$P_{if} = \frac{2\pi}{\hbar} |\langle f | \mathcal{H}_{int} | i \rangle|^2 \rho(E_f) \delta(E_f - E_i - \hbar\omega), \quad \mathcal{H}_{int} = \frac{-e}{2mc} \mathbf{A} \cdot \mathbf{p}, \quad (1.5)$$

where \mathbf{p} is the sum of the linear momentum operators of the electrons, $\rho(E_f)$ is the energy density of the final state, and $\delta(E_f - E_i - \hbar\omega)$ (with E_f , E_i , and $\hbar\omega$ the energies of the final state, initial state, and photon, respectively) is the condition for a photon absorption. \mathcal{H}_{int} stands for the interaction Hamiltonian, and we have considered only the electromagnetic interaction term from the first order of the full interaction Hamiltonian, as this is the relevant part to core level absorption [34].

Taking the first two terms of the Taylor expansion: $e^{i\mathbf{k} \cdot \mathbf{r}} = 1 + i\mathbf{k} \cdot \mathbf{r} - \dots$, which is reasonable in our case, since the x-ray wavelength is much larger than the extension of a core orbital ($|\mathbf{k} \cdot \mathbf{r}| \ll 1$), we can use the simplified wave vector for our calculations. The first and second terms are the dipole and quadrupole terms, respectively, and result in the frequently used dipole and quadrupole approximations. In the dipole approximation we finally obtain for the absorption cross section, by inserting eqn. 1.5 in eqn. 1.4:

$$\sigma(\hbar\omega) = \frac{\pi e^2}{\omega \epsilon_0 c m^2} |\langle f | \boldsymbol{\epsilon} \cdot \mathbf{p} | i \rangle|^2 \rho(E_f) \delta(E_f - E_i - \hbar\omega). \quad (1.6)$$

Using the commutation properties of the atomic Hamiltonian one arrives at:

$$\frac{1}{m} \frac{\hbar}{i} \langle f | \boldsymbol{\epsilon} \cdot \nabla | i \rangle = \frac{i}{\hbar} \langle f | \boldsymbol{\epsilon} \cdot [\mathbf{r}, \mathcal{H}_0] | i \rangle = \frac{i}{\hbar} (E_f - E_i) \langle f | \boldsymbol{\epsilon} \cdot \mathbf{r} | i \rangle. \quad (1.7)$$

Replacing now the linear momentum operator in eqn. 1.6, and using the fine structure constant $\alpha = e^2/(4\pi\epsilon_0\hbar c)$ one obtains finally:

$$\sigma(\hbar\omega) = 4\pi^2\alpha\hbar\omega |\langle f | \boldsymbol{\epsilon} \cdot \mathbf{r} | i \rangle|^2 \rho(E_f) \delta(E_f - E_i - \hbar\omega). \quad (1.8)$$

The initial and final states of the absorption event can be expressed in the basis of atomic orbitals as: $|i\rangle = \sum_{m_l, m_s} a_{i, m_l, m_s} |n, l, m_l, s, m_s\rangle$ and $|f\rangle = \sum_{m'_l, m'_s} b_{f, m'_l, m'_s} |n', l', m'_l, s, m'_s\rangle$, respectively [35]. The expansion of the dipole operator into spherical harmonics to describe linearly ($q = 0$), right ($q = 1$) and left ($q = -1$) circularly polarized radiation yields [36]:

$$\sigma(\hbar\omega) = \frac{4\pi^2 e^2 \omega}{3c\epsilon_0} \mathcal{R} \left| \sum_{q, m_l, m'_l} \epsilon_q a_{i, m_l, m_s} b_{f, m'_l, m_s}^* \langle l', m'_l | Y_{1,q} | l, m_l \rangle \right|^2 \rho(E_f), \quad (1.9)$$

where $\mathcal{R} = |\langle n', l' | r | n, l \rangle|^2$ is the squared radial part of the spherical harmonics. As the dipole operator does not act on the spin and $\langle m_s | m'_s \rangle = \delta_{m_s, m'_s}$, the summation over m_s, m'_s cancels out. The radial part \mathcal{R} will contain the intensity of the transitions, while the angular part determines the orientation. It can be evaluated with the Wigner 3- j symbols:

$$\langle l', m'_l | Y_{1,q} | l, m_l \rangle = (-1)^{-m'_l} \sqrt{\frac{3(2l+1)(2l'+1)}{4\pi}} \begin{pmatrix} l' & 1 & l \\ -m'_l & q & m_l \end{pmatrix} \begin{pmatrix} l' & 1 & l \\ 0 & 0 & 0 \end{pmatrix},$$

from which the selection rules of the electric dipole transition may be readily obtained:

$$\Delta l = \pm 1, \quad \Delta s = 0, \quad \Delta m_s = 0, \quad \Delta m_l = q. \quad (1.10)$$

At the $L_{2,3}$ edges, the spin-orbit coupling is dominant, making m_l and m_s no longer good quantum numbers. The dipole selection rules change in this case to [37]:

$$\Delta l = \pm 1, \quad \Delta s = 0, \quad \Delta j = 0, \pm 1, \quad \Delta m_j = q. \quad (1.11)$$

1.3 X-ray absorption spectroscopy

There are many different ways to detect the absorption of x-rays in a sample. Regarding the Auger process, the absorption can be detected by electron yield detection or transmission. Transmission is not feasible for thick metallic substrates such as the ones we use, so the most suited method is the electron yield. There are three electron yield methods: Auger electron yield (AEY), partial electron yield (PEY), and total electron yield (TEY). The AEY technique exploits the fact that Auger electrons, unlike photoemitted ones, have a kinetic energy that remains invariant in relation to the energy of the incoming photon. This enables the setup of an energetic window in an electron analyzer placed in front of the sample, such that the intensity of the Auger electron peak can be measured as a function of the incoming photon energy. The second possibility, PEY, also uses the electron analyzer, but this time it is set to a cutoff energy rather than an energy window, so that most of the photoemitted electrons are ignored by the detector. PEY usually produces a larger electron yield than AEY, but with a lower signal-to-background ratio. The third yield detection method, TEY, is the most used one, both due to its simplicity and to its higher electron yield. In this method, all electrons leaving the sample are measured. This simplifies the measuring process by possibly doing away with electron analyzers and simply measuring the total current generated on the sample with an ammeter. While the use of an electron analyzer is still possible, this is simplified due to the fact that there is no longer a need to set energy windows or cutoff energies. As expected, this method generates the highest yield, but the lower signal-to-background ratio among the three electron yield methods. The TEY is the method used throughout this work.

As mentioned before, TEY is a technique that takes into consideration all the electrons that leave the sample following an absorption event. It is important to notice that in bulk samples, the vast majority of the signal will not be directly connected to the Auger electron described previously, but will be a result of a cascading process of secondary electron excitations, shown in Fig. 1.4. As the figure shows, the Auger electrons generated deep in the sample, beyond the electron escape depth, will not contribute to the signal because, considering the mean free path of the electrons in the material, the cascading electrons will not be able to reach the sample surface and overcome the surface potential barrier to go into vacuum. For every absorption event within the electron escape depth region, however, a large number of electrons will leave the sample from the substrate, generating a large signal in our ammeter. For this reason, the

signal will invariably contain a large background component, and great care must be taken in order to properly analyze the adsorbate signal. The most common methods used to help achieve a good signal to background ratio are the normalization to the background signal, taken at the pre-edge region, the division by a reference spectrum taken at the same time upstream on the beamline, and the division by or subtraction of a previously recorded spectrum of the substrate. Variations and modulations of the x-ray intensity are common in synchrotron facilities, the former due to instabilities and the naturally decaying nature of the electron current in the storage ring, that needs to be replenished periodically in order to attain a continuous operation. The latter because of energy-dependent reflectivity changes of the x-ray optics in the beamline.

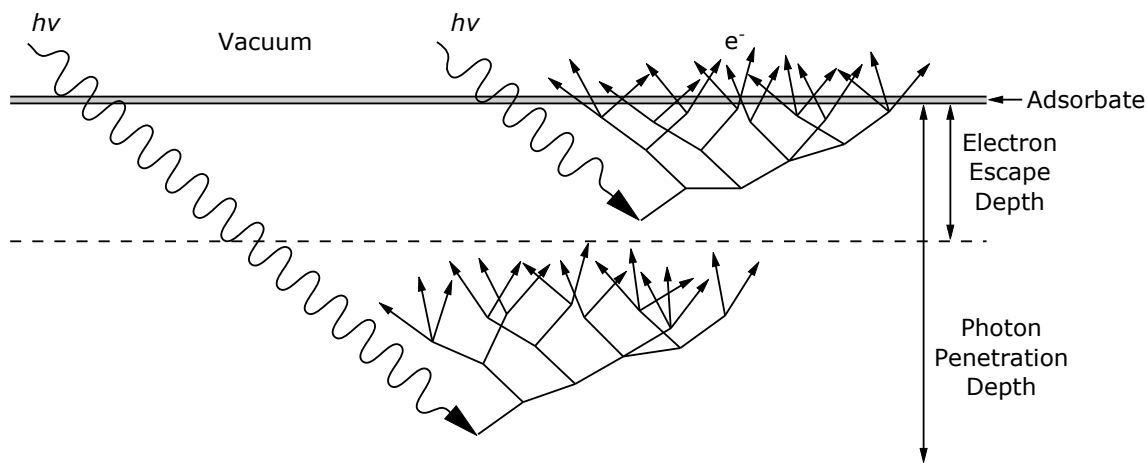


Figure 1.4: Illustration of the cascading effect of x-ray absorption events in bulk samples. The TEY signal is mainly generated by the higher order electrons excited in the sample by the absorption. Photons that penetrate deeper into the sample than the escape depth of the electrons do not contribute to the TEY signal, as the low mean free path of these electrons make it impossible for them to reach the adsorbate at the edge of the sample. Adapted from [33].

The analysis of the spectral region closer to the absorption edge is called NEXAFS (near edge x-ray absorption fine structure), while the study of the wider range of energies that follow immediately after the absorption edge is named EXAFS (extended x-ray absorption fine structure). There are several peculiarities between these two regions. The NEXAFS region is relevant for electronic excitation into valence states, as the excitation energies match the energetic separations between the core and excited states. The EXAFS region looks at the process of exciting electrons into the continuum. The low kinetic

energy range of the NEXAFS region leads to a large photoelectron backscattering amplitude by neighbor atoms, resulting in a predominance of multi-scattering events in the NEXAFS signal. The EXAFS, with higher kinetic energies, is dominated by single-scattering events. The time scales of the relevant processes in the two regions is also different, since the lifetime of a core hole is in the same time scale as the rearrangement of the valence electrons in the presence of a core hole (screening), making the sudden approximation (no screening) particularly suitable for EXAFS.

1.3.1 X-ray natural linear dichroism

The photon-absorption probability depends on the relative orientation of the electric field vector of the electromagnetic radiation, as well as its polarization, and that of the orbital being excited. The x-ray natural linear dichroism (XNLD) provides important information about the orbitals involved in the absorption process, and can also be used to determine the orientation of the molecules in certain cases. A second polarization dependence that is very important in the analysis of XAS is that of the circular polarization, as it gives rise to the XMCD technique and enables the study of the magnetic properties of the samples. The XMCD technique will be further explained in section 1.3.2.

For an example of the use of the linear polarization dependence, we may consider the excitation of an s orbital electron into a valence orbital. Due to the selection rules (eqn. 1.10), the final orbital is a p orbital. Since the s orbital is isotropic, the only orbital freedom of orientation in this event lies in the final state, that may be a σ^* orbital in the direction of the bond axis for a single bond, a π^* orbital perpendicular to the bond axis for a double bond, or both of these plus a π^* orbital perpendicular to the other two orbitals in a triple bond. The angular dependence of the x-ray absorption enables us to determine the orientation of these orbitals in the valence state, since the intensity of the absorption will depend, according to eqn. 1.8, on the orientation of the initial and final states, as well as on the orientation and polarization of the x-rays, ϵ , in a "search-light" effect, revealing whether there are empty states in a given direction [38]. Fig. 1.5(a) displays a schematic example of the relative orientations of a linearly polarized x-ray beam that comes at an angle θ to the surface and interacts with an s orbital electron, exciting it to a p valence orbital with a direction \mathbf{O} , at an angle α to the surface normal. For incoming radiation at normal incidence, the intensity of the absorption will be higher for final states lying parallel to the surface plane, while in grazing incidence, final states perpendicular to the surface

will produce greater absorption. This results in the sharp angle dependence observed in the K edge of oriented molecules, as illustrated in Fig. 1.5(b). The angle of the molecular orbitals relative to the surface may then be obtained from the ratio of the absorption intensities in these two configurations.

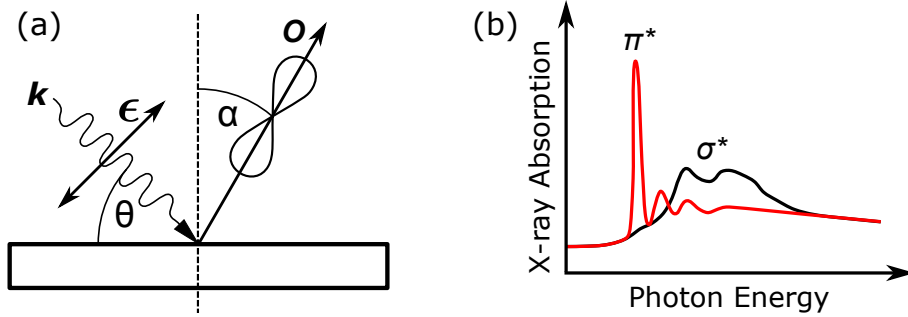


Figure 1.5: (a) Schematics of the linear-polarization-dependent interaction of x-rays and the orbitals of a sample. The highest absorption is obtained when the polarization vector of the light is parallel to the symmetry axis of the orbitals involved in the absorption event. For a K edge absorption, only the final state orientation needs to be considered, as the initial state is isotropic. (b) Example of the K edge absorption spectra for two different angles of incidence. The variation of the angle between the polarization vector of the light and the surface normal promotes the absorption into different orbitals for each angle of incidence, resulting in two different regions with high signal, marked as π^* and σ^* in reference to the final states that are preferentially probed in each angle. Adapted from [39].

The polarization vector, ϵ , and the final state orbital orientation vector may be represented in spherical coordinates as:

$$\epsilon = \begin{pmatrix} \cos \phi_1 \sin \theta \\ \sin \phi_1 \sin \theta \\ \cos \theta \end{pmatrix}, \quad \mathbf{O} = \begin{pmatrix} \cos \phi_2 \sin \alpha \\ \sin \phi_2 \sin \alpha \\ \cos \alpha \end{pmatrix}. \quad (1.12)$$

For $s \rightarrow p$ transitions, integrating over the azimuthal angle one can take it out of the equation and is left with an expression for the intensity of absorption that is only dependent on the angles of the final state orbitals and the electric field vector of the incoming radiation to the surface normal:

$$I \propto |\epsilon \cdot \langle f | \mathbf{r} | i \rangle|^2 \propto \frac{1}{2\pi} \int_0^{2\pi} d\phi (\epsilon \cdot \mathbf{O})^2 = \cos^2 \theta \cos^2 \alpha + \frac{1}{2} \sin^2 \theta \sin^2 \alpha \quad (1.13)$$

If we now take the ratio (R) of the absorption intensity in two different angles of incidence of the x-rays, usually $\theta_{norm} = 90^\circ$ and $\theta_{graz} = 20^\circ$ (due to experimental limitation it is not possible to take the measurements at full grazing incidence $\theta_{graz} = 0^\circ$). The result from eqn. 1.13 can be used to obtain the average angle of the molecules on the surface. This results in:

$$\alpha(R) = \arccos \sqrt{1 - \frac{2 \cos^2 \theta_{graz}}{R - 1 + 3 \cdot \cos^2 \theta_{graz}}} \quad (1.14)$$

When the molecules are not well oriented on the surface, the angle dependence of the absorption intensity gradually disappears, until the ratio $R = 1$ is reached, resulting in an apparent orientation of the molecules of $\alpha = 54.7^\circ$.

For other edges, the angular dependence information obtained from measurements at different angles is no longer suitable to aid in the determination of the molecular orientation, as the complexity increases greatly with the additional orbitals. It is still valuable information for the determination of the orbitals mainly responsible for the transitions observed in the x-ray absorption (XA) spectra, and may provide details about the electronic configuration of the sample beyond the total occupation of a given valence shell. One may write in a more general way, not restricted to the K edge, that since the polarization averaged intensity is a constant according to:

$$\langle I \rangle = C n_h, \quad (1.15)$$

with n_h the number of holes in the valence orbital, the intensity for a given direction α is a deviation from this constant. This formalism yields the expression [36]:

$$I_\alpha^0 = C n_h (1 - \mathcal{B} \langle \mathcal{Q}_{\alpha\alpha} \rangle), \quad (1.16)$$

where $\mathcal{Q}_{\alpha\alpha}$ is the quadrupole moment of the charge distribution and:

$$C = \frac{\pi \omega e^2}{c \epsilon_0} \mathcal{R} \frac{L}{3(2L+1)}, \quad \mathcal{B} = \frac{2L+3}{2L}, \quad (1.17)$$

with \mathcal{R} being the squared radial transition matrix element introduced in eqn. 1.9. The quadrupole moment of charge distribution ($\mathcal{Q}_{\alpha\alpha}$) comes from the definition of a dimensionless quadrupole tensor:

$$\mathcal{Q} = \delta_{\alpha\beta} - \frac{3 \mathbf{r}_\alpha \mathbf{r}_\beta}{r^2}, \quad (1.18)$$

that depends only on the angular distribution. The terms r_i denote the three

components of the position vector r . In spherical coordinates, the tensor is given by:

$$\mathcal{Q} = \begin{pmatrix} 1 - 3 \sin^2 \theta \cos^2 \phi & -3 \sin^2 \theta \sin \phi \cos \phi & -3 \cos \theta \sin \theta \cos \phi \\ -3 \sin^2 \theta \sin \phi \cos \phi & 1 - 3 \sin^2 \theta \sin^2 \phi & -3 \cos \theta \sin \theta \sin \phi \\ -3 \cos \theta \sin \theta \cos \phi & -3 \cos \theta \sin \theta \sin \phi & 1 - 3 \cos^2 \theta \end{pmatrix}. \quad (1.19)$$

This is a symmetric second rank tensor with $\mathcal{Q}_{\alpha\beta} = \mathcal{Q}_{\beta\alpha}$ and vanishing trace. It is constructed such that all matrix elements $\langle \mathcal{Q} \rangle$ vanish for a system with spherical symmetry.

1.3.2 X-ray magnetic circular dichroism

The magnetic properties of ions are mainly determined by the configuration of their valence electrons. The spin magnetic moment due to the exchange interaction is given by the difference between spin-up and spin-down holes (N_{\uparrow} and N_{\downarrow} , respectively) in the valence band, $m_S = -2\langle S_Z \rangle \mu_B / \hbar = (N_{\uparrow} - N_{\downarrow}) \mu_B$ [40]. The orbital moment $m_L = -\langle L_Z \rangle \mu_B / \hbar$ is usually not relevant for transition metals, since the magnitude of the values will be generally much lower than for the spin moment, but it is necessary to take it into account when dealing with lanthanides.

The circular polarization dependence of XAS can be exploited in the X-ray magnetic circular dichroism technique (XMCD) in order to analyze the magnetic properties of the materials under study. It can be easily understood with the two-step picture introduced by Joachim Stöhr [40]. In the first step electrons with spin-up (spin-down) are preferentially excited by right (left) circularly polarized light. The preferential excitation of electrons with different spin orientations by the two opposing photon helicities of the light is due to the transfer of different angular momentum (\hbar for right and $-\hbar$ for left polarization) to the electrons between the two polarizations and spin-orbit coupling. Due to the spin selection rule of eqn. 1.10, there is no spin flipping after the electron excitation in an absorption process. In the second step the spin-split valence shell acts as a spin detector for the excited photoelectrons. This results in a differential absorption intensity depending on the sign of the spin of the excited electrons, depending on the occupation of spin-down and spin-up electrons in the valence band. As this occupation determines the magnetic properties of the material, this enables a direct measure of the spin split of the valence band and consequently the magnetism of the sample. Fig. 1.6 shows the schematic picture of the circular-

polarization-dependent excitation of core electrons into a spin-split valence band, to clarify the principle of the XMCD measurement. The same is true for the orbital moment of the excited photoelectrons, if these are relevant, allowing for the detection of the orbital moment in this case.

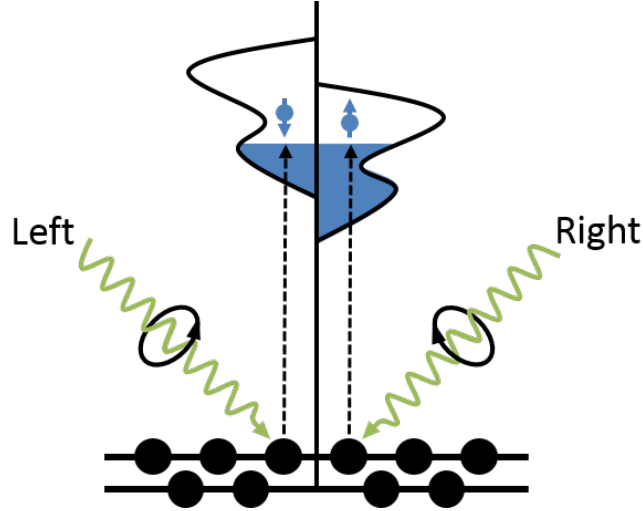


Figure 1.6: Schematic picture of the circular-polarization-dependent excitation of core electrons, in this case from the M edge, into a spin-split valence band. The angular momentum transfer from the photon to the core electrons produces spin polarized electrons depending on the helicity of the radiation. The valence band acts as a detector for the spin of the excited electrons, depending on its electrons occupation, yielding higher intensity signals for spin-down electrons than for spin-up ones.

Maximum dichroic effect will be obtained when the magnetization (M) and the light polarization directions are collinear, and it will be zero if these directions are set to be perpendicular. It is given by the difference of the absorption intensities measured with positive and negative helicities, or alternatively with sample magnetizations set to point in opposite directions. In practice this usually means the XMCD measurement can be performed by either switching the polarization sign of the circularly polarized light or the direction of the external magnetic field acting on the sample.

The preferential absorption of the different spin orientations is exemplified in Fig. 1.7, for p core electrons excited to a spin-up d valence orbital. The relative intensities of the absorption for the three different polarizations (+ for right circular, - for left circular, and 0 for linear) are shown. At the L_3 edge, right circularly polarized x-rays excite 62.5% spin-up electrons, while left circularly polarized x-rays excite only 37.5%. At the L_2 edge the majority percentages

are reversed, with 25% and 75% of excited electrons for $q = +1$ and $q = -1$, respectively.

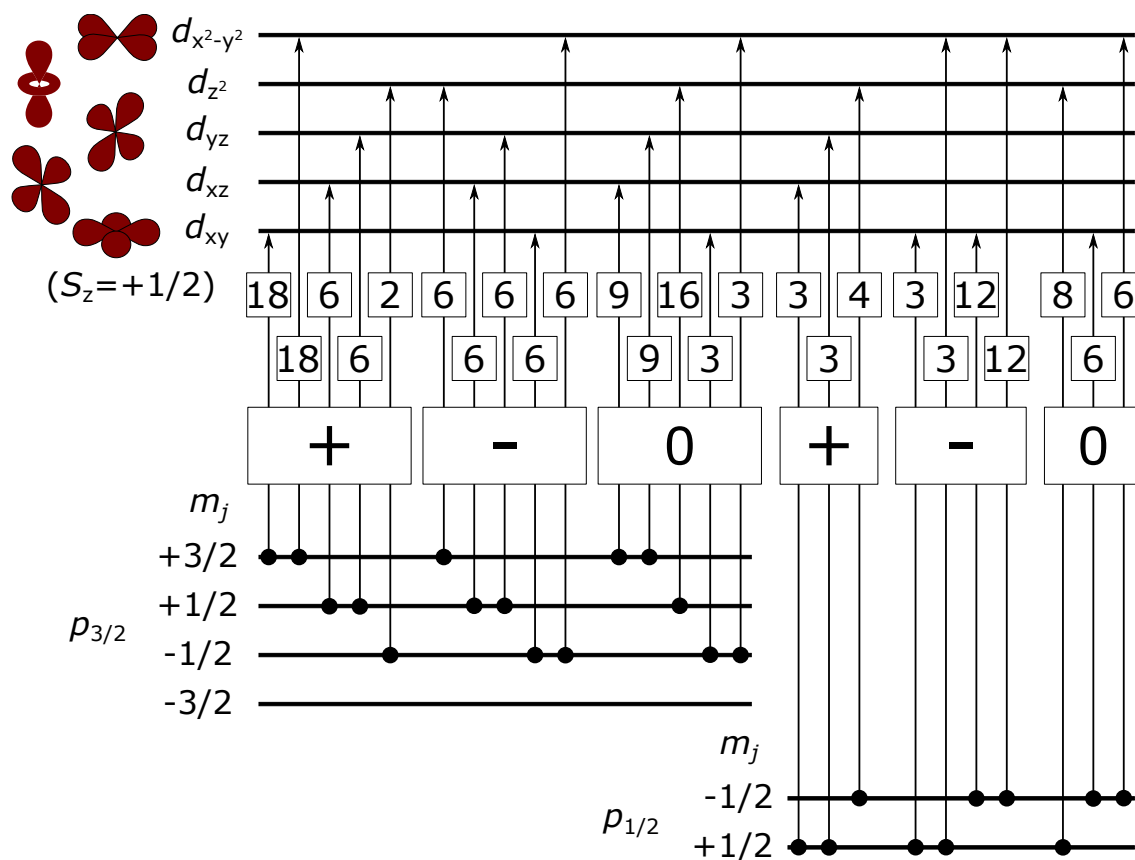


Figure 1.7: Polarization-dependent transitions from spin-orbit- and exchange-split p core states into spin-up d final states. The values in the small boxes show the relative intensity of each transition, while the signs in the big boxes display the polarization of the exciting radiation (+ for $q = +1$, - for $q = -1$, and 0 for $q = 0$). The degeneracy of m_j in the p states is assumed to be lifted by the exchange interaction, causing the different ordering of the m_j states in $p_{3/2}$ and $p_{1/2}$. Adapted from [36].

1.3.3 Sum Rules

Quantitative analysis of the intensities obtained in an XMCD experiment is carried out by the application of the so-called sum rules for the magnetic moments of the ions. Taking the $3d$ transition metals as an example, their $L_3(p_{3/2})$ and $L_2(p_{1/2})$ levels have opposite spin-orbit coupling ($l - s$ and $l + s$,

respectively), resulting in opposite spin polarization at the two edges. In the XMCD spectra this will manifest as different signs for the dichroism in the two edges (this is not the case for lanthanides). Fig. 1.8 shows the recorded spectra of a Ni sample in an XMCD measurement. The integrated intensity of the average of the two oppositely polarized spectra is shown by the dashed line of the upper panel, while the dashed lines in the lower panel show the integrated intensity of the difference between the two polarizations, the dichroic signal. The integration of the dichroic signal is shown taking both the direct integrations of the L_2 edge XMCD and the negative of that signal times two, as this is important in the application of the sum rules.

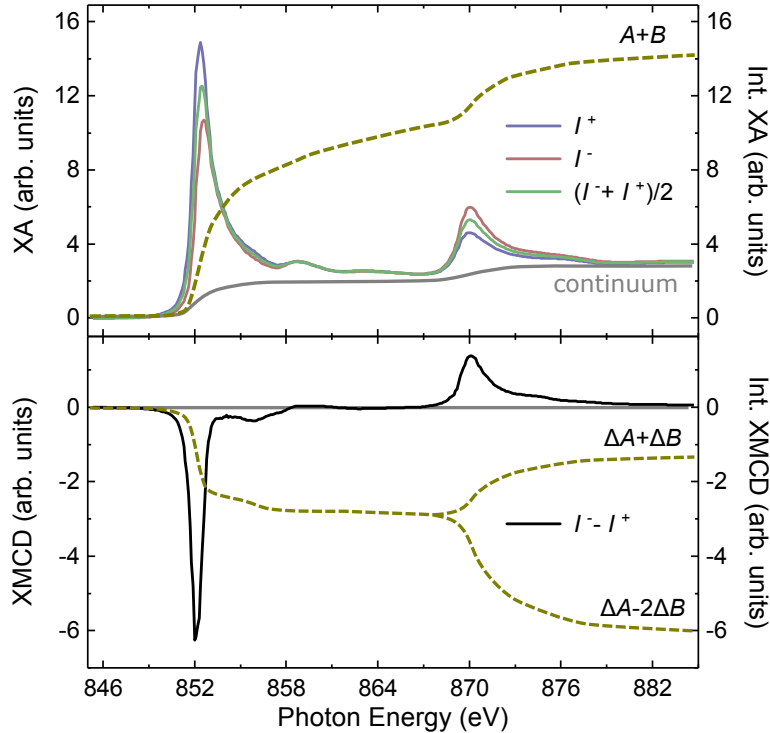


Figure 1.8: Example of the sum-rule calculations from a Ni L edge measurement. The top panel shows the XAS for two circular polarizations of the x-rays, as well as the average value between the two. The lower panel shows the XMCD obtained by subtracting the spectra of the two polarizations. $A + B$ gives the total integrated intensity of the two edges after subtraction of the continuum, represented by a step function. $\Delta A + \Delta B$ is the direct sum of the integrated intensity of the XMCD at both edges, and $\Delta A - 2\Delta B$ is an important value for the calculation of the spin sum rule.

The sum rules, first developed by Thole, Carra *et al.* [41, 42], and tested

experimentally in subsequent years [43, 44], provide a connection between the edge intensities measured with different polarizations in the XMCD experiment with physical properties of the ions, such as their spin and orbital moments. In this discussion of the sum rules applied to transition metals, the area of the white line (average between left and right circularly polarized light spectra) L_3 (L_2) edge will be named A (B) and the area of the dichroic signal (difference between left and right circularly polarized light spectra) of the L_3 (L_2) edge will be named ΔA (ΔB). The absorption intensity obtained from an XMCD measurement depends on the angle between the magnetization of the sample and the polarization direction of the light (ϵ), as well as the number of holes in the valence band (n_h) of the sample and the degree of circular photon polarization (P_c). This makes it a requirement that the angular dependence be eliminated from the sum rules in order to arrive at the correct values for the sample magnetization. This is achieved by either averaging three measurements along orthogonal coordinates or by measuring along the magic angle direction, when all anisotropic contributions cancel out.

The following discussion of the sum rules is taken from and given in more detail in the book by Stöhr and Siegmann [36]. The first important sum rule is the charge sum rule. It relates the x-ray absorption intensity to the number of unoccupied valence states (n_h) and is given by:

$$[A + B]_\alpha = C(n_h + n_Q^\alpha), \quad (1.20)$$

where α specifies the orientation of ϵ (linear polarization) or \mathbf{k} (circular polarization) and $n_Q^\alpha = \frac{7}{4} \sum_i Q_\alpha^i n_h^i$ is the anisotropy of the charge density, with $Q_\alpha^i = \langle Q_{\alpha\alpha} \rangle$ as the diagonal matrix elements of Q for an orbital i , and n_h^i the orbital-projected number of holes ($n_h = \sum_i n_h^i$). The term n_Q^α is closely related to the magnetic spin-density and orbital-moment anisotropies [45]. It vanishes when an angular average is performed or the angle α is taken to be the magic angle, yielding the isotropic sum rule. C is the proportionality constant given in eqn. 1.17.

The spin sum rule couples the dichroic signal intensity obtained by either two measurements with opposing circular polarization of the light or external magnetic fields on the sample with the spin moment of the material. It requires magnetically saturated samples in order for them to provide the correct values for the spin magnetic moment from the XMCD spectra. As such, one frequently obtains only a lower limit for this quantity instead, since magnetically saturating the sample is sometimes not possible for paramagnets with the magnetic fields

available in current laboratories.

$$[\Delta A - 2\Delta B]_\alpha = -\frac{C}{\mu_B}(m_S + m_D^\alpha). \quad (1.21)$$

The integrated intensities of the two edges usually have opposite signs, given the frequently different spin-orbit couplings of the initial states. This is the case in the $3d$ metals and results in the difference in the first part of eqn. 1.21 yielding a relatively large value, since it adds the magnitude of the integrated intensity of the first edge with two times the one of the second. m_S is the spin moment and the term m_D^α represents the anisotropy of the spin density. It is given by $m_D^\alpha = -7\langle T_\alpha \rangle \mu_B / \hbar$, with the intra-atomic magnetic dipole operator given by $\mathbf{T} = \mathbf{S} - 3\hat{\mathbf{r}}(\hat{\mathbf{r}} \cdot \mathbf{S})$. The term $T_\alpha = \sum_\beta Q_{\alpha\beta} S_\beta$ couples the charge (represented by the quadrupole operator \mathcal{Q}) and the spin components of T . It represents the spatial distribution of the spin density, usually increasing as the symmetry of the system is reduced. As such, it can become very significant in low-symmetry molecular systems [46]. m_D^α can be excluded if the spin-orbit coupling is weak compared to the ligand field by performing the average measurements along the three orthogonal axes or by measuring along the magic angle (35.3° from the surface). This requires, however, that the magnetization of the sample also be saturated in the propagation direction of the x-rays. Otherwise the spin moment calculations will always contain the contribution from the magnetic dipole operator and care must be taken in order to avoid mistakes in the analysis of the data.

The final sum rule to be presented here is the orbital sum rule. It relates the dichroic signals of the two edges to the orbital moment of the sample, and is given by:

$$[\Delta A + \Delta B]_\alpha = -\frac{3C}{2\mu_B} m_L^\alpha. \quad (1.22)$$

The determination of the orbital magnetic moment (m_L^α) from the orbital sum rules requires stronger alignment of the magnetization of the sample in the direction of the incoming x-ray propagation as well as a more careful data collection and analysis than for the other two sum rules. This is due to the fact that the first part of eqn. 1.22 usually reduces to a very small value calculated from large values of the integrated XMCD intensities.

In order to apply the spin and orbital sum rules that were just introduced to real XMCD measurements performed with TEY, one needs to normalize the intensity obtained from the experiments, as the conversion factor of x-rays into secondary electrons in the sample enters as an unknown quantity. This is done by

normalization to the isotropic charge sum rule. Additionally, the angle between the magnetization direction of the sample and the x-ray propagation direction (ϕ), as well as the degree of circular polarization (P_c) of the light and the number of empty states in the valence band (n_h) must be considered in the equations. When one includes these factors and writes the sum rule equations using the thermal expectation values of the operators, they yield for the transition metals [37]:

$$2\langle S_\alpha \rangle + 7\langle T_\alpha \rangle = \frac{n_h \hbar}{P_c \cos \phi} \frac{[\Delta A - 2\Delta B]_{\alpha'}}{[A + B]_{\bar{\alpha}}}. \quad (1.23)$$

$$\langle L_\alpha \rangle = \frac{2}{3} \frac{n_h \hbar}{P_c \cos \phi} \frac{[\Delta A + \Delta B]_{\alpha'}}{[A + B]_{\bar{\alpha}}}. \quad (1.24)$$

For lanthanides the equations change slightly due to the differences in the prefactors, yielding:

$$2\langle S_\alpha \rangle + 6\langle T_\alpha \rangle = \frac{1}{2} \frac{n_h \hbar}{P_c \cos \phi} \frac{[2\Delta A - 3\Delta B]_{\alpha'}}{[A + B]_{\bar{\alpha}}}. \quad (1.25)$$

$$\langle L_\alpha \rangle = \frac{n_h \hbar}{P_c \cos \phi} \frac{[\Delta A + \Delta B]_{\alpha'}}{[A + B]_{\bar{\alpha}}}. \quad (1.26)$$

1.4 Ligand field theory

Ligand field theory (LFT) describes the bonding within molecules and metal complexes in terms of the interaction between the different ligands and the metal ions. It is largely constructed upon a preceding approach, the crystal field theory (CFT), that was created to describe the electronic structure of transition metals within a crystal. The ligand ions surrounding the metal ions create an electrostatic field that promotes a split of the degenerate levels of the d orbitals of the metal. In CFT the anions are described as point charges and the field generated by these charges, as well as the effects on the d orbitals of the metal, would depend on the distribution of the charges around it. The realization that CFT could be very successfully applied to metal complexes by representing the ligands around the metal ion by point charges soon took hold, and CFT was used to further the development of the theory describing molecular orbitals. In an octahedral geometry, CFT predicts that the five orbitals of a transition metal would split into two sets of orbitals, the $d_{x^2-y^2}$ and d_{z^2} , with e_g symmetry, and the d_{xy} , d_{xz} , and d_{yz} , with t_{2g} symmetry. The energy separation between the two sets of degenerate orbitals is identified as Δ_o or $10Dq$. If the metal complex

exhibits large values of Δ_o , it is said to be in a strong ligand field, in contrast to the weak ligand field case of small Δ_o . The strength of the ligand field is very important in these complexes, because it will be a determinant factor in their electronic and magnetic properties.

The separation of energy levels in an octahedral geometry is a consequence of the symmetry of the metal's orbitals. With the aid of CFT, it is simple to see how the energy of the orbitals is affected by the geometry of the crystal field. The orbitals that are closer to the point charges are going to have their energy increased by the electrostatic interaction between the electrons. Fig. 1.9 shows how this leads to the increase in energy of the e_g orbitals. However, it is not expected from CFT that the t_{2g} orbitals would have their energy lowered, since the addition of point charges would always lead to an increase in the energy of the orbitals, albeit more in some orbitals than others. This is because in CFT the molecular orbitals of the ligands are ignored, in order for them to be treated simply as point charges generating an electrostatic field. This meant that, although useful for clarifying and predicting some of the properties of metal complexes, it failed to explain the electronic stabilization that is the driving force of metal-ligand bond formation [47]. For that reason LFT was developed from the combination of CFT and molecular orbital theory. In LFT the point charges of CFT are replaced by molecular orbitals, and symmetry consideration must be taken when the interactions between the metal and ligand orbitals are evaluated. This leads to a reduction in the energy of the bonded metal complex, therefore stabilizing the bonded state.

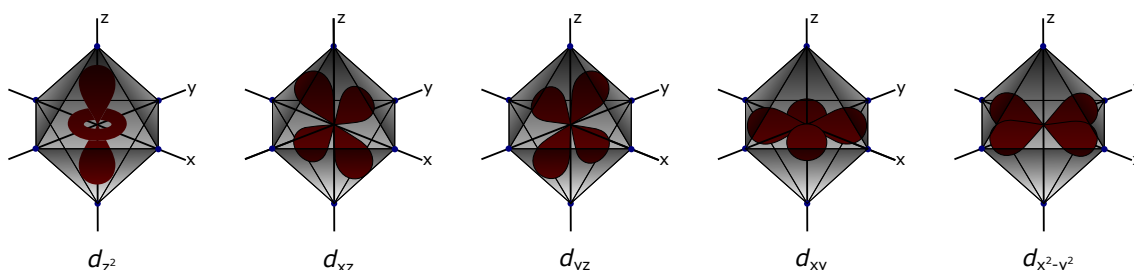


Figure 1.9: The d orbitals under octahedral crystal field geometry. The point charges, represented by the small blue dots, are meant to reproduce the crystal field experienced by the orbitals in the crystalline environment. The orbitals that are closer to the charges experience a greater increase in their energy, causing the degeneracy of the energy levels of the isolated ion to be broken.

Different molecular geometries lead to distinct energy level distributions, as depicted in Fig. 1.10 for square pyramidal and square planar geometries in

addition to the spherical and octahedral ones. These geometries that deviate from octahedral are usually treated as perturbations upon the higher symmetry [48]. The exact order of the energy levels is not fully known, and results usually depend on the calculation method used to obtain the energies [47]. The energy difference between levels (Δ_o) is still relevant in the geometries with lower symmetries and will be an important factor in the molecule's spin. In sufficiently strong ligand fields, the separation between energy levels will be enough to overcome the pairing energy of the electrons, resulting in low-spin complexes, as the electrons will tend to pair up at lower energy states. In contrast, weak ligand fields generate high-spin molecules. This is particularly important for spin-crossover molecules, mentioned previously, when the ligand field strength is usually at the threshold of the point the molecules switch from low to high spin, making small changes to the ligand field significant to the properties of the molecule. For non-spin-crossover molecules it plays a major role, however, as it is at the core of the magnetic properties of these molecules.

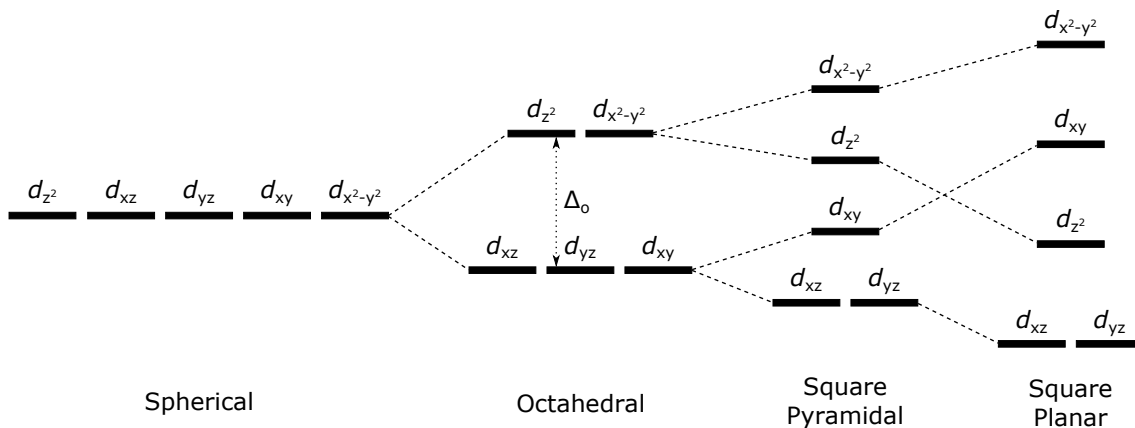


Figure 1.10: Energy splitting experienced by d orbitals under different crystal field geometries. The energy separation given by Δ_o is the result of the break in the degeneracy caused by the octahedral field, when the energy levels divide into orbitals with e_g and t_{2g} symmetries.

In metal complexes there are two types of interactions, shown in Fig. 1.11. In σ interactions the bond is symmetric along the bonding axis, while in π interactions it is not. Additionally, an orbital is said to be inversion symmetric and have positive parity if it is invariant under the operation of moving each volume element of the orbital amplitude wavefunction from \mathbf{r} to $-\mathbf{r}$. Otherwise, it is said they have negative parity. This means that s and d orbitals have positive parity, while p and f orbitals have negative parity. For metal complexes the most

common interactions are the σ donation, where the ligand donates electrons to the metal, and the π back-donation, or π acceptor interaction, where the metal donates electrons to the ligand. The π donor interaction, where the ligands would donate electrons to the metal through the π orbital interaction, is generally not favored for metals due to their relatively low electronegativities. Conversely, the usual π back donation is favored, in part because it helps stabilizing the metal complex by transferring back a bit of the charge gained through σ donation interactions [47].

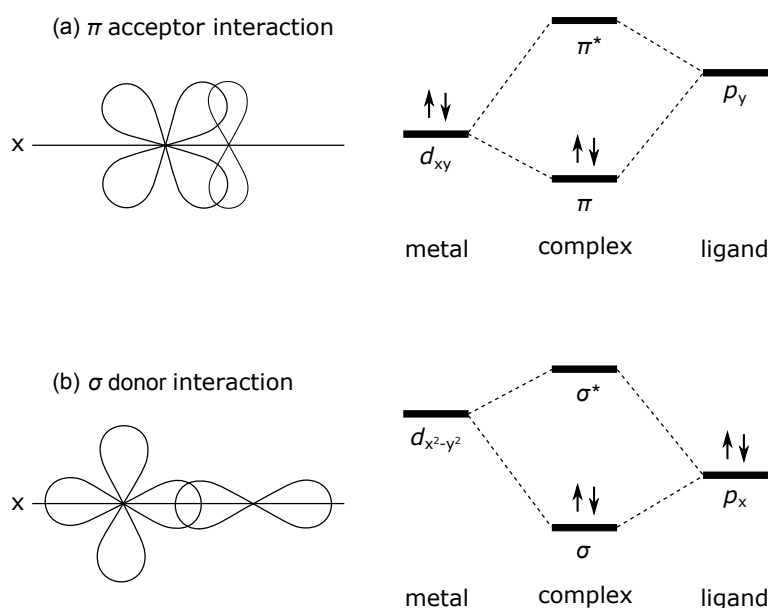


Figure 1.11: Most common interactions for metal complexes. In the π acceptor donation, shown in (a), also called π back-donation interaction, the ligand accepts electrons from the metal. In the σ donor interaction, shown in (b), the opposite happens, and the ligand donates electrons to the metal in order to form an energetically more stabilized molecular orbital.

The σ interactions are generally stronger than π interactions, given that the axial overlap is more efficient than the sideways one. The energy separation between the resulting orbitals is therefore larger for σ (bonding) and σ^* (antibonding) molecular orbitals than for the π and π^* ones [49].

1.5 Spin Hamiltonian formalism

Magnetic interactions in molecular systems are similar to the ones observed in crystal lattices, with the relevance of pair interactions being larger in molecular systems. The origin of the coupling between two magnetic centers lies in the electrostatic interaction responsible for the formation of the bond between the two centers. The magnetic fields of the two centers, while interacting, have been shown to represent energies far smaller than the usual interaction energy between transition metal ions, for instance. In the formulation of these interactions, one may consider two individual magnetic centers with unpaired electrons, A and B, initially isolated. A bridging group L with no unpaired electrons would connect the two centers. The interaction takes place when the electrons in A feel the presence of the electrons in B and vice versa [14]. In this configuration this is called the "super-exchange interaction", when the connection between the metal centers is mediated by a diamagnetic ligand. Otherwise, when the two metal centers interact directly, this is the usual exchange interaction. These interactions are of fundamental importance in molecular magnetism.

For the isolated metal centers, the most common approach to determine their magnetic properties is the spin Hamiltonian. This enables one to ignore the complicated orbital coordinates required to fully describe these systems, replacing them with spin coordinates that take full advantage of their symmetry. It is important to note that a central simplification necessary for this model to work is that the orbital moment of the metal centers is small, so that it can be treated as a perturbation. This is the case for many metallic complexes, particularly those of transition metals, because the ligand field tends to quench the orbital moment in these systems.

A magnetic center with ground state characterized by S will have $2S + 1$ spin states associated with it. These initially degenerate states for the isolated ion can be split first by the crystal field of the ligands, discussed previously, and then by the influence of an external magnetic field \mathbf{B} . The spin Hamiltonian formalism requires that each of these interactions be described by individual interaction Hamiltonians that combine to form the full spin Hamiltonian of the system. The external magnetic field is represented by the Zeeman Hamiltonian:

$$\mathcal{H}_Z = \mu_B g \mathbf{B} \cdot \mathbf{S}, \quad (1.27)$$

where μ_B is the Bohr magneton, the magnetic moment of the electron, g is the Landé factor, usually taken as 2 for magnetic systems with quenched orbital moments, \mathbf{B} is the external magnetic field and \mathbf{S} is the spin operator. The

magnetic moment is given by $\mathbf{m} = -\mu_B g \cdot \mathbf{S}$.

The crystal field Hamiltonian is usually given as a quadratic form of the spin operator:

$$\mathcal{H}_{CF} = \mathbf{S} \cdot \mathbf{D} \cdot \mathbf{S}, \quad (1.28)$$

where \mathbf{D} is a real, symmetric tensor. With appropriate choice of coordinate axes, this Hamiltonian can be written in terms of the diagonal components of \mathbf{D} as:

$$\mathcal{H}_{CF} = D_{xx}S_x^2 + D_{yy}S_y^2 + D_{zz}S_z^2 = DS_z^2 + E(S_x^2 - S_y^2), \quad (1.29)$$

where

$$D = D_{zz} - \frac{1}{2}D_{xx} - \frac{1}{2}D_{yy}, \quad \text{and} \quad E = \frac{1}{2}(D_{xx} - D_{yy}). \quad (1.30)$$

In cubic symmetry, the term with D can be ignored, since $D_{xx} = D_{yy} = D_{zz}$. In axial symmetry, the term with E can be disregarded, as $D_{xx} = D_{yy}$. We have, therefore, for the uniaxial case, very important in many classes of molecules, such as the ones discussed in this thesis, the crystal field Hamiltonian given simply by:

$$\mathcal{H}_{CF} = DS_z^2. \quad (1.31)$$

This is often called the zero-field splitting (ZFS) term of the spin Hamiltonian, as it requires no external magnetic field to break the degeneracy of the ground state. The eigenstates of this Hamiltonian are the $|m\rangle$ eigenvectors of S_z^2 , with eigenvalues $Dm^2 - S(S+1)/3$ [14]. The sign of D will determine the magnetic anisotropy of the ion: positive D leads to greater stabilization for low values of $|m|$, which translates to easy-plane anisotropy, while negative values of D lead to greater stabilization for high values of $|m|$, resulting in an easy-axis configuration of the magnetic anisotropy.

2

EXPERIMENTAL DETAILS

2.1 Introduction

In this chapter the different aspects of the experimental procedure performed in the measurements and discussed in the next chapters is presented. An introduction to the most important features of synchrotron radiation facilities and x-ray generation is given first, followed by the description of the VEK MAG, one of the end-stations utilized for this research. A special focus will be given to the sample preparation chamber, the assembling of which was an important part of my responsibilities. The description of the various types of sample preparations will then be given. In the end a brief description of the details of XAS methods employed in the analysis of the samples will be presented.

2.2 Synchrotron radiation facilities

Synchrotron radiation is an electromagnetic wave produced when charged particles are accelerated in a direction perpendicular to their velocity. In synchrotron radiation facilities this is obtained by accelerating electrons to relativistic energies and speeds close to the speed of light, then altering their trajectories with magnetic fields. For electrons with energies in the range of GeV, standard magnetic devices in synchrotron radiation facilities will produce radiation in the x-ray wavelength range. X-rays are short-wavelength, high-frequency electromagnetic waves, and their importance lies exactly in their physical characteristics, which place them in a very special part of the electromagnetic spectrum, between the

ultraviolet and the gamma ray radiation. In this energy range, electromagnetic waves have the exact energy necessary to excite core electrons of the atoms of a material into its outer orbitals. The tuning of the x-ray energy allows the well-defined excitation of electrons in particular orbitals, as explained in the previous section, making this a very important radiation for the study of the electronic properties of materials. Coupled with the high brilliance that can be obtained from such facilities, an important tool for the study of molecules and other nanostructures is found in synchrotron radiation. Originally, synchrotron radiation was a by-product of high-energy facilities, and studies done using it were performed in a parasitic way in these facilities. Soon, however, the unique characteristics of synchrotron radiation, described previously, justified the construction of dedicated synchrotron radiation facilities. The most common form of these facilities, dedicated to the production of x-ray radiation, is the storage ring, in which accelerated electrons are injected into a quasi-circular path controlled by magnets. This path is composed of several intercalated straight and curved sections, in such a way that at each curved section, where the electrons are radially accelerated, x-rays can be guided outside of the storage ring and into a beamline, for them to be used in interactions with materials being studied. The electron storage ring of the Helmholtz-Zentrum Berlin für Materialien und Energie, BESSY II, where all the experiments reported in this thesis were conducted, has a perimeter of 240 m and operates at 1.6 GeV.

Prior to the injection into the storage ring, the electrons must be accelerated to the high energies required for the production of x-rays. The different parts of a typical storage ring facility are shown in Fig. 2.1. The first part is the LINAC, or Linear Accelerator, where the electrons are extracted from a source and accelerated to moderate velocities through a series of oscillating electric fields generated by plates connected to an alternating power supply. The electrons are then injected into a booster ring, similar to the storage ring but smaller in size, where the electrons are further accelerated and tuned to the energy of the storage ring. This is usually achieved by devices present in the booster ring known as Radio Frequency Cavities (RF Cavities). In these cavities the electrons are once again accelerated by electric fields, but this time the fields are generated by the resonance of radio waves inside the cavities. The careful choice of the frequency and phase of the radio waves, depending on the shape of the cavity, enables the compression of the electrons into bunches with the required energy and frequency. Once the desired energy has been achieved, the electrons are finally injected in the storage ring, where they circulate at a near constant energy for some time. Depending on the injection mode of the storage ring, the electron current

is maintained either by large injections after long intervals, which is called the Decay mode, or by small injections after short intervals, the Top-Up mode. The Top-Up mode guarantees a stable current, but demands a good normalization method to remove the injection spike from the measured data.

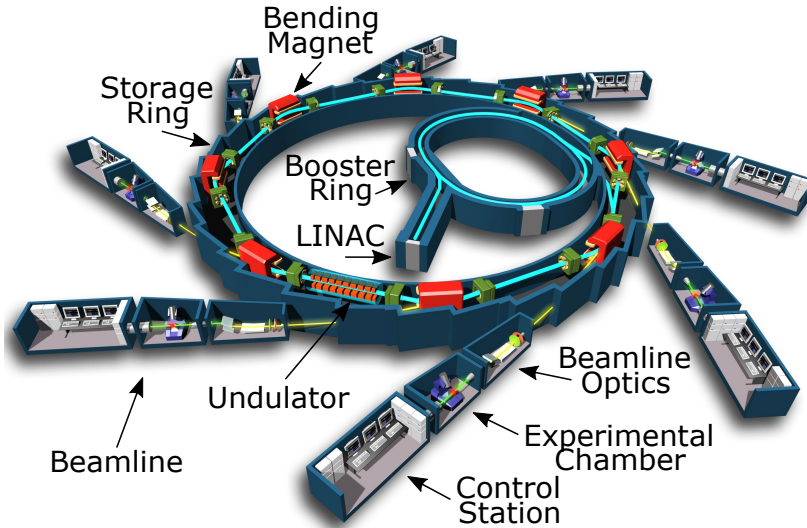


Figure 2.1: Simplified diagram showing the details of a synchrotron facility. Adapted from the original by EPSIM 3D/JF Santarelli, Synchrotron Soleil.

2.2.1 Generation of x-rays

The simplest way to obtain x-rays in these facilities is with a bending dipole magnet, which consists of a single section of the ring where a magnetic field perpendicular to the path of the electron is generated, causing the radial acceleration on the electrons. X-rays produced with bending magnets generally have low brilliance and are linearly polarized in the plane of the storage ring. Additional optical components are required in bending magnet beamlines if one wishes to obtain circularly polarized light. These components take the light out of the plane of the storage ring and decompose it into various differently polarized parts, from which the desired polarization can be selected. The choice of the polarization is important, as discussed in the previous chapter, in order to extract conformational and magnetic information from the sample.

Another way of obtaining the x-rays from the high-speed electrons is through the use of periodic magnets known as insertion devices. These device consist of arrays of magnets that generate magnetic fields in alternating directions along

the path of the electrons. Fig. 2.2 illustrates the operating principle of bending dipole magnets and insertion devices. In the insertion device, the oscillating trajectory assumed by the electron causes synchrotron radiation to be generated with every change in the direction of the motion. This results in a higher brilliance than for the x-rays obtained with bending magnet devices. The most widespread insertion devices are undulators and wigglers. These two have similar operating principles, but wigglers generally have higher magnetic fields, resulting in a wider-angle and incoherent x-ray beam. The undulator, on the other hand, produces a constructive interference between individual x-rays, which allows for a direct tuning of the polarization properties of the x-ray by changing the geometry of the magnetic fields.

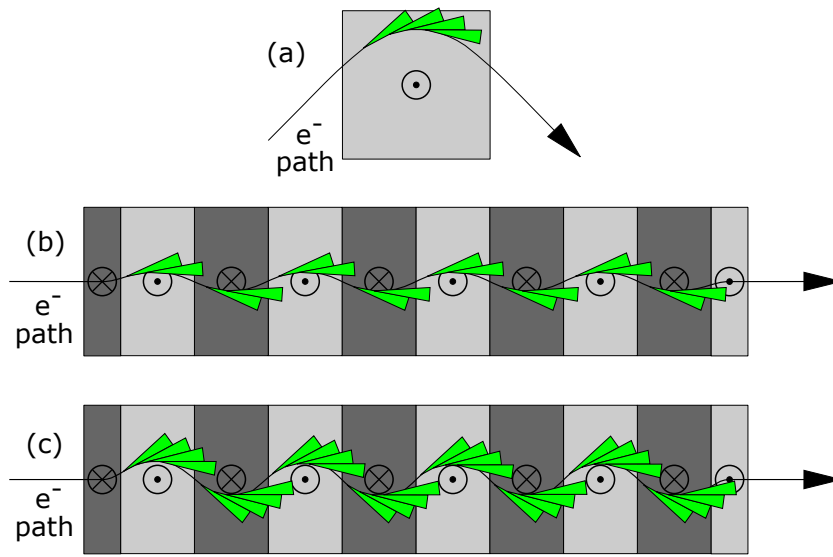


Figure 2.2: Schematic drawing of the magnetic fields, shown as crosses and dots for fields going in and out of the plane of the paper, respectively, electron path and generated x-rays, shown in green, for bending magnets (a) and insertion devices (undulator (b) and wiggler (c)). The magnets located at the extremes of the undulator are half the size of the others in order to keep the electron beam parallel before and after the insertion device.

One of the most popular insertion devices is the APPLE II, that stands for Advanced Planar Polarized Light Emitter. It is an elliptical undulator and the insertion device of the UE46 beamline at BESSY II, where the experiments described in chapter 3 were performed. It works by the combination of 4 rows of magnets, where the rows can move independently in the direction of the electron's original trajectory, generating the elliptical acceleration of the electron, and the

resulting polarization can be then determined by the relations between the rows. Fig. 2.3 illustrates the different possibilities. In the standard configuration the two rows of magnets on the top match half of the magnets of the bottom rows, while it is the opposite for the other half. This results in x-rays with linear polarization in the horizontal direction, since it causes the electrons to oscillate in the horizontal plane, while maintaining the vertical position constant. This configuration is illustrated in Fig. 2.3(a). The situations shown in Fig. 2.3(b) and (d) result in the electron oscillating both in the horizontal and vertical directions, producing circularly polarized x-rays. In Fig. 2.3(c), the electron path varies only in the vertical direction, resulting in vertically polarized x-rays. The sets of two rows of magnets can also be moved in the vertical direction, for the tuning of the wavelength.

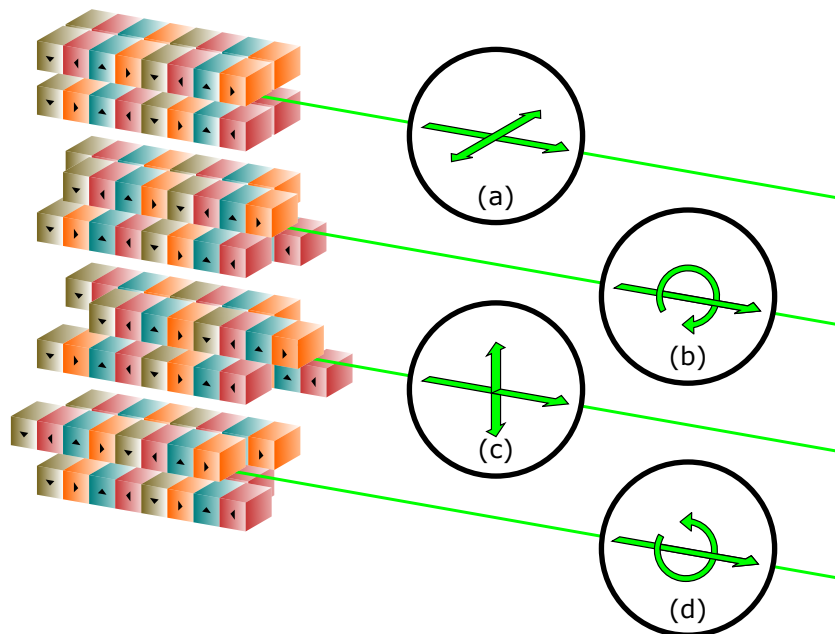


Figure 2.3: Different modes of an elliptical undulator. In its standard configuration (a) horizontally polarized x-rays are produced. Shifting two diametrically opposed magnet rows forward by one magnet unit (b) produces right circularly polarized light, while moving them forward by two units produces vertical polarization. Moving these rows three units is equivalent to moving them backwards by one, and results in left circularly polarized radiation (d).

2.2.2 Beamline Optics

The x-rays produced in the bending magnets or insertion devices is then guided into the different beamlines of the synchrotron facility, where they are further optimized by various optical components in order to obtain the desired properties. Fig. 2.4 illustrates a typical set of optical components present in a beamline. For a bending magnet beamline, such as the VEKMAG, additional mirror arrays are required to produce light with different polarizations. The light generated by a bending magnet is linearly polarized in the plane of the electron ring, but elliptically polarized above and below this plane. This allows for the selection of the desired components with either polarization through the use of optical devices. Undulator insertion devices, on the other hand, natively produce elliptically polarized light in the plane of the ring, and the properties of the polarization can be altered by changing the position of the magnets in relation to each other, as discussed previously, so the polarization is already determined before entering the beamline, and only other adjustments to the x-rays are required. Wiggler insertion devices also produce linearly polarized light, because even though they, like undulators, produce light by an oscillating magnetic field, in their case the overlapping of the different polarizations cancels out and the resulting light is linearly polarized. Circularly polarized light can also be obtained from wigglers with additional steps.

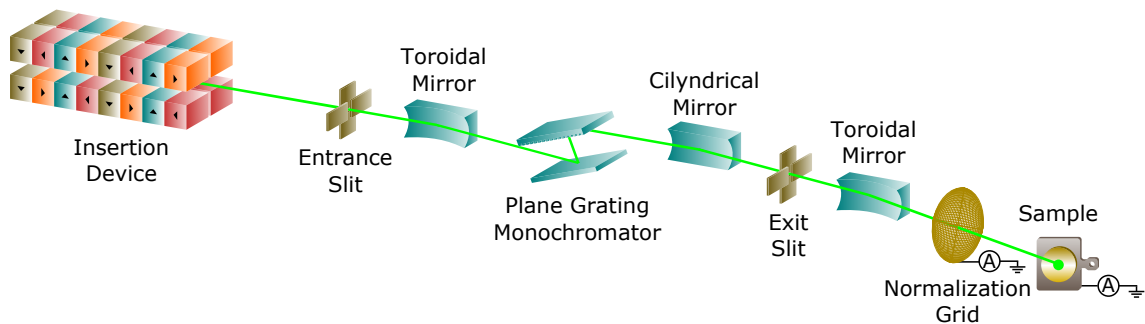


Figure 2.4: Typical optical components of a beamline. This schematic drawing shows the UE46 beamline at BESSY II.

The typical optical components shown in Fig. 2.4 describe the UE46 beamline, at BESSY II. It consists of slits to cut the beam in the horizontal and vertical directions, toroidal and cylindrical mirrors for the focusing or collimating of the beam, a plane grating monochromator and exit slit for the wavelength selection, and a gold grid as a normalization device. The normalization device helps reduce the influence of beam instabilities in the measurement and it works in total

electron yield (TEY) mode. After the beam properties have been determined, it interacts with the sample, placed in a magnetic field in most of our experiments, and the signal is produced, also by TEY.

2.3 VEKMAG

The VEKMAG is a new soft x-ray station of BESSY II that is designed for the analysis of magnetic systems under low temperatures and high magnetic fields. The vectorial superconducting magnet system is capable of delivering a magnetic field of 9 T in the direction of the x-rays, 2 T in the horizontal plane, and 1 T in every other direction. The assembly of the coils is shown in Fig. 2.5. The temperature range available to the sample is 2 to 350 K when using the Low-Temperature Variable Temperature Insert (LT-VTI). The low temperatures are achieved with a helium cryostat. To get to the lowest temperatures, a cooling shield needs to be placed around the sample. A second VTI is available for Ferromagnetic Resonance (FMR) measurements. In this VTI the temperature range is 8 to 500 K and there is no possibility for the employment of a cooling shield. Developments are underway for the construction of a helium-3 VTI, which would deliver temperatures in the millikelvin range.

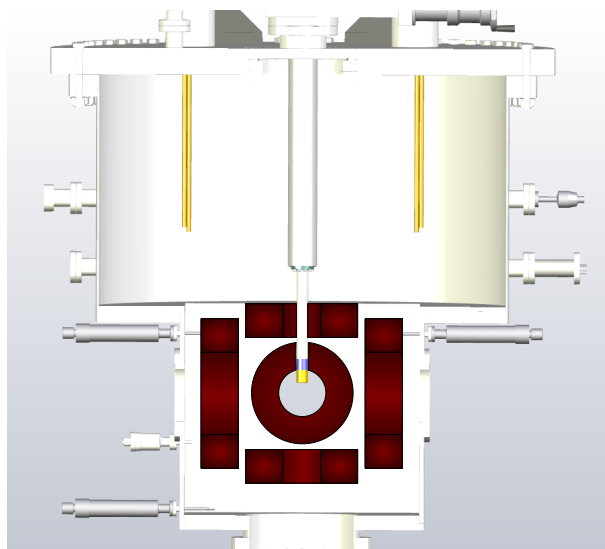


Figure 2.5: Outer shell of the magnet chamber with the superconducting coils (red color) assembly required for the vectorial magnetic field produced on the samples. The helium and nitrogen containers are not distinguished in the picture.

The VEKMAG end-station is located in a bending magnet beamline, the D51 dipole line, and for that requires a mirror array mounted on a hexapod system in order to extract circularly polarized x-rays from the beam coming from the beam that is obtained from the dipole magnet. The energy range is 20 to 1600 eV and the degree of circular polarization of the x-rays is $77\% \pm 3\%$, depending on the configuration of the mirror array. The integrated photon flux on the sample is 5×10^9 photons/s. This effect of this high flux can be attenuated for sensitive samples with foils placed on the beam path or by defocussing the beam, which distributes the flux over a larger area. This is usually required for sensitive molecular samples, as will be discussed later in this chapter. The standard area of the focused beam is $50 \times 100 \mu\text{m}^2$. It can be reduced to $50 \times 60 \mu\text{m}^2$, and further to $25 \times 60 \mu\text{m}^2$. The unfocused beam has an area of $0.8 \times 0.8 \text{ mm}^2$, resulting in a photon flux density of 7.8×10^9 photons/(s \times mm^2). For comparison, some of the characteristics of the UE46-PGM-1, an undulator beamline from BESSY II, where the experiments discussed in Chapter 3 were done, are: $E_{\text{range}} = 120$ to 2000 eV, $C_{\text{pol}} = 85\%$, $p_{\text{flux}} = 10^{12}$ photons/s. The standard focus size is $100 \times 50 \mu\text{m}^2$, it can be reduced to $40 \times 10 \mu\text{m}^2$, and the uncollimated mode beam has an area of $1.7 \times 1.5 \text{ mm}^2$. The superconducting magnet enables a field of 7 T in the direction of the beam, while the sample can be brought down to a temperature of 4 K. The undulator allows for the production of circularly and linearly polarized x-rays in any direction. While the undulator beamline is more flexible in the production of powerful x-rays, the VEKMAG offers more versatility with the control of the magnetic field, lower temperatures, and softer x-rays. It is also better suited for the study of fast magnetic relaxation phenomena, as the magnetic field sweep rate can be set up to 3 T/min. Both beamlines used 1200 mm^{-1} plane grating monochromators.

The fixed end-station is composed of three main chambers, shown in Fig. 2.6. They are the Deposition Chamber (in gray, to the right), the Detector Chamber (in green), and the Magnet Chamber (in grey, on top of the Detector Chamber). The chamber in yellow to the left is the last of the beamline optical components, where the normalization membranes and foils are located. The Detector Chamber contains the detectors used for transmission and reflectance measurements. It is also where the sample transfer from the Deposition Chamber to the Magnet Chamber is done. A long transfer rod, not shown in Fig. 2.6, brings the sample shuttle, seen in Fig. 2.8(b), from the Deposition Chamber to the Detector Chamber, where it is taken from the rod with a telescopic mechanism that is then used to lift the shuttle to the Magnet Chamber's VTI, in a six-way-cross-shaped tube at the center of the magnetic coils assembly that separates the VTI

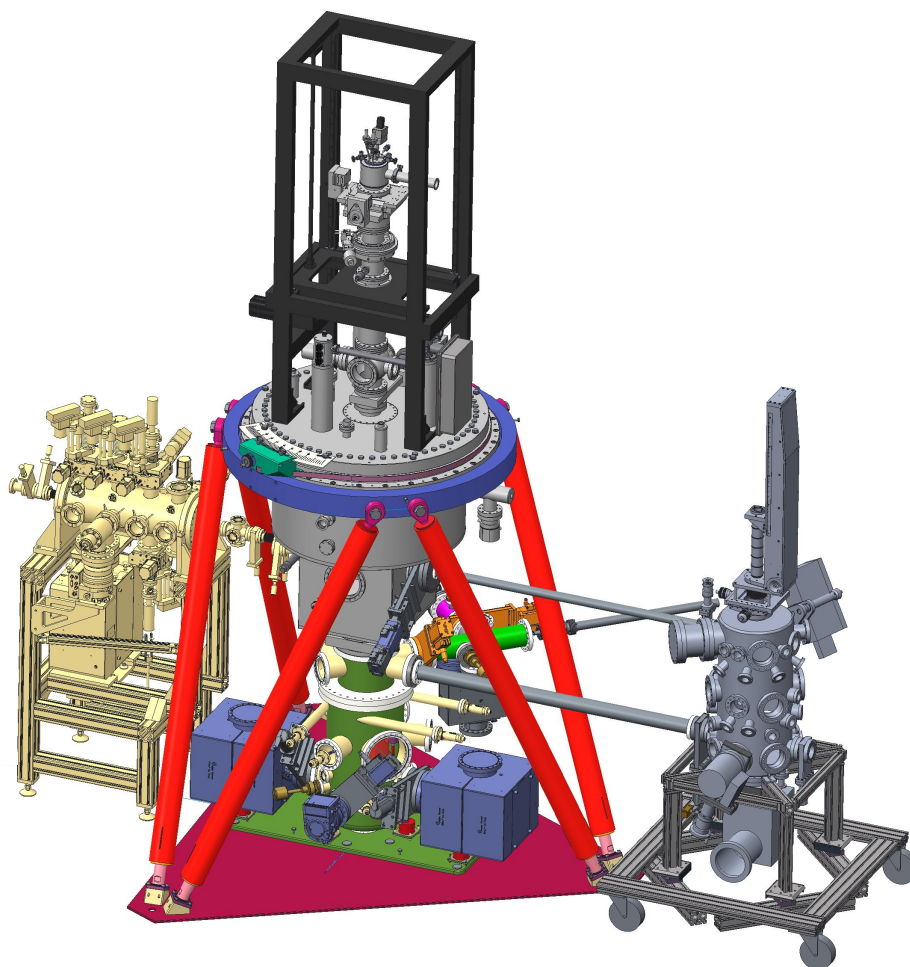


Figure 2.6: The three main chambers (Deposition Chamber in grey to the right, Detector Chamber in green, and Magnet Chamber above it) and the Characterization Chamber in yellow.

from the liquid helium bath that cools the magnet coils.

The deposition chamber, depicted in Fig. 2.7, is a dedicated sample preparation environment to produce samples in-situ. X-ray absorption measurements are available in this chamber by letting the x-ray beam pass through the Magnet Chamber and the x-ray tube, shown in Fig. 2.7. The top part of the chamber, where the x-ray tube is, also contains a multichannel plate (MCP) Low-Energy Electron Diffraction (LEED)/Auger system, a quadrupole mass spectrometer (QMS), and a quartz microbalance. The LEED/Auger system can be used for checking the integrity of the single crystal substrates and deposited films, as well as self-assembled molecular systems with periodic arrangements. The QMS

can be used to check the chemical composition of sublimated materials from the evaporators in a ballistic mode, in addition to the normal gas mass spectrometry. The quartz microbalance is used primarily to auxiliate with the deposition of metal films, as the molecule evaporators, to be discussed soon, have built-in quartz microbalances. The space to install Medium-Energy Electron Diffraction (MEED) and Magneto-Optic Kerr Effect (MOKE) equipment is also available, but these have not been installed at the moment.

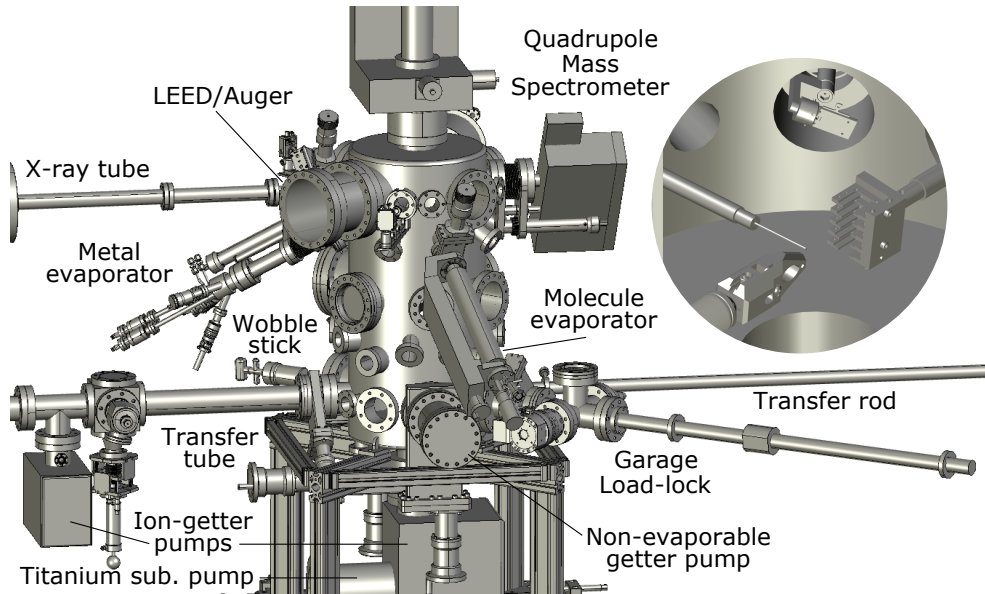


Figure 2.7: Deposition chamber with the transfer tools in the inset, showing the grabber, the screwdriver, the shuttle, and the garage.

While the top part of the chamber is dedicated to the characterization of samples, the middle part is used for the deposition equipment. It contains a four-pocket Electron-Beam Evaporator (EBE) and three valves that can be connected to different deposition equipment, such as molecule evaporators and chemical dosers. A four-pocket molecule evaporator is also in development. The angle of most flanges in this middle section is set to 45° , so that the focal point of the evaporators is at the same height as the x-ray and electron beams, as well as the QMS and quartz microbalance. Gas bottles may be attached here to be used in the film growth or cleaning procedures, with oxygen and propylene being the most used in our preparations. Argon gas is fed directly into the ion-source, also located in the middle section, to be used in the sputtering of the substrates. A large viewing window in this section allows for a clear view of the interior of the chamber. The bottom part of the Deposition Chamber contains the transfer

tools, shown in the inset of Fig. 2.7, and the vacuum pumps. The chamber's vacuum is generated by a turbo pump, an ion getter pump, a non-evaporable getter pump, and a titanium sublimation pump, resulting in pressures in the mid 10^{-10} mbar range.

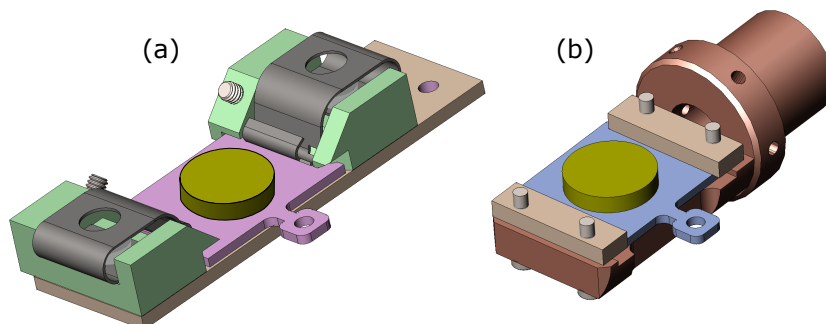


Figure 2.8: The Deposition (a) and Magnet (b) chambers sample holders.

The manipulator can take samples between the different sections of the chamber, with the sample holder depicted in Fig. 2.8(a). This sample holder is designed with titanium leaf springs for quick loading and unloading of the flag-style sample plates where the substrates are mounted. It can go down to temperatures below 100 K with its nitrogen cooling system and is connected to a high sensitivity ampere meter for the recording of the TEY in x-ray measurements and sputtering. Thermocouples are placed above and below the sample for accurate temperature reading. Fig. 2.8(b) shows the sample shuttle, where the sample plate is placed for the transfer between the Deposition and the Magnet Chambers. The shuttle is screwed into the transfer rod and the VTI of the Magnet Chamber with an M10 bolt connection. In the shuttle the sample is secured in brackets tightened with screws, to avoid movements when it is subjected to high magnetic fields in the Magnet Chamber. The screwdriver is shown in the inset of Fig. 2.7, along with the wobble-stick grabber, the shuttle mounted on the transfer rod, and the garage. A rotatable garage is also available in case there is any additional sample preparation that should be done in the load-lock requiring the removal of the sample plates from the garage in the load-lock without breaking the vacuum.

2.4 Sample preparation

2.4.1 Cleaning Au and Cu substrates

The substrate is cleaned under ultra-high vacuum to avoid contamination before the deposition of the molecules. The cleaning process consists in a few

cycles of sputtering and annealing of the single-crystalline substrate in the case of the Au and Cu substrates. The sputtering step mechanically displaces impurities that might be on the surface of the crystal by bombarding it with accelerated Ar^+ ions. The Ar^+ ions are produced by letting the Ar gas in the chamber, to a partial pressure of usually about 7×10^{-6} mbar. The ions are produced in an ion source, where electrons are extracted from a hot filament and ionize the Ar atoms. A high voltage of about 1 to 2 kV is applied to accelerate the Ar ions towards the substrate to be cleaned. The angle between the ion beam and the surface of the substrate is set to about 40° in order to yield optimum sputtering rates. This procedure leaves the substrate in a rough state and requires that it is followed by the annealing of the crystal for a period of 20 minutes in order to obtain the original surface structure. The annealing temperature depends on the crystal, but for Cu and Au crystals, the temperature used was around 900 K. This sputtering/annealing cycle was repeated as necessary in order to obtain the clean crystal surface, sometimes checking with LEED to guarantee a well-ordered structure. If the crystal had not been taken out of the chamber and the cleaning was only to remove molecules previously deposited, one cycle was usually enough, otherwise three cycles were done.

2.4.2 Cleaning Ir and W substrates

The cleaning process for the Ir and W substrates is different than for the softer metals. In the case of Ir, a sputtering step was also sometimes initially used to remove the light impurities on the surface of the crystal. For the W crystal, however, this step was skipped as the subsequent steps also cause the desorption of the molecules. The second step in the cleaning process of these crystals is the mid-temperature annealing in an O_2 atmosphere, or oxygen burning. A highly pure oxygen gas is let into the chamber, up to an O_2 partial pressure of 2×10^{-6} mbar, while the crystal is annealed up to a temperature of 1300 K for a period of 10 minutes. The objective in this step is to remove carbon atoms from the surface, as they have a tendency to segregate into the bulk of the crystals if this step is skipped. The surface carbon atoms react with the O_2 gas, forming volatile CO molecules that desorb from the substrate. Following the oxygen burning, the O_2 is removed from the chamber and the crystal is annealed to higher temperatures for shorter times, usually about 10 seconds, called flashing. In this process, the other impurities that were not removed, as well as oxides and atomic oxygen that were added during the oxygen burning are desorbed from the substrate. The flashing temperature depends on the substrate, for iridium

1600 K was used, while for tungsten it was 2200 K. These steps were repeated as necessary, with two cycles being the usual.

2.4.3 Graphene growth

The most popular technique, and the one used here, for the growth of graphene layers is the chemical vapor deposition (CVD) method. In this process the substrate, after being cleaned, is kept at an elevated temperature while a hydrocarbon gas is let into the chamber. In our samples, either propylene (C_3H_6) or ethylene (C_2H_4) were used. The substrate was kept at 1400 K, and the partial pressure of the gas in the chamber was $p_{hcg} = 2 \times 10^{-6}$ mbar. The high-temperature substrate acts as catalyst to promote the dissociation reaction of the hydrocarbon gas molecules. The carbon atoms remain on the surface while the hydrogen desorbs due to the high temperature. The details of the graphene growth will depend on the substrate. For metals with a low carbon solubility, such as Cu, the graphene formation will consist mainly of deposited carbon atoms directly forming bonds on the surface. For these metals the graphene synthesis is usually a surface-mediated self-limiting growth process [50]. Fig. 2.9(top) shows this situation. As the dissociated carbon atoms cover the surface of the substrate, the reaction stops, resulting in no more carbon than required for a single layer being deposited. If, however, the substrate has a high solubility for carbon, such as Fe, most of the dissociated carbon atoms will diffuse into the substrate under the high temperatures required for the reaction and will segregate back to the surface when the substrate is cooled, as seen in Fig. 2.9(bottom). The graphene layer is then formed by the segregated carbon atoms on the cooling substrate. For this reason, this process is not self-limiting, and multiple graphene layers may be produced. In order to obtain single-layered graphene on these substrates, great care needs to be taken with the cooling rate employed after carbon dissociation/diffusion. The metallic substrates used in this work for graphene growth, Ni and Ir, have intermediate carbon solubility [50, 51], and as such the graphene growth process uses a combination of deposited and segregated carbon. The process is reasonably self limiting, as long as the correct values of annealing temperature and cooling rates are employed. In this work the substrate heating was turned off and this process was not assisted with additional cooling, so a moderate rate was used to obtain single-layer graphene on these substrates.

For the Ir substrates, the graphene growth procedure is performed directly after cleaning the substrate. The other graphene substrate used in this work was graphene on Ni/W(110). For the latter, prior to the graphene growth,

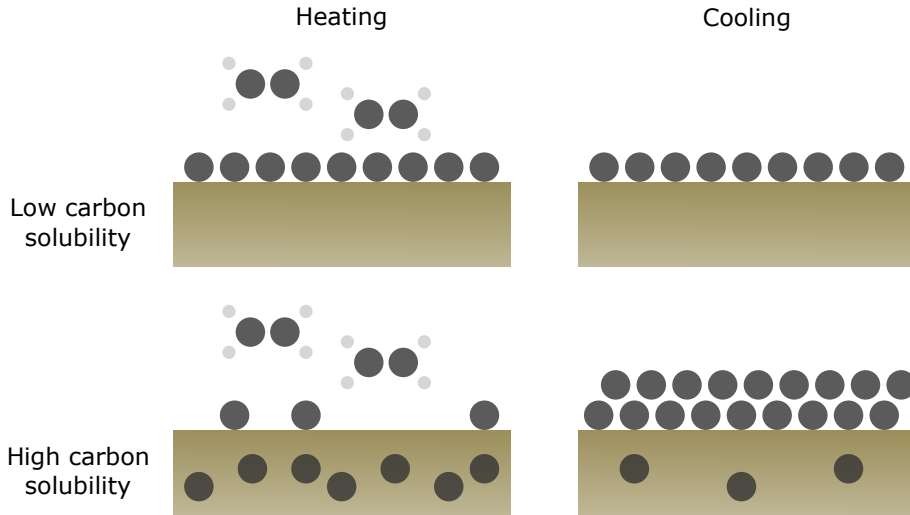


Figure 2.9: Graphene growth. Deposition (left) and cooling (right) processes for metal substrates with low/high carbon solubility.

nickel atoms are deposited on top of the tungsten single crystal. This is done with the metal EBE. The nickel is deposited on the clean tungsten substrate until a thickness of about 30 layers is obtained, so that the lattice mismatch between the Ni and the W is overcome and a Ni(111) surface is obtained. The deposition is checked with a flux measurement on the electron beam source, current measurement on the sample, and a quartz microbalance check of the deposition rate just before the deposition of the nickel. The Ni(111) structure is desirable because it matches almost perfectly to the lattice parameters of graphene. The lattice mismatch is only about 1%, causing the graphene to not alter the periodicity observed in the LEED pictures, as can be verified on the left side of Fig. 2.10, because the graphene bonds can easily adjust to the small difference in distance. For the graphene grown on Ir(111), as can be seen on the right side of Fig. 2.10, there is a big mismatch in the lattice parameters of the two structures, about 10%, causing the graphene to generate a secondary periodicity on the surface structure, given the incommensurability of the two structures. This results in the moiré pattern observed on the LEED picture seen on the top right of Fig. 2.10, where there is a secondary hexagonal structure within the primary one.

Another important factor to consider is the differences in thermal expansion of the graphene compared to the metals underneath it. As the substrate is cooled down after the growth of the graphene, a difference in the contraction coefficients may lead to wrinkles or tears on the graphene sheet. This not as significant for

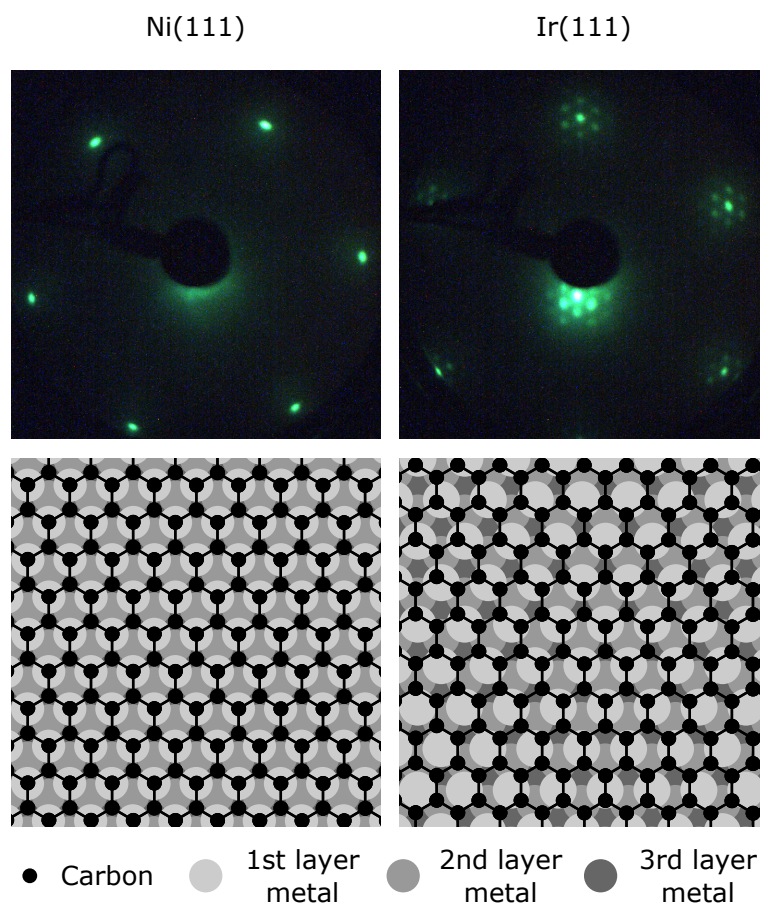


Figure 2.10: LEED and surface schematics of graphene on Ni(111), and Ir(111). The Moiré pattern is generated by the lattice mismatch between the graphene and the Ir(111) surface.

the growth through segregation, since the graphene will only be formed after the cooling process has already begun. For the substrates used here, one usually obtains for the Ir(111) substrate a graphene that contains wrinkles, while on the Ni(111) this is not as prevalent. This will result in different mechanical and electronic properties for the graphene grown on the two different substrates, which in turn results in different interactions with the molecules deposited on top of it. This will be discussed in a later chapter.

2.4.4 Molecule deposition

The molecules are deposited with a home-built molecule evaporator, under room temperature and in a base pressure of 10^{-9} mbar. The molecules in powder form are placed in a tantalum Knudsen cell and heated with tantalum wires.

Fig. 2.11 shows a schematic drawing of the deposition process. Each molecule evaporator is equipped with a quartz microbalance that is cooled by a closed running water cycle to keep the accuracy at higher temperatures of the Knudsen cell. A stable rate is first obtained, with the use of the microbalance, before the molecule evaporator is opened to the main deposition chamber. A linear motion brings the Knudsen cell into the chamber and closer to the sample, and a shutter is opened to begin the deposition.

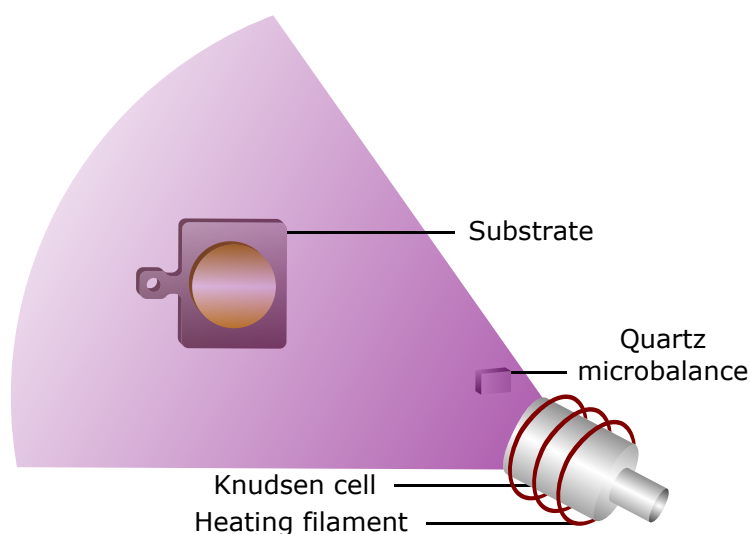


Figure 2.11: Schematics of the deposition process of the molecules. The tantalum Knudsen cell is heated by tantalum wires. The molecules sublimate in a cone onto the substrate. The rate is measured by a quartz microbalance.

A submonolayer molecular coverage is the objective, since we are interested in studying the molecules' interaction with the substrate, but want to reduce the prevalence of intermolecular interactions. The calibration of the molecular coverage is done preliminarily by the quartz microbalance, but the deposition is made in steps, so that the coverage can be checked with XAS. The intensity of the main peaks of the XA is then compared to previous measurements of known coverage, and adjustments are made to the deposition rate to obtain the desired coverage, usually between 0.4 and 0.8 ML, with 1 ML being the situation when the crystal surface is covered by exactly one layer of molecules.

2.5 X-ray absorption measurements

The XA measurements are taken in Total electron Yield, which means that all the current generated on the sample by the photon absorption and electron cascading effects, described in the previous chapter, is recorded. The recorded current will be higher for photons with energies that match the absorption energy of the core electrons of the edge we are interested in. The increased absorption results in higher currents, and the ampere meter records peaks at these energies. The raw spectra obtained in this way are normalized to both the spectra recorded by the normalization gold grid and the pre-edge value of the sample spectra, so that in the end one obtains the spectra with a base value 1 and peak heights given by the percentage increase from the pre-edge. The final spectra is sometimes normalized a third time to reference spectra of the bare substrates, if these have high or bending absorption profiles. For the measurements of the magnetization curves, full spectra of the pre-edge region are taken with varying magnetic field, in order to normalize out electron extraction differences caused by the changing field. This change in the electron extraction can be very significant for zero magnetic field, so it is also usual to apply very small fields that have no considerable effect on the properties of the molecules, but improve the signal-to-noise ratio by a significant amount. All the measurements are performed under Ultra-High Vacuum (UHV). The benefit of UHV is mainly twofold: It protects the surface against impurities, such as oxygen and water, that might alter the properties of the materials considerably, and it allows the utilization of x-rays more flexibly, as soft x-rays are strongly absorbed in air. In order to generate UHV, the combination of several vacuum pumps are used and the chamber is heated in a "bake-out" process that removes gas molecules from its walls, where the majority of them accumulate [52].

When studying molecules with synchrotron radiation, it is imperative to be mindful of the condition of the molecules, as they can sometimes be easily damaged by the x-ray beam. Fig. 2.12 shows an example of a molecular sample that was subjected to radiation damage from the x-rays. The differences might seem small in the spectra, but depending on the sample, could have significant effects in the magnetic and electronic properties of the material. In the example of Fig. 2.12, a molecular nanowire composed of europium, the damaged sample is paramagnetic, while the pristine molecular system is ferromagnetic [53]. The damage to the molecules is caused mostly by the secondary electrons produced in the cascading effect of the substrate photon absorption process [37, 54], so this is sometimes attenuated by our choice of substrates, by choosing ones with lower

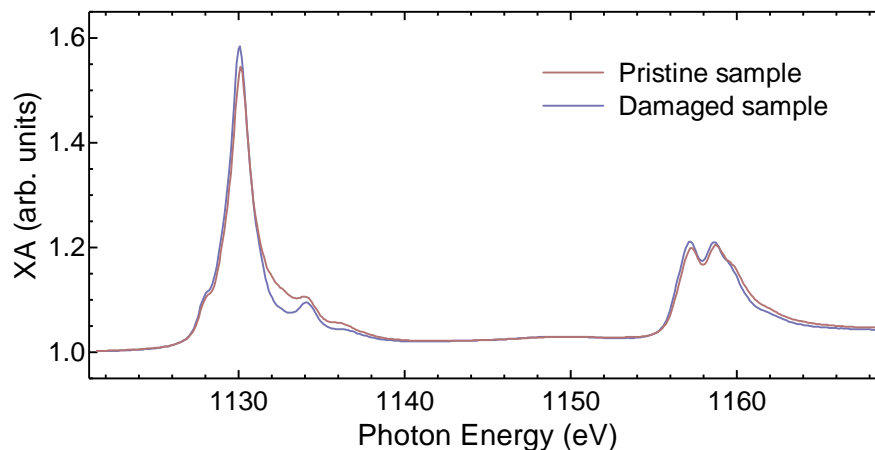


Figure 2.12: Example of the changes to the absorption spectrum of a radiation damaged molecular system.

absorption cross-sections for x-rays. When that is not possible, the attenuation has to be done directly on the flux of the incoming beam. This can be achieved, as mentioned before, through the placement of attenuation foils in the path of the beam, or by decollimating the beam to reduce the flux density. These two options reduce the intensity of the signal obtained, so care must be taken in order to obtain good signal to noise ratios when employing these methods. With the reduced flux necessary to keep the molecules undamaged and the small coverages desired for the study of individual molecules with little influence of intermolecular forces, a very sensitive measurement of the small currents produced from the absorption processes is required. A resistance higher than $10\text{ G}\Omega$ is necessary between sample and ground.

ON-SURFACE REACTION OF METALLOPORPHYRIN MOLECULES

3.1 Introduction

Porphyrins are an ubiquitous class of molecules in nature. The main function of naturally occurring porphyrins is to bind metals, forming coordination complexes, which are to be major components in a variety of chemical and biological processes [55]. They have a macrocyclic ring composed of four pyrrole groups, two with protonated and two with unprotonated nitrogens, connected by four methine bridging groups. Fig. 3.1a shows the porphine, the parent compound of the porphyrins, with no substituted ligands. Variations of this basic structure with substituted ligands give rise to the many possible different porphyrin molecules.

While the porphyrin molecules are usually very planar, deformations in this planarity may arise from the addition of substituted ligands, binding of differently sized metals and axial ligands, or even the simple protonation of the central unprotonated nitrogens [55]. Once a metal is bound to the center of the molecule it is fourfold-coordinated to the nitrogen atoms in the plane of the macrocycle, leaving above and below two coordination sites free for the metal to bind to additional axial ligands or surfaces. This contributes to the stability of the porphyrin on crystal substrates and increases the opportunities to tune the electronic and magnetic properties. One of the most remarkable features of these metal complexes is the ability to drastically modify the properties of the coordinated metal by relatively small changes in the molecule's macrocycle or

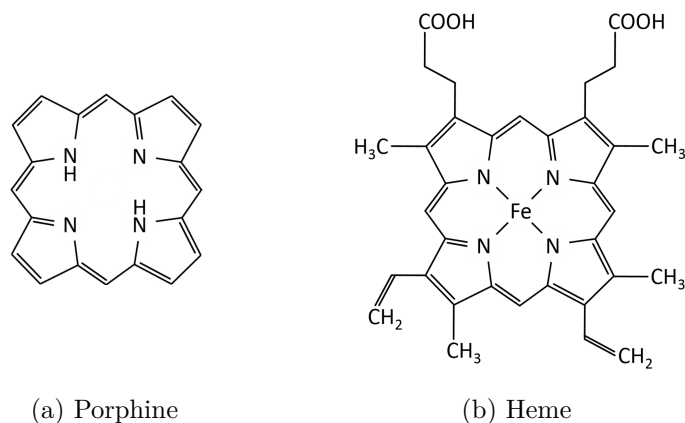


Figure 3.1: Schematic representations of porphyrin-related compounds

axial ligands, which in turn are frequently sensitive to changes in the environment of the molecule. In nature this allows, for instance, the metal to interact with oxidizing agents without irreversibly changing their oxidation state and to perform tasks unattainable by the isolated metal ion. This is the case for heme, Fig. 3.1b, an iron porphyrin molecule with many biological functions, chiefly among those the transport of gases. In humans and similar aerobic organisms, heme binds oxygen gases in the lungs, where the abundance of oxygen and lower acidity promotes a higher oxygen binding coefficient to the iron, and releases it in other body tissues, where the higher concentration of carbon dioxide promotes an increase in the acidity of the blood by reacting with water [56]. This flexibility in the physical properties of the central metal atom is among the greatest strengths of the porphyrin class of molecules, and the main reason why synthetically produced porphyrins are avidly studied in pursuit of novel biological and technological applications.

The octaethylporphyrins, or OEP for short, are the first class of porphyrins discussed in this chapter. The iron-binding OEP molecule is the FeOEP, shown in Fig. 3.2a. It was observed [16, 57] that the FeOEP on different substrates, when subjected to annealing temperatures of the order of 500 K, undergoes a gradual reaction that causes the ethyl groups to close into benzene rings, eventually forming four benzene rings from the intramolecular reaction of all eight ethyl groups. The porphyrin that results from these reactions is the tetrabenzoporphyrin, TBP, and the CoTBP, when it is binding cobalt, is illustrated in Fig. 3.2b. The TBP molecules, while having an obviously greater thermal stability, present a perfect opportunity to study the effects of subtle changes in the porphyrin macrocycle and their consequences to the properties of the central metal ion.

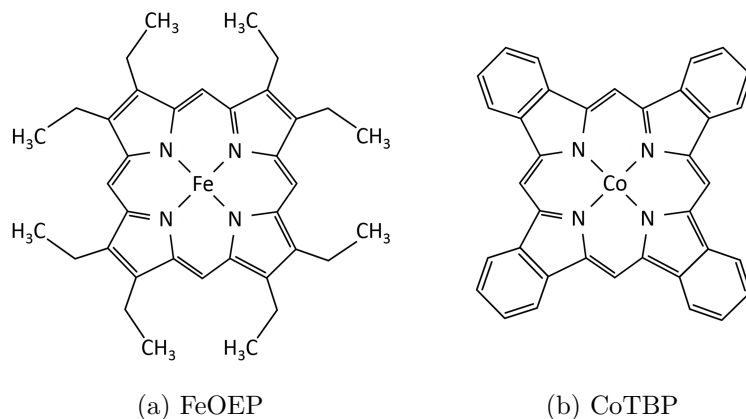


Figure 3.2: Schematic representations of porphyrin molecules studied in this work.

The reaction is not limited to a single substrate as discussed, and it is also not limited to a single metal ion. The confirmation that the reaction has indeed taken place can be asserted from the significant changes to the nitrogen atoms' electronic structure, as can be seen from the nitrogen K edge XAS taken for the different molecules. The ring-closure reaction process, illustrated in Fig. 3.3 in a simplified way for one ring, is in fact a three-step process in which first a dehydrogenation of neighboring ethyl groups promotes a bond to be formed between them, generating a six-membered carbon ring, followed by a second dehydrogenation process that completes the formation of a benzopyrrole unit and reestablishes the aromaticity of the molecule [16]. This process is repeated for all the other ethyl groups individually, until the TBP macrocycle is formed. The stability of the benzopyrrole unit is very high, making this intramolecular reaction irreversible, and the enhanced planarity of the TBP macrocycle caused by the absence of the freer ethyl groups is likely to promote modifications on the ion/substrate distance and a subsequent variable amount of interaction between the metal ion and the substrate. This adds an additional layer of influence to the physical properties of the metal ion in addition to the macrocycle ligand modification.

In this chapter, FeOEP and CoOEP molecules as well as their ring-closure reactions and resulting TBP molecules will be studied on a variety of substrates. The objective is to understand how the different environments influence the electronic and magnetic properties of the molecules and what this can tell us about the reaction and the molecules themselves. It will be shown that in some cases the reaction can drastically alter these properties, while in others no change

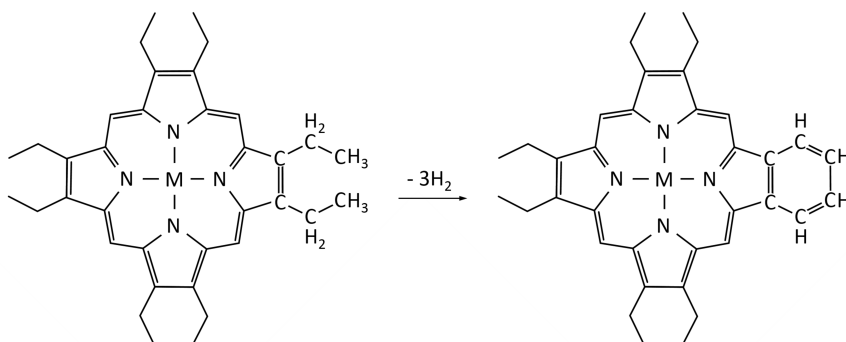


Figure 3.3: Schematic representation of the closure reaction. The annealing process causes a series of dehydrogenation reactions and the formation of covalent bonds between carbon atoms from neighboring ethyl groups, generating a benzopyrrole unit.

is verified to them. Similar changes can be obtained for the same OEP complexes, just by varying the substrate. Between TBP molecules, such variations were much less significant, attesting to the flexibility of the ethyl groups of the OEP molecules to adapt to the different conditions of their environment.

3.2 Fe porphyrins

3.2.1 Fe porphyrins on Au(111)

The molecules presented in this section were synthesized as dipyrindine complexes, FeOEP(Py)₂. The sample was prepared under ultra-high vacuum by sublimating the molecules from a Knudsen cell heated to a temperature of 500 K after 5 hours of degassing at 470 K to ensure the loss of the pyridine ligands. They were deposited at room temperature on a Au(111) substrate, cleaned beforehand by argon sputtering and annealing cycles, to a submonolayer coverage of 0.9 ML. The coverage was checked with a quartz microbalance and crosschecked with intensity calibration of the iron, nitrogen, and carbon edges with previous works [58]. The measurements were taken at low temperatures of around 4.5 K, unless stated otherwise.

The ring-closure reaction was activated by annealing the sample to a temperature of 600 K. The annealing temperature used here is higher than the complete reaction temperature of 550 K recorded by Heinrich et al. [16] so as to ensure the

complete reaction has taken place, given there is no access to scanning tunneling microscopy (STM) measurements during the XAS experiments. The nitrogen K edge spectra (Fig. 3.4) display a clear difference in the electronic structure of the molecules before and after the annealing process. This is to be taken as confirmation that the ring-closure reaction has taken place for future experiments with different samples than the ones previously measured in STM. While the first major peak observed seems to be fairly independent of the molecule transition, the second peak is shifted to lower energy values, and its overall intensity is diminished. Although not noticeable under grazing incidence, the reduction in signal intensity related to σ^* orbitals is clearly visible in the spectra of the magic angle measurements. This overall reduction in the signal intensity, visible in the spectra for 20° (15%) and 55° (33%), indicates a charge transfer to the nitrogen atoms of the molecule.

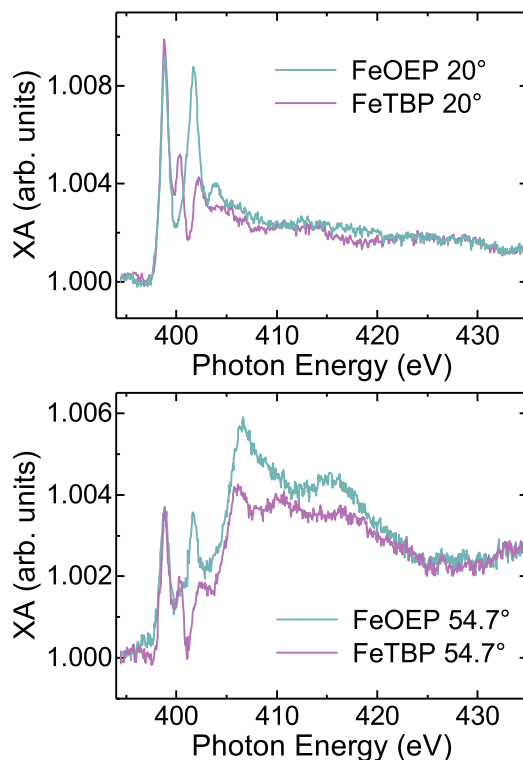


Figure 3.4: Nitrogen K edge XAS for grazing and magic angle of the molecules on Au(111) before (FeOEP) and after annealing (FeTBP). Taken at room temperature.

The electronic structure of the iron center of the molecules is seen in Fig. 3.5 to be significantly changed by the annealing process, most notably by the energetic

contraction of the Fe L_3 edges on the FeTBP for different incidence angles. The peak energies are brought closer together, with the lower energy features shifting towards higher energies and the higher energy ones displaying a redshift. This contraction could mean a direct shift of the energy levels separation of the different valence orbitals of the iron ion, in turn caused by ligand field changes stemming from the reaction. The shift could very easily lead to a reorganization of the electron charge distribution in such a way that the higher-energy orbitals of the FeTBP molecule end up more filled than in the FeOEP due to a weaker ligand field splitting. This situation would lead to an increase in the spin magnetic moment of the iron ion. Analysis of the integrated intensity shows that there is a decrease for 20° angle of incidence, while the integrated intensity for 90° incidence angle is increased by a less significant amount. The charge density distribution is 10% more anisotropic after ring closure. Due to the insignificant increase (2%) in the integrated intensity for normal incidence, the differences in the spectral shape for the different molecules under this incidence are attributed to charge reorganization between different in-plane orbitals and energy level shifts. This and the more significant decrease (8%) in the integrated intensity for grazing incidence points to a very small charge transfer to the out-of-plane orbitals of the metal center of the FeTBP molecule and to increased overlap of the wave functions with the substrate, although this is inconclusive just from the XAS results.

It is interesting to note that when taken at room temperature, the XAS of the FeOEP molecules displays a line shape that more closely resembles the FeTBP than the FeOEP at lower temperatures, as can be verified in Fig. 3.6. This indicates that the highly flexible ethyl groups are affected by the temperature in a way that seems to be, at least to a certain degree, equivalent to the ring closure. It is, however, not permanent as the ring-closure reaction, given that the two states can be accessed by simply going from room to low temperature. This indicates that no ring closure takes place at room temperature, and possibly means that the ethyl groups adopt a more planar configuration than in the lower temperature FeOEP, while the hydrogen atoms remain bonded to the carbon atoms, blocking the formation of the covalent bonds between the neighboring ethyl groups. This would enable both a different level of interaction with the substrate or simply a ligand field change that promotes the reconfiguration of the energy levels distribution of the iron ion. When the temperature is further increased the dehydrogenation process takes place and the newly formed covalent bonds force the structure to remain the same even at lower temperatures in FeTBP. Related reversible phase transitions have been reported for porphyrin

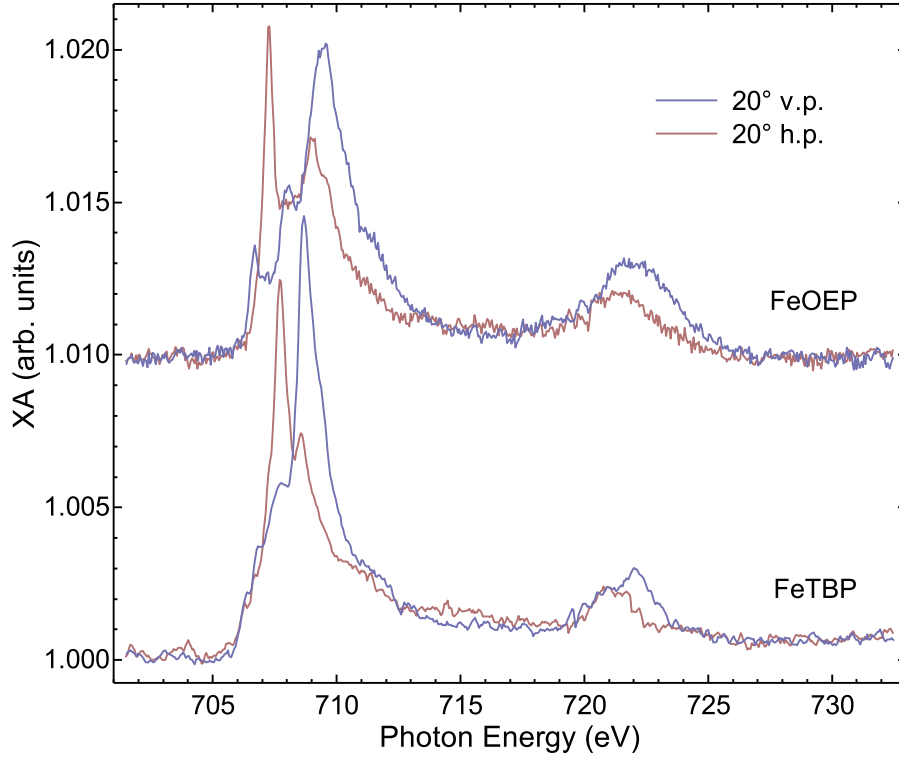


Figure 3.5: XAS of the iron L edge for normal and grazing incidence angles of the X-rays for FeOEP and FeTBP on Au(111), taken at 4.5 K. The FeOEP spectra were vertically shifted for clarity.

molecules deposited on copper [59]. In this study the molecular organization under lower temperatures is seen to change from a hexagonal to a herringbone arrangement, and back to hexagonal upon increasing of the temperature again. The change is attributed to a modification of the tilt angle of the molecules' ligands. This change in the tilt angle of the ligands could very reasonably be expected to occur on the OEP molecule, given the spectra taken at room temperature show a stronger resemblance with the TBP under low temperature, as discussed.

Density functional theory calculations with additional strong Coulomb correlation (DFT+ U) were carried out by Prof. Ehesan Ali from the Institute of Nano Science and Technology, in India, and Prof. Peter Oppeneer from Uppsala Universitet, in Sweden, using the DFT+ U approach, and adopting the generalized gradient approximation (GGA) for the exchange-correlation function. The calculated magnetic moments on the central Fe atoms are 1.96 and 2.09 μ_B , respectively, for single molecule FeOEP and FeTBP, resulting in a spin $S \sim 1$

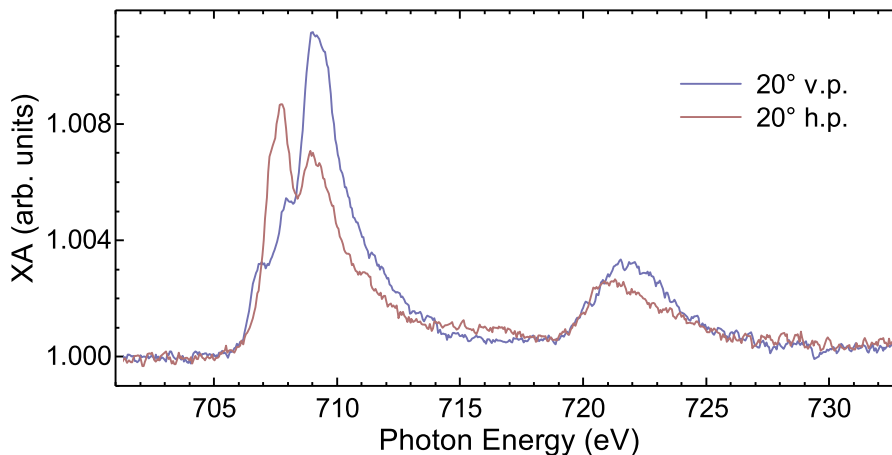


Figure 3.6: XAS of the iron L edge for normal and grazing incidence angles of the X-rays for FeOEP on Au(111), taken at room temperature.

for both molecules. Due to the differences in the ring structures, however, a significant difference is observed in the ordering of the $3d$ orbital energies (see Fig. 3.7(a) and (b)). The differences between the electronic structures of FeTBP and FeOEP are mainly due to the strained, non-planar macrocyclic structure of FeOEP caused by the eight ethyl groups attached to the porphyrin ring, whereas FeTBP has a more planar ring structure. This difference in the ring structure is reflected in the m_l -resolved density of states (DOS) for the central metal atom as well.

When the calculations are performed with the Au(111) substrate, changes are observed in the electronic structures of both molecules, particularly in the d_{z^2} orbital, that change from completely and partially occupied for the FeOEP and FeTBP, respectively, to a broad, featureless DOS structure when the molecules are placed on the Au substrate, with the FeOEP molecule exhibiting greater substrate interaction through this orbital than the FeTBP, as evidenced by the larger relative broadening observed in the DOS (Fig. 3.7(c) and (d)), since in the free molecules the FeOEP d_{z^2} peaks are limited to below the Fermi energy. This reveals that the main substrate interaction in the molecules is mediated by the d_{z^2} orbitals, and the greater interaction of FeOEP can be attributed to the calculated distance of this molecule to the first Au layer, $d_{Fe-Au}^{OEP} = 2.53 \text{ \AA}$, while in the case of FeTBP, this distance is $d_{Fe-Au}^{TBP} = 2.88 \text{ \AA}$. The distance from the Fe to the nearest Au atom, shown in Table 3.1, also demonstrates this difference. Thus, there is an additional likelihood of electron transfer between molecule and substrate for FeOEP, that has a completely filled d_{z^2} orbital in the gas phase, in

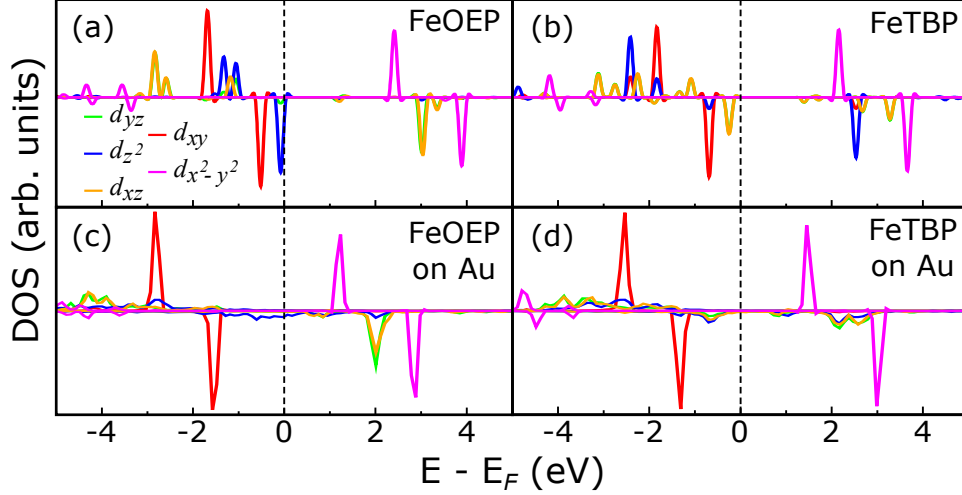


Figure 3.7: DFT+ U -calculated 3d-orbital DOS plots for FeOEP (a), FeTBP (b), FeOEP on Au(111) (c), and FeTBP on Au(111) (d). Positive and negative orbital DOS is for majority and minority spin, respectively.

contrast to FeTBP, in which this orbital is half-filled in the free molecule. In the FeTBP molecule, there is a more significant change to the d_π orbitals, although their intensity is somewhat reduced on Au in both molecules. The formation of the benzene rings on the FeTBP leads to a larger π -system on the ligands of the molecule, promoting greater interaction between them and the d_π orbitals of the iron ion. Hybridization is also likely with the nitrogen atom, leading to the characteristic changes to the N K edge, seen in Fig. 3.4. Even though there are significant changes to the electronic configuration of both molecules on Au, the spin moment does not change considerably (see Table 3.1), and remains about $S \sim 1$ for both molecules.

Table 3.1: Structural and magnetic properties of FeOEP/Au(111) and FeTBP/Au(111), calculated with the DFT+ U method (at GGA-D2 Level). Given are the Optimized Fe–Au atomic distances and spin moments.

GGA-D2 optimized properties	FeOEP/Au(111)	FeTBP/Au(111)
Fe-Au distance	2.67 Å	2.96 Å
spin moments (μ_B) on Fe	2.17 ($3d$)	2.01 ($3d$)
spin moments (μ_B) on attached Au	0.02 (total)	0.004 (total)

Spin-density plots with the same isosurface value of $0.01 \mu_B/\text{Å}^3$ indicate that the electronic interactions associated with the unpaired orbitals occur through

the central metal atom and the Au substrate atoms underneath (see Fig. 3.8). The $0.02 \mu_B$ magnetic moment obtained on the Au atom underneath indicates fractional charge transfer to the central Fe atom of the FeOEP from the substrate. The shape of the spin density on the Fe atom for FeOEP/Au (Fig. 3.8(a)) reflects the information from the calculated DOS, that the out-of-plane d_π orbitals are responsible for the magnetic properties while the d_{z^2} orbital makes a bond with the substrate. The side view shown in Fig. 3.8 enables one to see how the molecule adopts a more planar structure after ring closure, with the a formation of the benzene rings by the previously flexible ethyl groups.

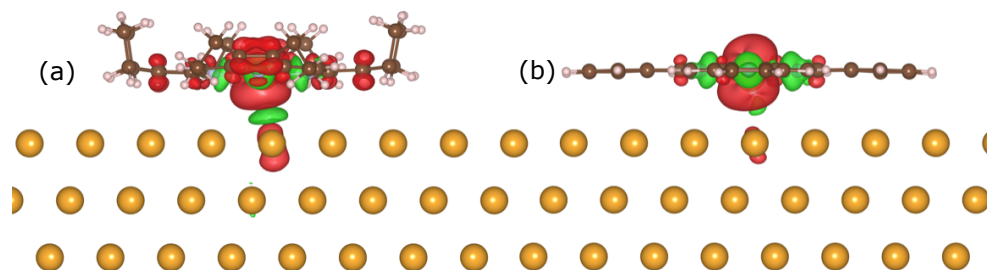


Figure 3.8: DFT+ U -calculated $3d$ -orbital DOS plots for both molecules on Au(111), FeOEP (a), and FeTBP (b). The red and green spin density isosurface with isovalue of $0.01 \mu_B/\text{\AA}^3$ indicate majority and minority spins.

The charge density analysis shows that there is no significant overlap of electron densities between the FeOEP/FeTBP molecules and the Au substrate. However, a very low charge density isosurface value of $0.01 e/\text{\AA}^3$ (see Fig. 3.9) or lower reveals weak electronic interactions between the molecule and the substrate. This interaction could not be attributed to chemical bonding interactions as sigma-electron densities of the saturated ethyl groups are involved. This is an unusual interaction and the probable reason why FeOEP is reactive in nature on the Au(111) surface and undergoes further chemical transformations to form FeTBP. Overall, the molecule-substrate interactions are rather complex in nature on Au(111) as it is associated with electrostatic (dipolar and multipolar) instantaneous charge density fluctuations due to induction and plasmonic effects.

The circularly polarized X-ray measurements were taken with a field of 6 T in the direction of radiation incidence. In the left side of Fig. 3.10 it is seen, from the vanishing XMCD at normal incidence, that the in-plane orbitals of the FeOEP molecule don't contribute significantly to the magnetic moment, while the out-of-plane orbitals do, generating a significant XMCD signal under grazing incidence. For the FeTBP there is a very small contribution from the in-plane

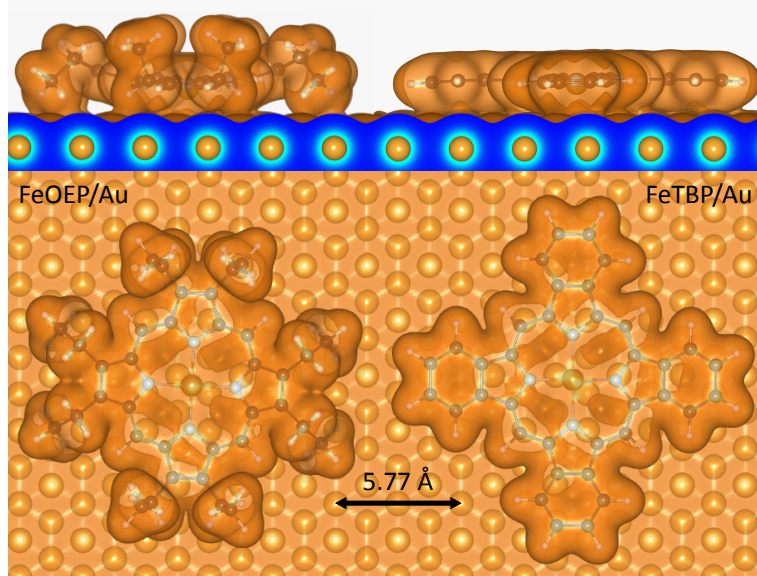


Figure 3.9: DFT+ U calculated charge density distributions plotted with isosurface value of $0.01 e/\text{\AA}^3$. The left panel is for FeOEP/Au and the right panel is for FeTBP/Au. Side views and top views are plotted in the top and bottom panels, respectively.

orbitals, as seen by the XMCD signal under normal incidence, and a significant increase in the out-of-plane contribution. These results and qualitative analysis of the angle dependence support the DFT+ U results that in FeOEP/Au there are no half-filled in-plane orbitals, confirming that the magnetic signal obtained from this molecule under grazing incidence is due to out-of-plane orbitals.

The results of the sum-rule analysis [41, 42] are displayed in Table 3.2 for FeOEP/Au(111) and FeTBP/Au(111), assuming a $3d^6$ electronic configuration for both molecules. Here, $m_S^{\text{eff}}(\alpha)$ includes the T_z term contribution, except for the magic angle (35.3°), when it cancels out. The application of the sum rules provides values of $0.69(4)$ and $1.31(5) \mu_B$ for the effective spin moment of FeOEP/Au and FeTBP/Au, respectively, under magic angle (35.3°) X-ray incidence and external field directions. These values are small when compared to the theoretical results because they are obtained from spectra taken at 6 T and 4.5 K, far from magnetic saturation for either molecule, particularly for FeOEP, as will be shown in the following discussion of the magnetization curves. Additionally, the moments obtained from the sum rules will always be underestimated due to the limit of the sum-rules' applicability to lighter transition metal ions [60], which introduces an intrinsic systematic error to the sum-rule results for the magnetic moments of Fe. The errors in Table 3.2 only

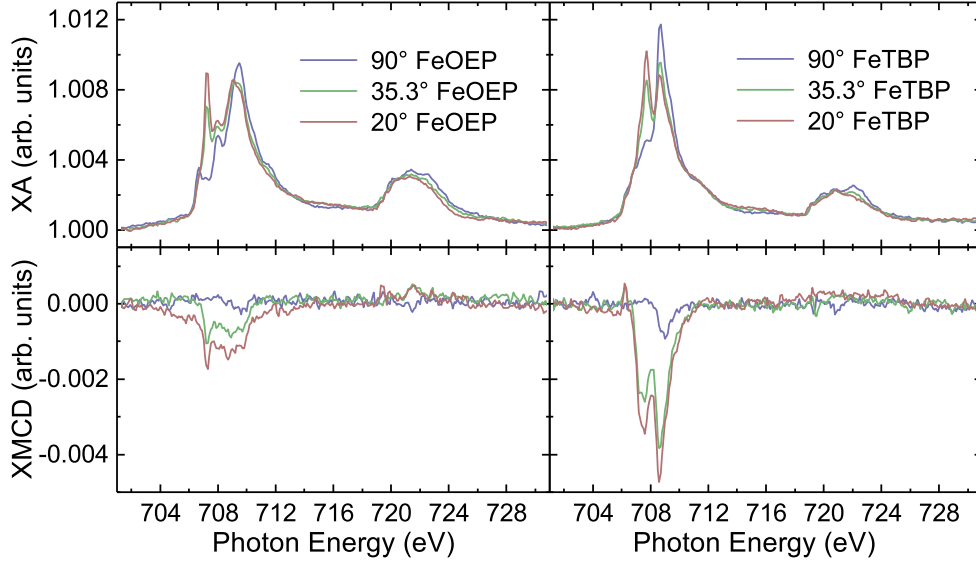


Figure 3.10: XAS and XMCD angle dependence at the iron L edge for FeOEP and FeTBP on Au(111), taken with circularly polarized X-rays at 4.5 K and 6 T.

account for the noise of the spectra, and are therefore not representative of the real errors of the measurements.

Table 3.2: Results of the sum-rule analysis for the orbital and effective spin moment of FeOEP and FeTBP under three angles of incidence of the X-rays at 4.5 K and 6 T. The values have not been corrected for saturation.

α	FeOEP		FeTBP	
	$m_L(\alpha)/\mu_B$	$m_S^{\text{eff}}(\alpha)/\mu_B$	$m_L(\alpha)/\mu_B$	$m_S^{\text{eff}}(\alpha)/\mu_B$
90°	0.03 ± 0.02	-0.05 ± 0.07	0.07 ± 0.03	0.31 ± 0.07
35.3°	0.11 ± 0.02	0.69 ± 0.04	0.50 ± 0.02	1.31 ± 0.05
20°	0.18 ± 0.04	0.88 ± 0.05	0.70 ± 0.03	1.60 ± 0.06

The XMCD signal as a function of external magnetic field is displayed in Fig. 3.11 for both molecules at grazing and normal incidence and field directions. The integrated values of the Fe L_3 edge (705 to 715 eV) XMCD signal, displayed as circles and diamonds, were taken from 0.2 to 6 T at a temperature of 4.5 K. The lines are obtained from the following spin Hamiltonian:

$$\mathcal{H} = \mu_B g \mathbf{B} \cdot \mathbf{S} + DS_z^2, \quad (3.1)$$

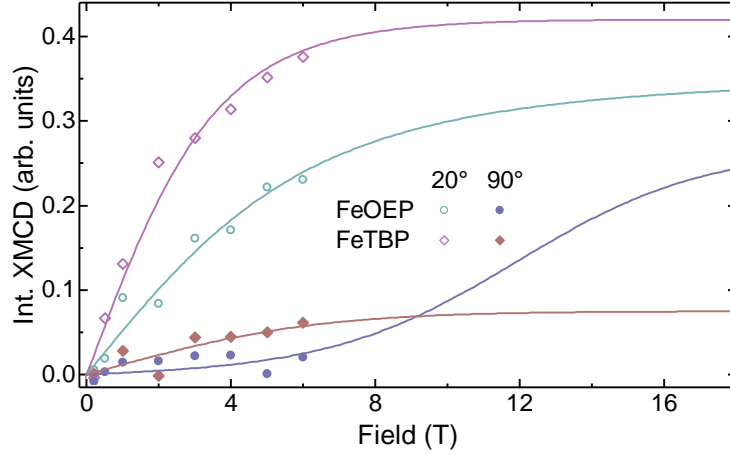


Figure 3.11: Experimental magnetization curves at 4.5 K of FeOEP and FeTBP (circles and diamonds, respectively) on Au(111) and corresponding spin-Hamiltonian fits (lines).

where only the Zeeman and the uniaxial anisotropy energy terms are considered. The first term represents the Zeeman energy (μ_B is Bohr's magneton, g is the g -factor, \mathbf{B} is the external field vector and \mathbf{S} is the spin vector), while the second one describes the uniaxial anisotropy energy (D is the zero-field-splitting parameter and S_z the spin component perpendicular to the plane of the molecule). The moment obtained from this spin Hamiltonian is further modified by the magnetic dipole term (T_z). We need to consider the effective spin moment ($m_S^{\text{eff}} = m_S - 7T_z(\cos^2 \alpha - 2\sin^2 \alpha)$) for the signal obtained from the XMCD to be properly fitted. The influence of the (T_z) term will depend on the angle between the X-rays and the surface, α , and can be ignored for the magic angle of incidence, when $m_S^{\text{eff}} = m_S$. The spin calculated by DFT+ U , $S = 1$, can be used to obtain a meaningful fit of the experimental results. This is shown in Fig. 3.11 as solid lines.

The effective spin moment is zero under normal incidence when the value for T_z is maximum, $T_z = -m_S/14$ in this case. The model used to fit the experimental magnetization curves is: $XMCD_{\text{theo}} = a|M| \cos(\theta - \alpha)(1 - T_{zsc}(1 - 3 \cos(2\theta))/4)$, where a is the scaling to the experimental signal, θ is the angle of the magnetization of the sample to the surface, and $|M| \cos(\theta - \alpha)$ is the projection of the magnetization in the direction of the measurement. $T_{zsc} = -14T_z/m_S$, so that $T_{zsc\text{max}} = 1$, and $(1 - 3 \cos(2\theta))/4$ is the angle dependence of the T_z term. The T_z term is, thus, obtained from the fit. The magnetization is obtained from the spin-Hamiltonian equation.

The higher curvature of the magnetization curves of FeTBP/Au indicates that this system is closer to magnetic saturation than FeOEP/Au. From the fit one obtains that the FeOEP molecule on Au has a strong in-plane magnetic anisotropy ($D = 1.72$ meV) parallel to the plane of the molecule, while FeTBP/Au has a weaker anisotropy ($D = 0.36$ meV) in the same direction. In addition, the fit shows that the T_z term, which has a very low value in FeOEP, increases by about four times after ring closure. The fit of the magnetization curves reconciles the values obtained from the DFT+ U calculations for the magnetic moments of the two molecules and what is observed in the XMCD results. The strong in-plane anisotropy of the FeOEP molecules almost quenches the magnetic signal observed in the XMCD for FeOEP/Au under normal incidence for lower fields, such as the maximum one measured in our experiments (6 T). The change in the magnetic dipole term is responsible for the increase in magnetic signal observed in grazing incidence after ring closure, when theory predicts no significant change in the magnetic moment between the two molecules. The smaller XMCD signal in FeOEP/Au is, therefore, not a result of a smaller moment on this molecule, but of the different T_z and anisotropy terms. While the higher T_z term in FeTBP/Au should result in a decrease of the magnetic signal observed under normal incidence, this is balanced by the change in anisotropy. In FeTBP/Au, as can be seen in the spin density plots presented in Fig. 3.8, the molecular conformation is much more planar than in FeOEP/Au. The flexibility of the ethyl groups of the OEP molecule allows for a conformation that distorts the molecular plane and brings the Fe center out of the plane of the molecule, closer to the substrate. This in turn enables a higher degree of interaction with the substrate and promotes the charge reorganization in the orbitals of the OEP molecule in a more significant way than in TBP, as described in the DOS discussion.

With the parameters obtained from the fit of the magnetization curves, one can also estimate the saturation value expected for the magnetic moments at high field. The values obtained from the sum rules discussed previously can be adjusted by the estimated saturation factor obtained from the spin-Hamiltonian fit, by extrapolating the model to large field values. This correction factor is applied to the sum-rule results obtained for the 6 T measurements, yielding $1.1(3) \mu_B$ and $1.4(3) \mu_B$ under magic angle (35.3°) incidence and external field directions for the spin moment of the FeOEP and FeTBP, respectively, in magnetic saturation. In addition to the experimental error of this result, which accounts for the bending and noise of the L edge spectra, there is an intrinsic error of about 20% in the magnetic moment value obtained from the sum-rule analysis due to the limit of its applicability to lighter transition metals [60]. This error is mainly

due to the spectral overlap of the L_2 and L_3 edges for these ions. Considering these two main sources of error, the values obtained are in agreement with an $S = 1$ system, as predicted by DFT+ U , and indicate that this is the most likely spin state for the two molecules. A second possibility, with $S = 3/2$, would require much higher values for the effective spin moment, and a third one, with $S = 1/2$, does not result in a meaningful fit of the magnetization curves with the spin-Hamiltonian model described previously. A last possibility would require an intermediary spin state, similar to the system described by Stepanow *et al.* [61] While this cannot be ruled out entirely just from the XMCD results, it is a very special scenario that is not supported by our DFT+ U results.

It is worth mentioning that experiments had been previously performed for FeOEP molecules on Cu(100) [62]. The higher reactivity of the copper substrate is expected to cause a stronger interaction with the iron ion of the porphyrins when compared to the molecules deposited on gold. The linear polarization spectra are similar to the ones of FeTBP and especially of FeOEP at room temperature, Fig. 3.6. These similarities are then taken as further indication that the changes observed after the ring-closure reaction are a result of stronger substrate-molecule interaction. The main difference between the spectra recorded on Au(111) and Cu(100) is on the peak at ~ 707.6 eV. While this peak is very prominent in the grazing-incidence spectra of the gold sample, it is reduced to a shoulder on copper. This reduction is observed in both the XA and XMCD spectra. The XMCD spectra [62] are strikingly similar to the ones of FeTBP on gold as well, apart from the aforementioned reduction of the first peak under grazing incidence. In the copper case the differences between magic and grazing incidence are nearly unnoticeable, but that is in part due to the fact that the grazing-incidence angle was 25° here. The enhancement of the XMCD signal of the FeOEP molecule deposited on the bare copper substrate as compared to the Au one appears to be a direct consequence of the stronger interaction between molecule and this substrate, and this shows that, for iron porphyrin molecules, the increased substrate interaction should promote a higher spin moment. We will see later in this chapter that this is a trend for the iron porphyrins on different substrates.

3.2.2 Fe porphyrins on graphene

Porphyrin molecules were deposited on a graphene/Ni(111)/W(110) substrate. The sample preparation is described in [58]. It starts with the cleaning of the W(110) single crystal by oxygen burning (10^{-6} mbar oxygen pressure at 1600 K

for 15 minutes) and high-temperature flashing cycles (5 flashes at 2300 K for 10 seconds each). Ni atoms were subsequently deposited by means of electron beam evaporation up to a thickness of about 20 ML, forming a Ni(111) surface. A graphene layer is then produced in a self-limiting process by cracking propylene (C_3H_6) gas molecules on a high temperature Ni(111)/W(110) substrate. The cracking was performed under a propylene partial pressure of 10^{-6} mbar and substrate temperature of 650 K for 10 minutes, followed by 10 minutes of annealing at a temperature of 750 K. FeOEP molecules were deposited on the graphene layer in the same way described in subsection 3.2.1 for the gold substrate. The annealing procedure that promotes the ring closure was also carried out in the same way.

The TBP conversion is visible from the nitrogen K edge spectra, Fig. 3.12, as discussed in the previous subsection. The resemblance to the FeOEP and FeTBP on Au(111) spectra is clear, but in the case of the graphene sample the overall absorption signal is increased after ring closure, which translates into a net decrease in the charge density of the nitrogen atoms. There is a reduction in the intensity of the second main peak of the π^* orbitals region, around 402 eV, but this reduction is less significant than the one observed for the Au(111), and is compensated by an increase in the intensity of the first peak, around 399 eV, resulting in the overall increased intensity. The effect happens in both grazing and magic angles of incidence when only the π^* orbitals are considered, and is even more pronounced when the σ^* orbitals are included. The intensity increase in the π^* region is of 12% for both the grazing and magic incidence angles. This is the direct opposite of the Au(111) case in which a net increase in the charge density is observed after ring closure.

One interesting aspect of these molecules adsorbed on graphene is that they are remarkably planar. While porphyrins have planarity as a common characteristic of their adsorption behavior on surfaces, as discussed in the previous subsection, there is usually a certain degree of buckling of the macrocycle caused by the central ion. This planarity is easily observable in the normal incidence spectra of the N K edge as remnant features in the lower energy, π^* region, around 400 eV. In the FeOEP there is only a very small peak, that points to a small deviation from planarity. This peak completely disappears for the FeTBP, as shown in the bottom panel of Fig. 3.12. It has been pointed out for similar molecules that such remnant features in normal incidence spectra might also be caused by a rehybridization with the central ion [63], indicating that even the OEP molecule might lay in a very planar geometry. It is clear for the FeTBP, however, that the molecule is lying on a plane. This high planarity is also a small indication of

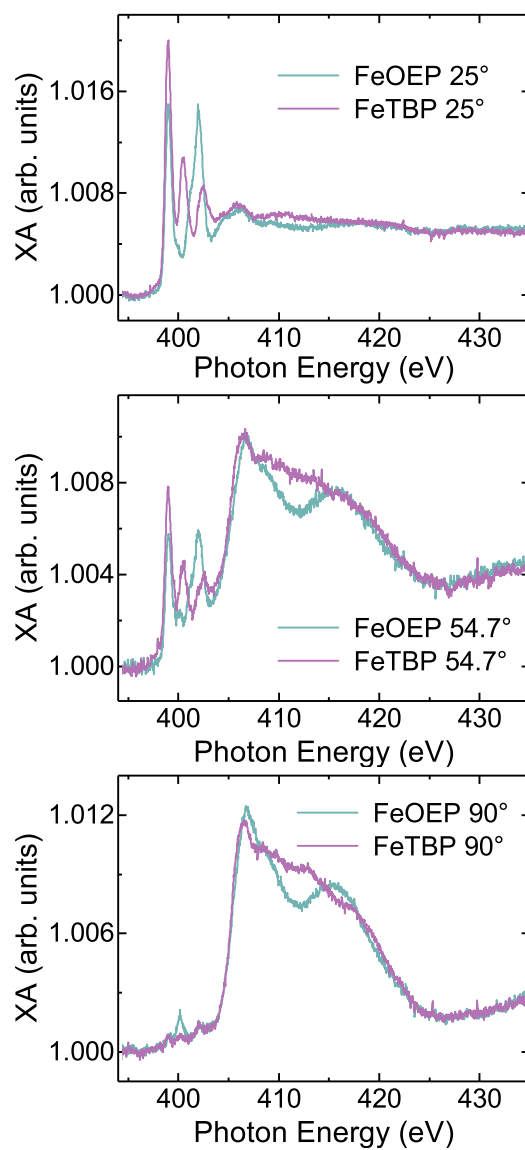


Figure 3.12: Nitrogen K edge XAS for grazing, magic, and normal angle of incidence for the molecules on graphene/Ni(111)/W(110) before and after annealing. Taken at room temperature.

a nonexistent or weak interaction with the substrate, as such interaction is likely to pull the central ion out of the macrocycle plane.

Similar to what is observed in the case of the N K edge, the spectra for the Fe L_{2,3} edges on graphene shown in Fig. 3.13 resemble the ones on Au(111). Once again, the crucial difference lies in the fact that there is an overall decrease in the charge density of the iron atom, the opposite of what is observed in the previous subsection. The integrated intensity of the grazing spectrum after ring closure displays an increase of 6% when compared with the one for the FeOEP, while in normal incidence the gain is of 3%. The increase in the integrated intensity of the grazing spectrum is mainly due to an increase in the intensity of the peak at 707.8 eV, which is a pronounced shoulder on the peak at 707.3 eV in the FeOEP spectrum. In the FeTBP spectrum, this configuration is reversed and the 707.3 eV peak becomes the shoulder, while the overall integrated intensity increases. This points to a small decrease in the charge density of the out-of-plane orbitals of the iron atom. The second main peak of the L₃ edge is more closely related to the in-plane orbitals of the iron, and it changes very little under this incidence angle. This peak is much more visible under normal incidence, when the changes due to the ring-closure reaction are very clear. It is in fact mainly composed by two peaks that can be seen more clearly in the magic incidence angle spectra of the FeOEP, when the two have roughly the same intensity. A similar thing to what is observed for the main peaks of the grazing incidence happens here, this time with the lower energy peak gaining intensity while the higher one becomes a shoulder peak. The other shoulder peaks that can be seen at higher energies mostly disappear after ring closure. The change in the integrated intensity is less than at grazing incidence, as mentioned earlier, and indicates that the charge density of the in-plane orbitals remains essentially unchanged, with a charge reorganization within the in-plane orbitals being the most relevant process.

Experiments on a related system, iron phthalocyanine (FePc) [64], have demonstrated that the interaction between the molecule's metal center and the substrate is suppressed by the graphene layer. Due to the similarity between the FeTBP molecule measured here and the FePc cited in the mentioned article, it is not unreasonable to believe they behave analogously. It is however not possible to affirm that with certainty, given that small changes to the substrate, molecule or environment tend to translate into big changes in the properties of these systems. Cobalt phthalocyanine (CoPc), for instance, seems to be capable of strongly interacting with the substrate even through a graphene buffer layer [65]. In the present case, due to the small change in the total integrated intensity of

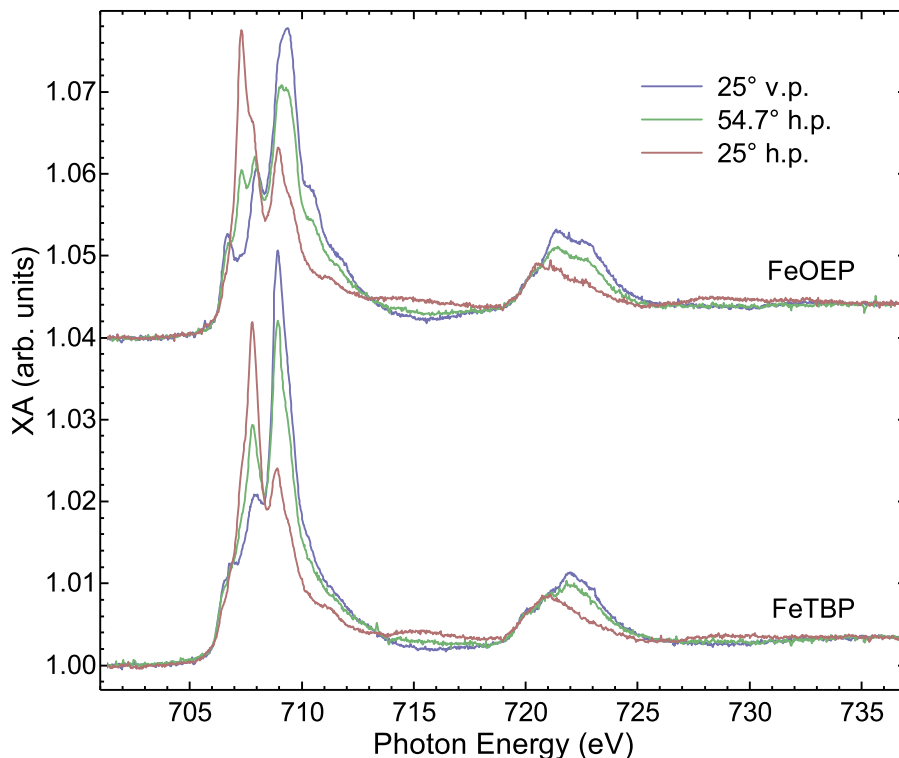


Figure 3.13: Angle-dependent XAS of the iron L edge for FeOEP and FeTBP on graphene/Ni(111)/W(110), taken at 4.5 K. The FeOEP spectra were vertically shifted for clarity.

the iron and nitrogen edges, it is less likely that a full charge transfer occurs between substrate and molecule. It is unlikely, however, that this change was caused solely by charge reorganization within the molecular orbitals, since the integrated intensity increases under magic angle incidence for both the iron (7%) and nitrogen edges. If the interaction with the substrate can be excluded, a reduction in the charge density can only be explained by electron accumulation in the outer region of the macrocycle and in the newly formed rings of the FeTBP molecule. To confirm this, one would need to measure the carbon K edge as well, and this measurement was not performed. Besides the fact that the substrate is graphene, contamination of beamline components with carbon particles is common, which would cause the measurement to be unreliable. Lastly, DFT calculations would be very helpful in determining the charge density of the molecules, but they were not yet performed for these systems.

The FeOEP molecules have been shown to couple ferromagnetically to nickel films when deposited directly on them, or antiferromagnetically through an

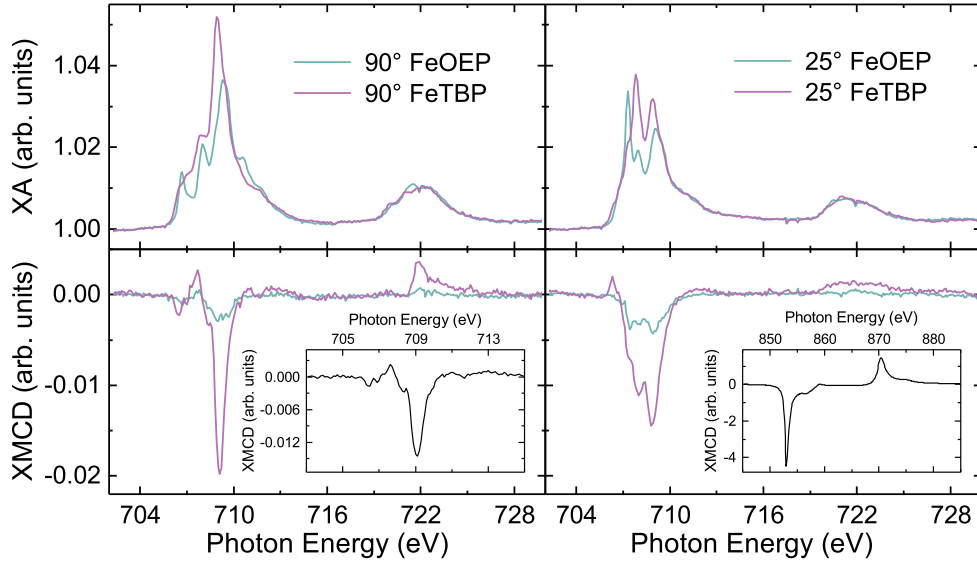


Figure 3.14: XAS and XMCD of the iron L edge under normal and grazing angles of incidence of the X-rays for FeOEP and FeTBP on graphene/Ni(111)/W(110), taken with circularly polarized X-rays at 4.5 K and 6 T. The left side inset shows the L_3 edge XMCD signal of an FeTBP molecule under normal incidence at 0.2 T. The right side inset shows the XMCD of the Ni layers.

oxygen layer [66, 13]. Similar cobalt porphyrin molecules were shown to couple antiferromagnetically with nickel through graphene [67]. The magnetic moment of the FeOEP iron center lies in the same orientation as the nickel one as can be seen on the inset on the right side of Fig. 3.14 and displays remanence when the measurements are taken close to 0 T external field, as seen in the left side inset. This proves there is a ferromagnetic coupling between the FeOEP and the nickel film through the graphene. The XMCD results are displayed in Fig. 3.14 separated by angle, so as to accentuate the differences before and after ring closure. Continuing with the comparative analysis to the Au(111) substrate made throughout this subsection, one can initially see that the XMCD trend of increasing intensity observed before is repeated here. This suggests once again that there is an increase in the magnetic moment of the system after ring closure. The difference is that, in the present case, the most significant change in XMCD intensity is observed under normal incidence, which indicates that the in-plane orbitals are important actors in this increase. In the case of the gold substrate, the opposite was observed, and the contribution of the in-plane orbitals to the magnetic moment, while present, was much smaller. The

grazing incidence XMCD signal also supports the prominent role of the in-plane orbitals in the increase of the magnetic moment, as there is a shift in the ratio of main peaks observed, making the peak around 709 eV, associated with in-plane orbitals, stand out. As mentioned earlier in this section, the charge density of the in-plane orbitals changes very slightly after ring closure, evidencing this increase in the XMCD signal must come primarily from charge reorganization within the in-plane orbitals of the metal center.

The close relation of the magnetic moment increase and the in-plane orbitals occupation can be directly associated to the proposed notion of the graphene layer acting in this case as a buffer layer that hinders the molecule-substrate interaction. The changes in the charge distribution of this system must then be assumed to be caused primarily by changes in the ligand field generated by the newfound conformation of the FeTBP molecule or by changes in the direct interaction of the central iron ion and the nitrogen atoms that surround it. It is here more likely, since the changes are verified to stem mostly from variations of the in-plane orbitals electronic occupation, that the latter possibility is the correct one. It is interesting, however, to note that the graphene layer, while acting to reduce the molecule-substrate interaction, does not manage to impede the increase in the magnetic moment observed after ring closure or the ring-closure reaction itself, which is widely regarded as surface-assisted [16, 57].

3.3 Co porphyrins

3.3.1 Co porphyrins on graphene

The preparation of this sample closely follows the one of the FeOEP molecules on graphene presented in a previous section, with only a slight increase in the sublimation temperature of the molecules to 510 K. CoOEP molecules were deposited on top of the graphene layer to a coverage of 0.6 ML. The ring-closure annealing procedure was carried out in the same way.

The ring-closure reaction is evident from the nitrogen K edge spectra once again, as shown in Fig. 3.15. The integrated intensity of the π^* region decreases by 4% for the two measured incidence angles, pointing to a very small increase in the charge density of the nitrogen atoms.

The changes in the XAS of the L edges of cobalt, however, are much less evident, as seen in Fig. 3.16. In the L_3 edge, all that can be safely affirmed is that there is a decrease in the intensity of the peak recorded at 778.1 eV and again for the peak at 781.1 eV, for both grazing and normal incidence angles.

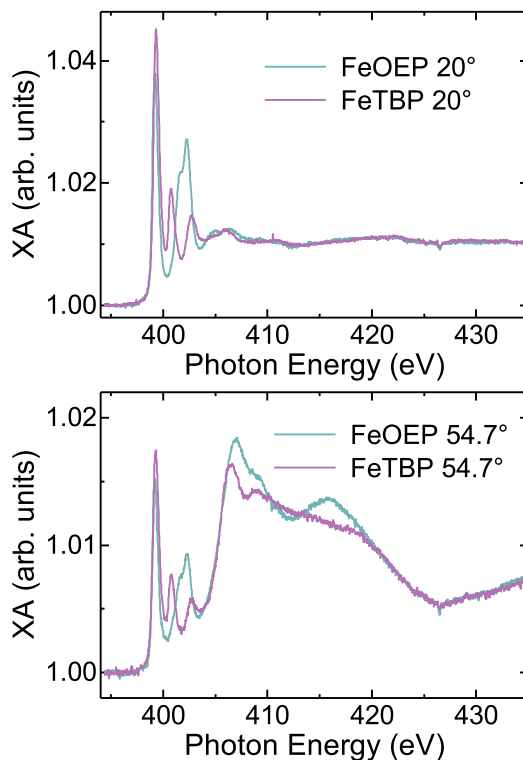


Figure 3.15: Nitrogen K edge XAS for grazing and magic incidence angles of the X-rays on graphene/Ni(111)/W(110) before and after annealing the molecules. Taken at room temperature.

The integrated intensity for the different angles tells the same story, with a decrease of 5% in grazing intensity and a negligible increase of 1% for the normal incidence. The situation here is very reminiscent of the case of the iron porphyrin on graphene presented previously, but now with an inversion in the sign of changes in charge density of the molecules, besides a reduction in the intensity of these changes. The ligand field change is also seen to be much less significant than in the Fe porphyrins on graphene, as there is very little difference in the line shape of the spectra before and after ring closure. The conclusions, however, are similar. Once again there is a hampering of the interaction of the ferromagnetic substrate and the molecule caused by the graphene. Once again this does not impede magnetic coupling.

Fig. 3.17 shows the XMCD results for grazing and normal incidence of the CoOEP/TBP molecules on graphene/Ni(111)/W(110). As discussed in the literature [67], the coupling in the case of the CoOEP in this system is anti-ferromagnetic, which persists in the case of the CoTBP, presented now. The

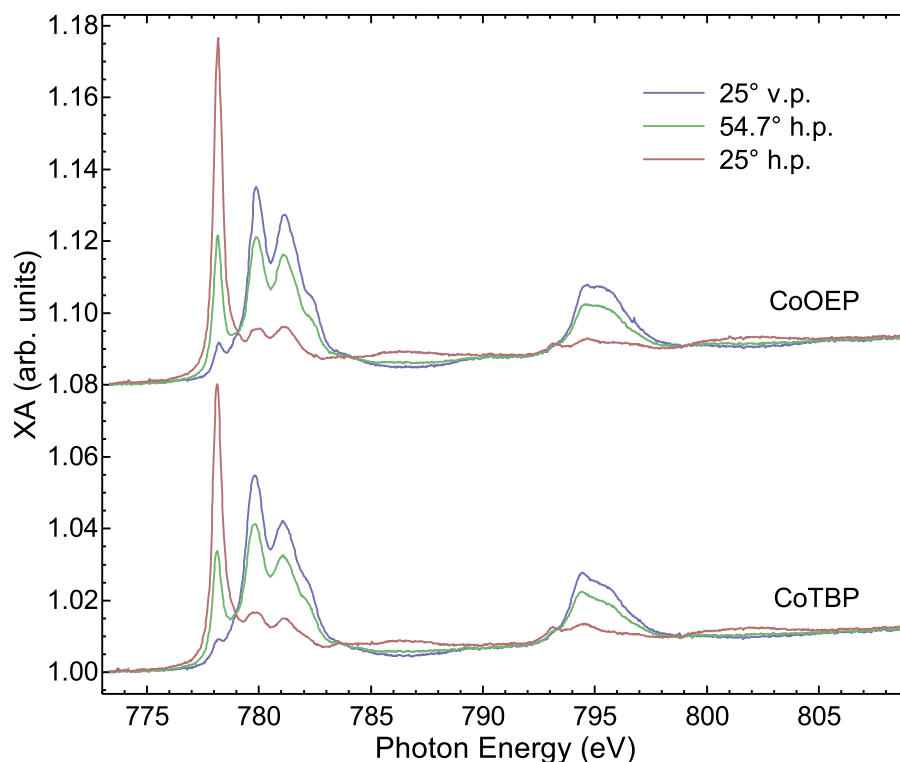


Figure 3.16: Angle-dependent XAS of the cobalt L edge for CoOEP and CoTBP on graphene/Ni(111)/W(110), taken at 4.5 K. The CoOEP spectra were vertically shifted for clarity.

changes brought by the ring-closure reaction to the magnetic properties of the molecules are limited to the reduction of the XMCD signal and consequently of their magnetic moment. This reduction is observed, as will be discussed later in this section, in all cases of the ring closure of cobalt porphyrin molecules, while the opposite happens for the iron porphyrins. One of the main differences brought by the reaction is in the molecule-substrate distance. The formation of the benzene rings from the ethyl groups of the OEP macrocycle is believed to promote greater restriction to the deviations from planarity of the molecule, and a stronger interaction with the substrate due to the favored van der Waals forces acting on the newly formed π -system. This likely results in a shorter distance between the molecule and the metal center, meaning the interaction with the substrate should increase for all of the molecules studied so far after ring closure, even if this interaction is hindered by the graphene layer in some cases. The conclusion is that the interaction with the substrate in the case of the iron porphyrins generally serves to increase their magnetic moment, while a

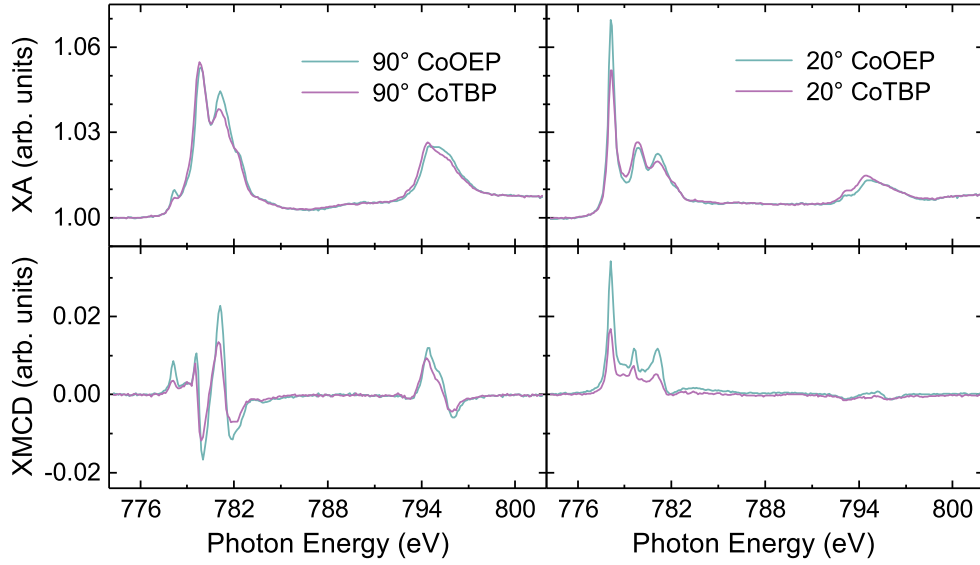


Figure 3.17: XAS and XMCD of the cobalt L edge under normal and grazing incidence for CoOEP and CoTBP on graphene/Ni(111)/W(110), taken with circularly polarized X-rays at 4.5 K and 6 T.

reduction is verified for the cobalt porphyrins, and even a quench in special cases as will be shown in the following subsection. The magnetic coupling is therefore usually highly dependent on the metal-ferromagnetic film distance. It has been suggested that the adsorption of small ligands can reduce the magnetic coupling through conformational changes to the porphyrin molecule [68]. An additional possibility is that the adsorption of the small ligand pulls the metal away from the substrate [27], thus reducing the coupling.

The coupling of the cobalt porphyrins to the nickel layers is even stronger than in the case of the iron porphyrins, as can be observed in Fig. 3.18 for the CoTBP molecules under different external field values. There is barely any discernible difference between the spectra taken at 1 T and 6 T on the two angles of incidence. It has been previously verified [58] that for the CoOEP molecule there is a negligible difference between the spectra at 2 T and 5.9 T at normal incidence, much like is observed here for the CoTBP. In the case of grazing incidence, however, a substantial variation is observed, with the external field of 5.9 T already being large enough to counteract the antiferromagnetic coupling between the Co spins and the Ni film, reducing the magnetization by 17% when compared to the 2 T field.

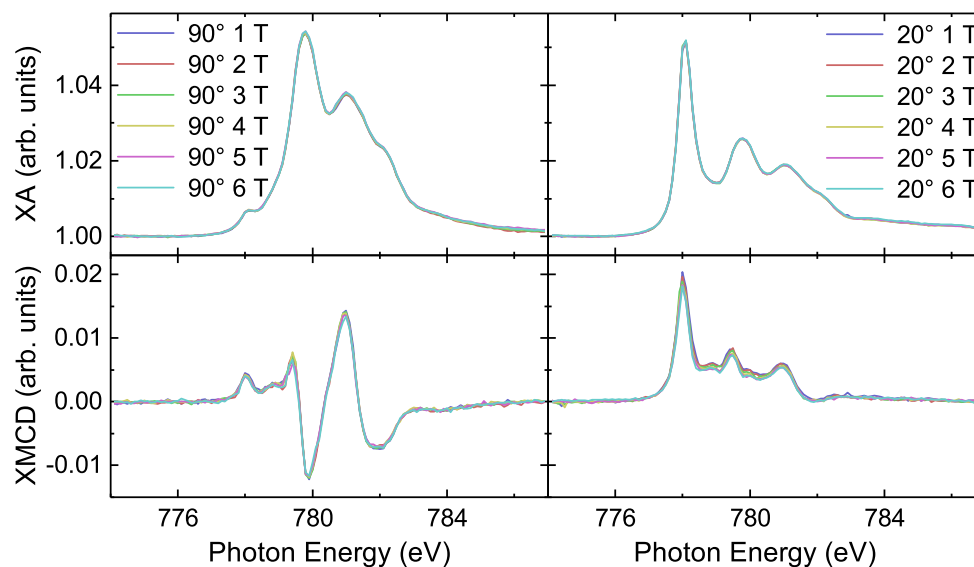


Figure 3.18: XAS and XMCD of the cobalt L_3 edge under normal and grazing incidence for CoTBP on graphene/Ni(111)/W(110), taken with circularly polarized X-rays at 4.5 K and various field values.

3.3.2 Co porphyrins on metallic substrates

In this subsection, results of the deposition of CoOEP molecules directly on four different metallic substrates are presented. The deposition took place, in all instances, under room temperature and UHV conditions. The substrates, Au(111), Au(100), Cu(111), and Cu(100), were cleaned by sputtering and annealing cycles before deposition. The STM images of the CoOEP and CoTBP molecules on Cu(100) and Cu(111), taken by the group of Prof. Dr. Katharina Franke, at Freie Universität Berlin, are displayed in Fig. 3.19. It is clear that on both substrates the molecules adsorb in a planar geometry and do not form long range structures, except for some accumulation at step edges. This is likely a result of the strong interaction with the substrate, which hinders the movement of the molecules on the surface. Additionally the separation between the molecules indicates a repulsive force, which points to charged molecules and charge transfer with the substrate. There is a stronger contrast between the central and peripheral parts of the molecule on Cu(100) than on Cu(111). It is clearly visible that for the OEP molecules on both substrates, the apparent height of the cobalt ion is lower than that of the peripheral ligands, albeit this appears to be more significant for the molecules deposited on Cu(100). This suggests that the peripheral ethyl groups are relatively higher than the central

atom in this case when compared to the molecules deposited on Cu(111). This situation could arise from either the ethyl groups pointing sharply away from the surface or the cobalt ion being closer to the substrate in relation to the molecular macrocycle. In either case the ligand field acting on the cobalt ion should be significantly different in the two situations. In the case of the TBP molecules, the central ion appears to be higher than the rest of the molecule on both substrates, indicating a slight bending of the molecule with the cobalt lifted up from the plane of the macrocycle. This, however, does not necessarily mean the cobalt ion is further away from the surface when compared to the OEP molecules. The benzene rings of the TBP molecule are expected to have a strong π -type interaction with the substrate, causing a reduction in the overall molecule-substrate distance.

From previous CoOEP experiments [69], only a fraction of the cobalt ions are seen to interact strongly with the Au(111) substrate through the formation of coordinative bonds. This is attributed to the structure of the reconstructed Au(111) surface, responsible for a more complex interaction behavior with the molecules. This is in contrast with silver surface experiments [70], when all cobalt ions were seen to interact in a strong and uniform fashion with the substrate. Ref. [69] also shows that there is a strong role played by the central metal ion in the molecule-substrate interaction in these systems. For these reasons we expect the copper substrate to interact more strongly with the molecules when compared to gold, just as was the case for the iron porphyrins discussed in the previous section.

The spectra recorded for the CoOEP molecules on the four substrates are displayed in Fig. 3.20. The spectra for the gold substrates are multiplied by four for a better comparison with the copper substrate results. The results for the two gold substrates, Au(111) and Au(100), are remarkably similar and also resemble strongly the results obtained for the CoOEP molecule on graphene if one imagines the latter to simply possess more resolved peaks and a better signal-to-noise ratio than the former. Differences are not to be ignored, however. The main peak under grazing incidence, at around 778 eV, has a higher relative intensity in the case of the graphene sample. The main peak of the normal incidence spectra (~ 780 eV), on the other hand, has the higher relative intensity in the gold substrates, when this peak is compared to the secondary peak (~ 781 eV). This peak is not well resolved in the gold measurements, and appears as a shoulder of the main peak, while it is close in intensity to the main one in the case of the graphene substrate. Nevertheless, the similarities in the electronic structure of the cobalt atom that can be inferred from these spectra indicate that, just

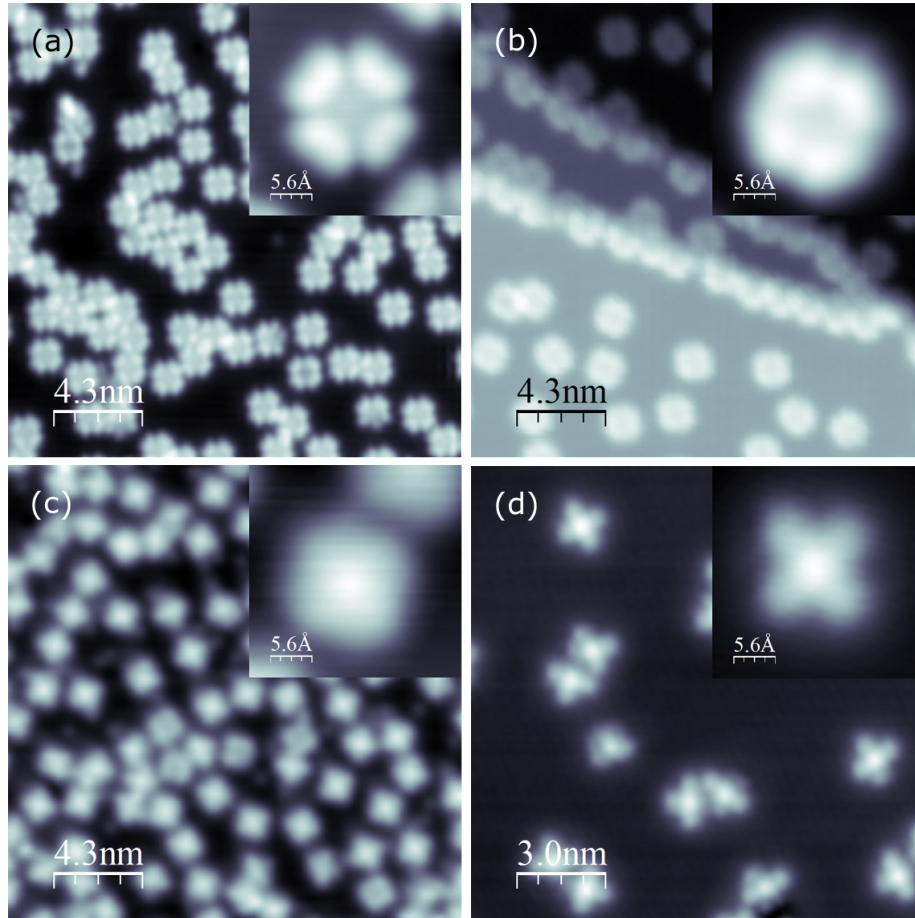


Figure 3.19: STM images of the CoOEP molecules deposited on Cu(100) ((a); Main image: $U = 500$ mV, $I = 100$ pA; Inset: $U = 50$ mV, $I = 200$ pA; $T = 1.1$ K) and Cu(111) ((b), Main image and inset: $U = 1$ V, $I = 100$ pA, $T = 4.5$ K), and CoTBP molecules on Cu(100) ((c); Main image: $U = -50$ mV, $I = 100$ pA; Inset: $U = 50$ mV, $I = 100$ pA; $T = 1.1$ K) and Cu(111) ((d); Main image: $U = -1$ V, $I = 32$ pA; Inset: $U = -700$ mV, $I = 26$ pA; $T = 4.5$ K).

as was the case for the CoOEP molecules on graphene, the ones deposited on gold appear to have only a limited or weak interaction with the substrate, in the end possessing an electronic configuration that should be akin to the one of the free molecule. Interestingly, the similarities of the electronic configuration of the CoOEP molecules on graphene and gold do not translate into comparable magnetic properties. While the cobalt ion possesses significant magnetic moment that is even coupled to the ferromagnetic nickel substrate below the graphene in the first case, there is no magnetic moment detectable from the XMCD

measurements of the molecules deposited directly on gold.

The main difference between the two spectra taken on gold is a slight shift of all the peaks to higher energies on the Au(100) substrate. For the copper substrates, however, there are very clear differences in the spectra recorded on the differently oriented surfaces. The peak at 778.1 eV, already significantly reduced on Cu(100) when compared to the spectra on gold, completely disappears on Cu(111). The main peak shifts to higher energies as well as the shoulder peak at around 780 eV, which displays a stronger shift than the former, becoming more evident. Another significant difference between the two copper substrates measurements is in the L_2 edges. This edge is a lot more angle-dependent on the Cu(111) spectra, pointing to a lower charge occupation, especially for in-plane orbitals, of the CoOEP molecules on this substrate. The analysis of the integrated intensity of the X-ray absorption on these two substrates paints a very clear picture of what is different between the two systems. While the integrated intensity is similar for the magic incidence geometry, pointing to a comparable overall occupation between the systems, the intensities for the grazing and normal incidences differ significantly. The grazing incidence intensity is reduced by 18% in the Cu(111) sample compared to the Cu(100), while for normal incidence there is an 18% increase. This makes for a much larger charge anisotropy for the cobalt ions of the molecules deposited on Cu(111). This can be directly inferred to be caused by a reorganization of the electronic structure of the ion, with electrons going from the in-plane orbitals of the ion in the Cu(100) system to the out-of-plane orbitals of the ones in the Cu(111). A likely scenario is that the orbitals, represented in Fig. 3.20 mainly by the peaks at around 778.2 eV and 779.3 eV for out-of-plane and in-plane orbitals, respectively, were partially occupied on Cu(100). On Cu(111) an out-of-plane orbital, likely d_{z^2} , became fully occupied and an in-plane orbital was emptied. This would cause the 778.2 eV peak to completely disappear from the spectra of the Cu(111) system, while an increase is noticeable for the 779.3 eV peak and the L_2 edge. Such changes would also have a drastic effect in the magnetic properties of the molecules, as discussed in the following.

As seen in Fig. 3.21, the XMCD spectra recorded for the CoOEP molecule on the Cu(100) substrate displays a significant signal in all incidence angles measured. The XMCD signal of the molecules on Cu(111), on the other hand, is null for all incidence angles, illustrating the complete quench of the magnetic spin moment of the molecules on this surface. The variations observed in differently oriented surfaces illustrate how important the role of the substrate is in the magnetic properties of these molecules. The stronger XMCD signal is obtained

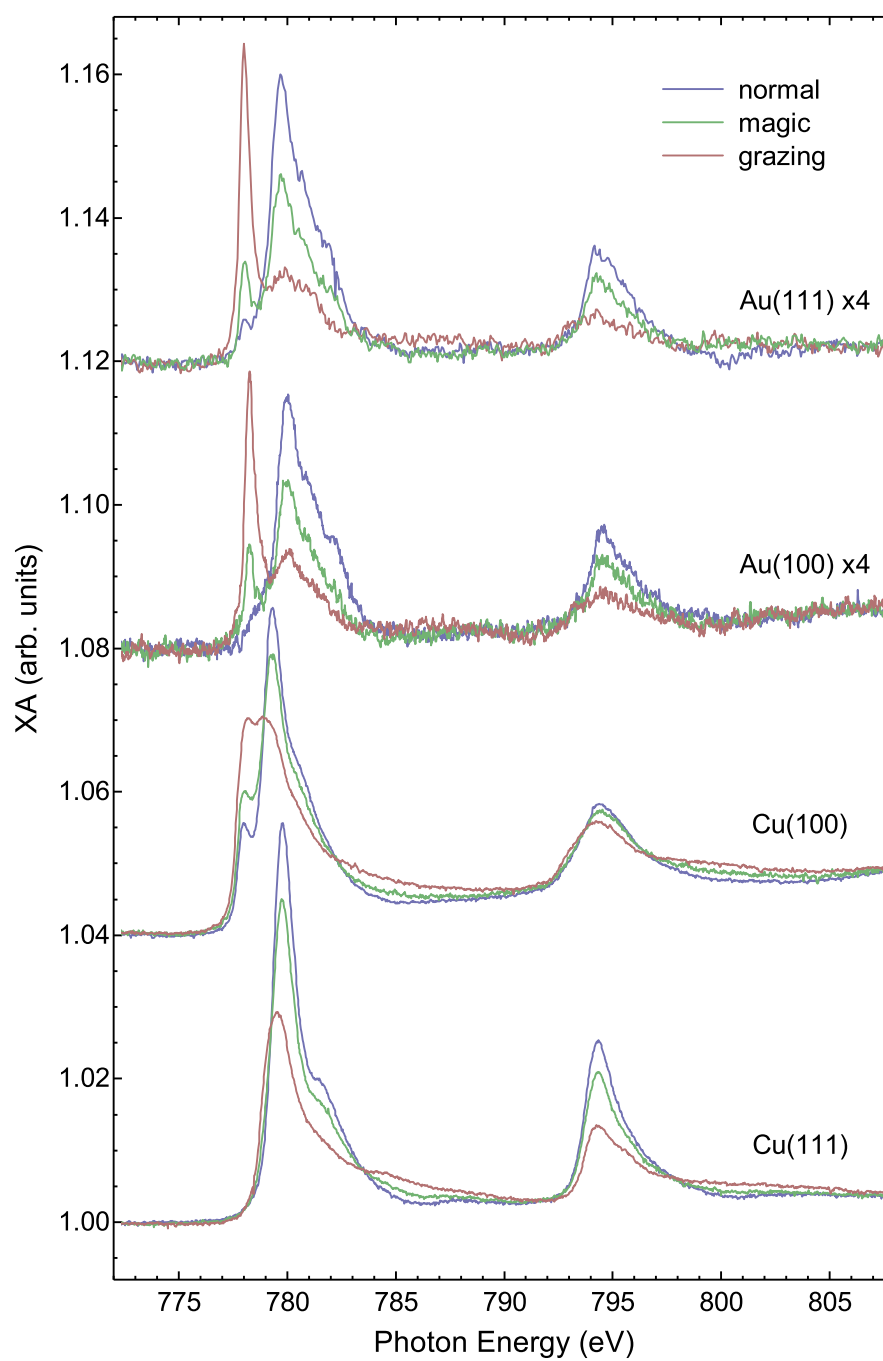


Figure 3.20: Angle-dependent XAS of the cobalt L edge for CoOEP on different metallic substrates, taken at 4.5 K. Several spectra were vertically shifted and the gold substrate spectra were multiplied by four for clarity.

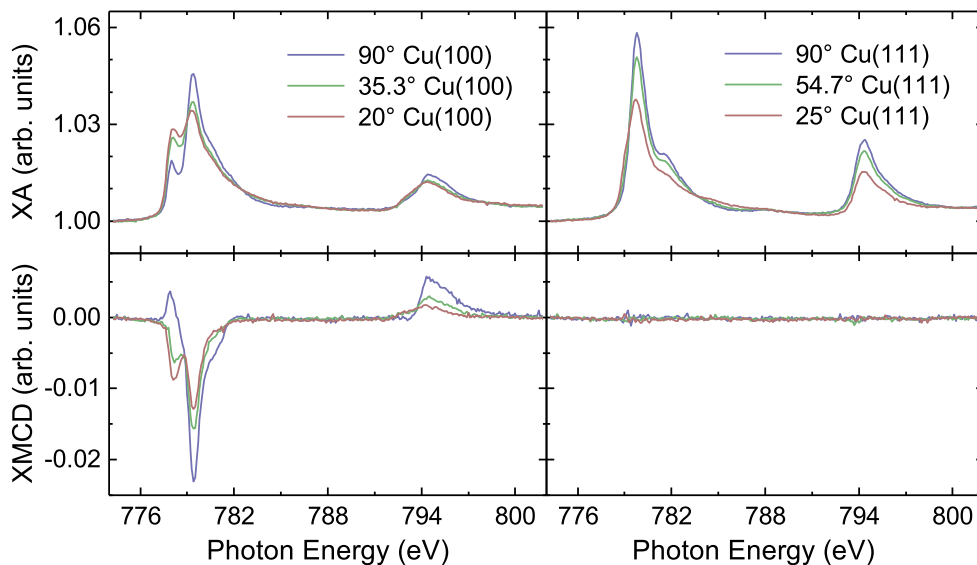


Figure 3.21: XAS and XMCD angle dependence for the CoOEP molecule deposited on differently oriented copper substrates, taken at 4.5 K and 6 T.

under normal incidence, displaying the predominance of the in-plane orbitals in the magnetic moment of the molecule, but the out-of-plane orbitals also contribute, as evidenced by the negative contribution to the L_3 edge XMCD at 777.9 eV, a behavior characteristic to the d_{z^2} orbital, under normal incidence. The fact that the corresponding peak disappears from the XAS spectra for the molecules deposited on Cu(111) is a strong indication that in this system the d_{z^2} is completely filled. This is likely caused by an enhancement of the ligand-field splitting of the energy levels of the cobalt ion of the molecules deposited on Cu(111). The differences observed on the two substrates can then be attributed to conformational changes to the ligand structure of the molecules, not to different interactions of the substrates to the metal centers. That is not to say there is a weak interaction between the substrate and molecule. The case may be that the interaction is present, but similar in both systems. It was demonstrated [71] that the orientation of the substrate may allow for the opening of an indirect charge transfer path between porphyrin molecules and the substrate by the shift of the substrate's energy level alignment with those of the molecule. In the present work the charge transfer from the cobalt center is likely occurring for the molecules deposited on the two differently oriented substrates as will be seen later when the oxidation states are discussed. Additionally, the total electron density remains largely unchanged for the central ion. Additional charge transfer channels to

other parts of the molecule could help explain the differences observed between the two CoOEP samples, however.

Table 3.3: Sum-rule results for CoOEP on Cu(100)

α	$m_L(\alpha)/n_h\mu_B$	$m_S^{\text{eff}}(\alpha)/n_h\mu_B$
90°	0.051 ± 0.001	0.53 ± 0.01
35.3°	0.098 ± 0.003	0.40 ± 0.01
20°	0.122 ± 0.004	0.333 ± 0.008

The sum-rule analysis of the circularly polarized X-rays results obtained for the CoOEP on Cu(100) gives further insight into the magnetic properties of the cobalt metal center. In Table 3.3 the values obtained from the sum-rule analysis are displayed. To obtain the actual magnetic moment values, the ones in Table 3.3 must be multiplied by the number of holes n_h in the valence shell of the cobalt ion. Additionally, as discussed in Chapter 1, $m_S^{\text{eff}}(\alpha) = m_S(\alpha)$ only for the measurements taken at the magic angle, because then the magnetic dipole operator contribution (T_z) cancels out. It is important to notice that even then, the values obtained here will still be lower than the real magnetic moment values, because the system measured is not in magnetic saturation. The expected values for the magnetic moment given the temperature and external field for paramagnetic systems not in magnetic saturation can be obtained from the modeling of the magnetization for an isotropic system with the Brillouin function. In this model we have the magnetization given by [72]:

$$M = ngJ\mu_B B_J(\alpha), \quad (3.2)$$

$$\text{where } B_J(\alpha) = \frac{2J+1}{2J} \coth\left(\frac{2J+1}{2J}\alpha\right) - \frac{1}{2J} \coth\left(\frac{1}{2J}\alpha\right),$$

$$\text{and } \alpha = \frac{B\mu_z}{k_B T}.$$

Here n is the number of cobalt ions per volume, J is the total angular momentum, μ_B is the Bohr magneton and k_B the Boltzmann constant. The factor g is called the spectroscopic splitting factor, or g factor for short, and is given by the Landé equation:

$$g = 1 + \frac{J(J+1) + S(S+1) - L(L+1)}{2J(J+1)}. \quad (3.3)$$

The term μ_z is the maximum value of the magnetic moment component in the direction of the external field B , and is given by $\mu_z = gJ\mu_B$. With high magnetic field and low temperatures, the paramagnet magnetization can be saturated and we have:

$$M_o = ngJ\mu_B = n\mu_z. \quad (3.4)$$

Analogously to eqn. 3.4, one can define the unsaturated magnetic moment in the direction of the external field using eqn. 3.2 as:

$$M = nm_z, \quad (3.5)$$

$$m_z = gJ\mu_B B_J(\alpha).$$

From eqn. 3.5, one can easily obtain a first approximation of the values of m_z for an external field of 6 T and temperature of 4.5 K, the conditions in which the measurements were made. If one compares to the magic-angle results from the sum-rule analysis, the only value that is within the error of our measurement is the one corresponding to $S = 1$, and $n_h = 4$. This result points to an oxidation state of +3, unlike the +2 encountered in the free molecule, evidencing a charge transfer from the Co ion. It is not surprising, considering how reactive the copper substrate is, that it would result in a strong interaction with the molecule, causing charge transfer. From the results discussed earlier for the integrated intensity of the cobalt edges, it is inferred that this is also the oxidation state of the cobalt ion of the molecule deposited on Cu(111). The oxidation state of +3 allows for the spin moment of the ion to be readily quenched by an increase of the ligand field energy.

The spin Hamiltonian formalism is used here once again to perform the calculated fit to the experimental values of the magnetization obtained from

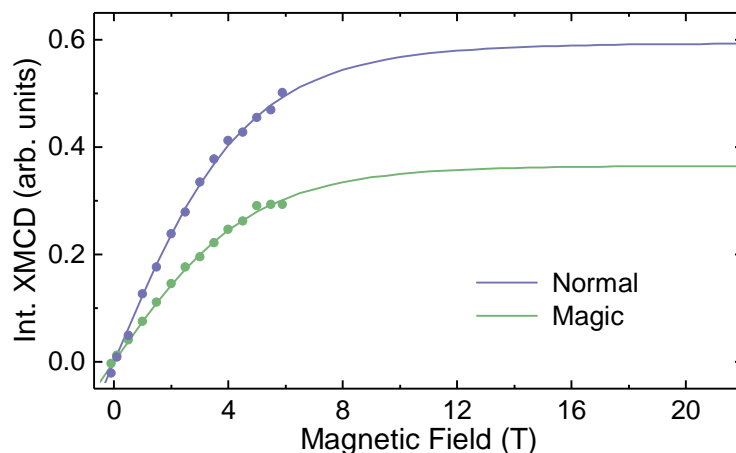


Figure 3.22: Magnetization curves for CoOEP on Cu(100) under normal and magic angles of X-ray incidence. The experimental results are shown as dots, while the solid lines are the calculated fits obtained from the spin Hamiltonian. Taken at $T = 4.5$ K.

the XMCD. Fig. 3.22 shows the experimental values as dots and fitted curves for normal and circular magic angles, assuming a spin $S=1$. It is clear, as was from the XMCD in Fig. 3.21, that the in-plane orbitals are responsible for the majority of the magnetic signal, but the curvature and relative saturation is the same for both angles which indicates low magnetic anisotropy. Indeed, the value obtained for the magnetic anisotropy from the fitting procedure confirms this, with a very low value $D = -0.04 \pm 0.02$. The difference between the two angles of incidence is accounted for mostly by the magnetic dipole operator, which is included in the Zeeman interaction term, and represents spin density anisotropy [73].

The ring-closure reaction was carried out in the usual way, but only for the molecules deposited on copper substrates. The modifications on the nitrogen edge can be verified in Fig. 3.23. The ring closure is once again clear from the spectra for both Cu(100) and Cu(111) samples. Interestingly, the integrated intensity of the nitrogen edge signal for the magic angle of the OEP molecules deposited on differently oriented substrates show great discrepancy (24%), while the TBP molecules' vary only slightly (6%). This is an indication that the charge distribution of the nitrogen atoms, and consequently the cobalt ion close environment, is very similar for the two TBP molecules. This similarity is evidenced more clearly in the cobalt edge measurements taken for the TBP molecules on both substrates, Fig. 3.24. It is clear from this picture that the central ions of the CoTBP molecules have very similar electronic configuration,

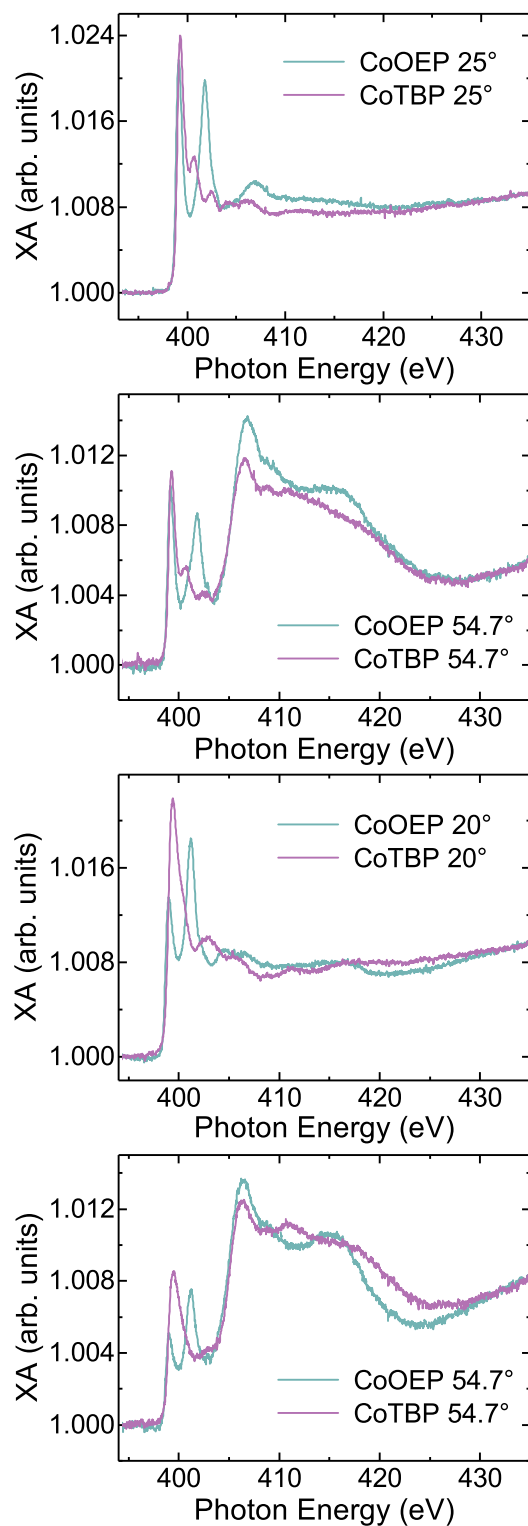


Figure 3.23: Nitrogen K edge XAS for grazing and magic incidence angles of the X-rays on Cu(111) (top) and Cu(100) (bottom) before and after annealing the molecules. Taken at room temperature.

especially when compared to the OEP molecules. While there is no discernible change between the cobalt edge spectra of the molecules on Cu(111) before and after ring closure, the spectra of the Cu(100) molecules is drastically changed, mainly by the disappearance of the lower energy peak, attributed mainly to the d_{z^2} orbital. In fact, the differences between the spectra before and after ring closure on Cu(100) can be explained in the same way the differences between the CoOEP molecules on Cu(100) and Cu(111) were explained before. The similarities of the two TBP molecules and the OEP molecule on Cu(111) would suggest that, just as it was in that case, the magnetic moment of the CoTBP molecules on both substrates are quenched, and this is indeed observed.

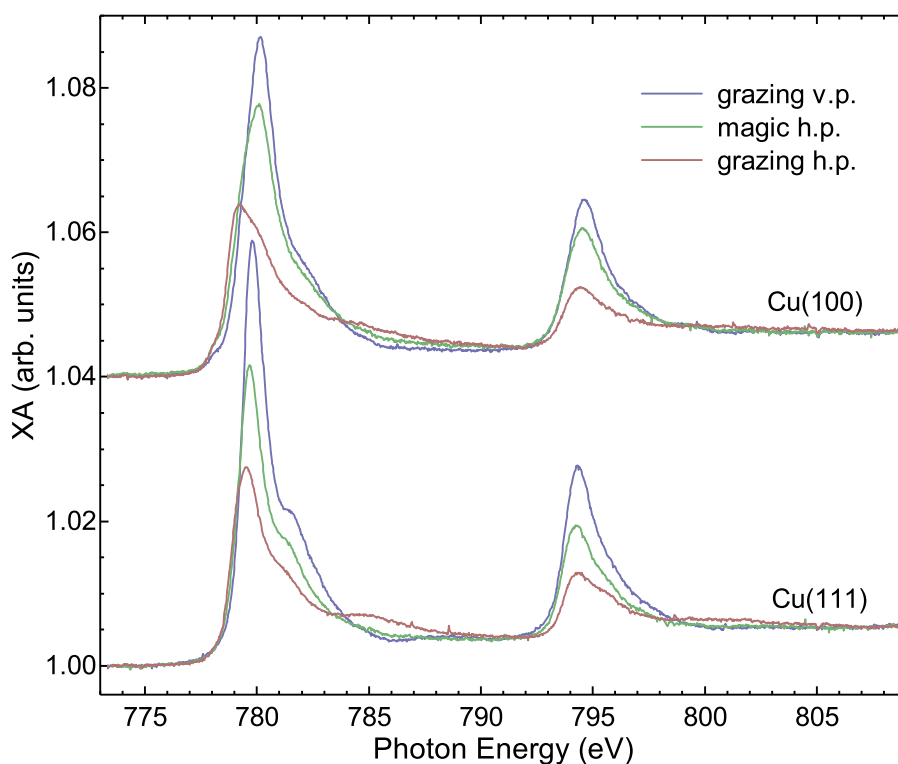


Figure 3.24: Angle-dependent XAS of the cobalt L edge for CoTBP on Cu(100) and Cu(111), taken at 4.5 K. Cu(100) spectra were vertically shifted for clarity.

Fig. 3.25 shows the XA and XMCD spectra of the CoTBP molecules for different angles on Cu(100) and Cu(111). The magnetic moments of the two systems are quenched on every incidence angle measured. In light of all the results presented here, it seems that the most likely scenario for both the TBP molecules' metal center electronic configuration is that three of the five orbitals

of the cobalt ions are completely filled while the remaining two are empty, in a $3d^6$ configuration that corresponds to an oxidation state of +3 for the cobalt ion, analogous to the OEP molecules.

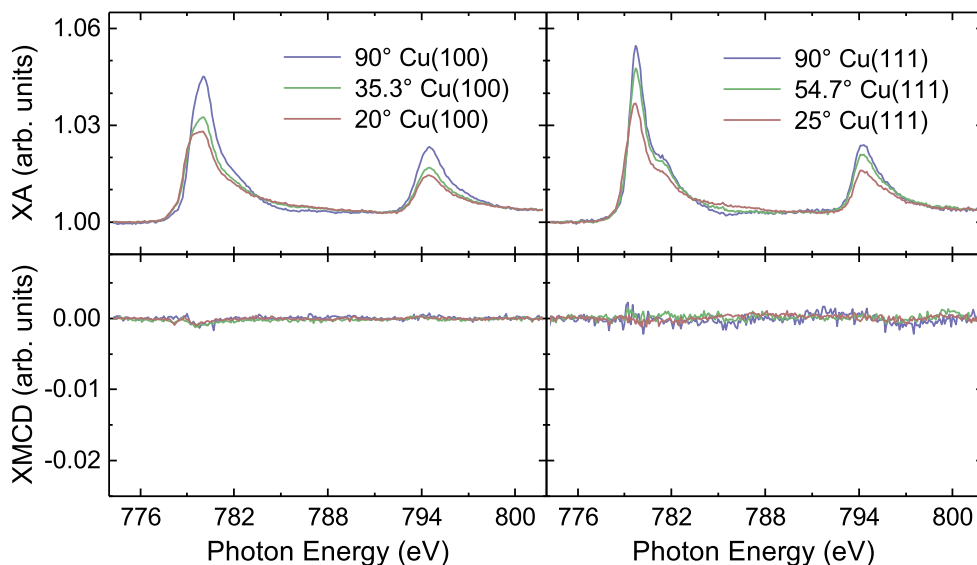


Figure 3.25: XAS and XMCD angle dependence for the CoTBP molecule on differently oriented copper substrates, taken at $T = 4.5$ K.

The interaction of CoOEP/TBP molecules with copper substrates is seen in this subsection to be much stronger than their interaction with gold or graphene capped substrates, the spectral shape of which resemble much more that of the bulk sample [58], which points to them retaining the oxidation state of the free molecule. This interaction is very strong and unaffected by the ring-closure reaction, all the significant changes brought by it being the result of ligand field variations.

If one assumes the CoOEP molecule being in a square pyramidal geometry when deposited on Cu(100), one would expect the energy level distribution displayed on the left side of Fig. 3.26. From our results for the spin moment and the number of electrons, the distribution would be as shown, with a ligand field too weak to keep the two higher energy electrons on the same orbital, thus resulting in the observed $S = 1$. After ring closure, we propose an inversion of the mid-energy orbitals positions, shown on the right side of Fig. 3.26. This distribution corresponds to a square planar geometry in which the ligand field splitting is stronger and forces the electrons to fully occupy the d_{z^2} orbital, while leaving the d_{xy} completely empty. This reorganization causes the complete quench of the magnetic moment of the new molecule, because there are no longer

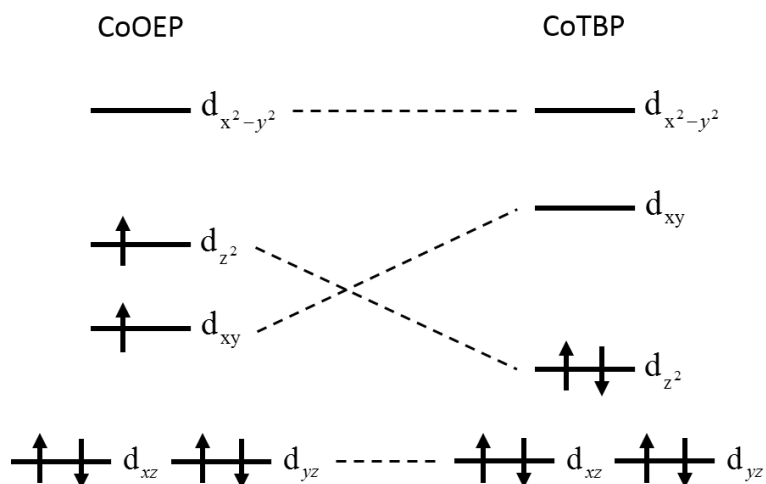


Figure 3.26: Proposed energy level arrangement of the molecules before (CoOEP) and after (CoTBP) ring closure on Cu(100). The energy levels of the CoOEP/TBP molecules on Cu(111) are proposed to be the same as the ones of CoTBP on Cu(100).

any partly occupied orbitals.

Based on DFT calculations, it was suggested that the most stable adsorption structure of the CoOEP molecules on Au(111) [74] and graphite [75] is the one in which the ethyl groups are pointing up, away from the substrate. From our results, we believe this structure is also occurring on Cu(100) at lower temperatures. At room temperature, we expect the same situation as observed for the FeOEP molecules on Au(111), when the ethyl groups may rotate and form a more flat structure reminiscent of the TBP macrocycle. In the case of Cu(111), the flat macrocycle structure appears to be present even for lower temperatures, as concluded from the similarities between the OEP and TBP low-temperature spectra on this substrate.

4

LANTHANIDE MAGNETIC MOLECULES

4.1 Introduction

The lanthanides, often called "inner transition metals", are another important series of elements in molecular magnetism. They possess many properties similar to the previously discussed d-block transition metals, such as metallic and often magnetic behavior but, unlike those, the lanthanides' valence electrons are located in the $4f$ electron shell. This electronic configuration of lanthanide ions allows them to achieve higher magnetic moments, while simultaneously shielding the valence electrons from stronger interactions with molecular ligands [76]. For this reason, even though the influence of the ligand field is still usually noticeable and potentially crucial in the magnetic properties of lanthanide magnetic compounds, they primarily have a strong metallic character, with little environment-dependent variation observable in their x-ray absorption spectra.

The lanthanide series together with the elements scandium and yttrium are usually collectively known as the rare-earth elements. This name often leads to the misinterpretation that these elements are scarcely found in nature, but that is not accurate. The main difficulty with their procurement is that they are often found in clusters of various rare-earth elements and other minerals, and their individual extraction is a complicated and often dangerous process, given the high toxicity involved in their mining and processing. Extraction difficulties notwithstanding, these elements' importance in modern technology has grown considerably in recent years, particularly in the development of efficient permanent magnets and components in renewable energy production, where

their use is very widespread, even though frequently only small amounts are necessary in each instance, specially when compared to the more traditionally used metals such as copper and iron.

The application of lanthanide ions as metallic centers of magnetic molecules was initially spurned in favor of transition metals, given the latter's versatility and potential for unusual magnetic properties, but in recent years lanthanides' use has increased as the unique properties of these metals are discovered. The shielding of the $4f$ electrons results in a dominance of the +3 oxidation state across the different elements in the series [76]. This is reflected in the difficulty to separate them from their naturally occurring clusters, and in the apparent lack of variety in their magnetic properties. Once again setting themselves apart from the transition metals, however, the magnetic molecules with lanthanide centers display a non-quenched orbital moment and a high spin-orbit interaction that cannot be ignored in the treatment of these molecules. The spin-orbit coupling of lanthanide $4f$ electrons is about 0.2 eV, as opposed to around 0.05 eV in the $3d$ transition metals [77]. This gives rise to magnetic properties that are highly dependent on the orbital characteristics of the valence electrons, and consequently closely related to the molecular symmetry. The increased attention directed towards lanthanide magnetic molecules is also a direct consequence of the growing realization that single-ion anisotropy is a crucial property in the design of single-molecule magnets (a class of ferromagnetic molecules whose hysteresis displays slow magnetic relaxation) with large anisotropy barriers, a fundamental characteristic in these compounds, and lanthanide ions have notoriously high single-ion anisotropies [78]. The interest in these molecules has only increased in recent years and the lanthanide centered variants are very promising candidates for high-spin, high-anisotropy-barrier single-molecule magnets (SMM).

The two complexes discussed in this chapter belong to the class of molecules lanthanide-tris(tetramethylheptanedionate) (LN-(TMHD)₃). The two molecules, Dy(TMHD)₃ (shown in Fig. 4.1) and Er(TMHD)₃ were synthesized by Prof. Constantin Czekelius in Heinrich Heine Universität Düsseldorf. Both were in powder form, with the molecule containing dysprosium displaying a white colored powder and the one with erbium being pink. The sample preparation is very similar to the one of the porphyrin compounds discussed previously, with the distinction that the (TMHD)₃ molecules sublime at much lower temperatures. This warranted greater attention during the degasing of the molecules, as temperatures slightly above room temperature already initiates the sample sublimation. The Dy(TMHD)₃ was sublimated at around 370 K and the Er(TMHD)₃ at around 360 K. This low sublimation temperature also indicates

a higher risk of desorption from the substrate after deposition, but no significant decrease in signal over time was observed and once the low temperatures of the measurements are reached, this ceases to be an important factor. Spatially, however, the molecular coverage was highly inhomogeneous in most substrates, which could point to an extremely high mobility and cluster-forming behavior of the molecules after deposition. This would in turn point to a weak interaction with the substrate, which is a common trait of lanthanide compounds. As will be discussed in the following, however, significant changes to the magnetic properties are still observed among different substrates. The coverage for the samples presented on this section was around 0.5 ML.

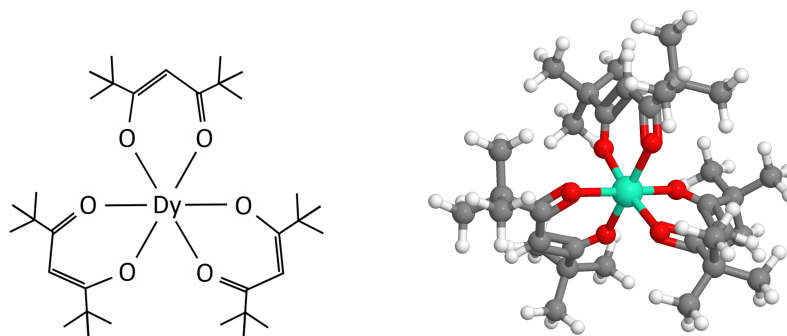


Figure 4.1: Schematic representation of $(\text{TMHD})_3$ molecule with Dy as the lanthanide metallic center (left) and its 3-dimensional representation (right).

XAS measurements of molecules deposited on HOPG in particular displayed significant molecule density inhomogeneity across its surface, with measurements performed in different positions displaying similar line shapes but varying intensities. Since the changing of the measurement angle is never free of a change in the position of the beam on the sample, this leads to an uncertainty in the direct comparison of the intensity between different angles in this substrate. This inhomogeneity may have various causes. The substrate might be itself inhomogeneous, for instance, due to possible imperfections in the cleaving procedure. In the graphene samples similar surface inhomogeneity could be a result of varying tensions generated across the graphene during the CVD growth, resulting in wrinkles across the surface. Another possibility is that the combination of a high degree of attraction between the molecules coupled with a superb mobility on the HOPG substrate in particular. In the figures presented of the measurements performed on the HOPG substrate, the intensity of the grazing incidence linear

polarization spectra and normal incidence circular polarization spectra has been scaled by about 5% to match the expected intensities of these geometries based on the two other incidence angles' results. As a consequence, detailed analysis of the charge densities based on the signal intensity differences among varying incidence angles is not meaningful for these molecules.

The geometry of these molecules in gas form is displayed on the right side of Fig. 4.1, with the schematic representation pictured on the left side. Following deposition this configuration is unlikely to remain unaltered, particularly if there is a stronger than usual interaction between lanthanide and substrate. STM-supported studies [79] have demonstrated that similarly shaped molecules adapt to a distorted shape when deposited on a Au(111) substrate, with two ligands adsorbing with their rings parallel to the substrate, while the third one rests on a plane perpendicular to it on top. This configuration would promote the strongest lanthanide/substrate interaction, as well as providing a significant alteration to the free molecules' symmetry, consequently causing interesting changes to the lanthanide's electronic configuration.

4.2 Dy(TMHD)₃

The aforementioned metallic character of the lanthanide ions dominates the spectral shape of the M_{4,5} edges across the three different substrates, as displayed in Fig. 4.2. There is no significant difference in the overall structure, with the three-peak motif of the M₅ edge present on the three instances. This line shape agrees very well with multiplet calculations for the isolated Dy⁺³ ion [80], reinforcing the expectation that we have the common oxidation state on the Dy(TMHD)₃ molecules on the three different substrates. The three-peak structure of the M₅ edge that is present in every substrate is common for trivalent late lanthanides, and is a result of the splitting of the energy of the unoccupied 4f states allowed by the optical selection rules $\Delta J = 0, \pm 1$ [80]. There is, however, some noticeable difference in the degree of angle dependence observed. The angle dependence of the graphene/Ir(111) sample is the strongest among the three substrates. The second peak intensity increases substantially on this substrate for the grazing angle of incidence, indicating a preferential adsorption geometry on this graphene substrate, and likely a higher degree of ion-substrate interaction. The spectra of the molecules deposited on graphene/Ni/W(110), on the other hand, show only subtle differences between the various angles of incidence. The idea that on the two substrates with the lower angle dependence there is a weakened interaction with the substrate is reinforced by the fact that on these

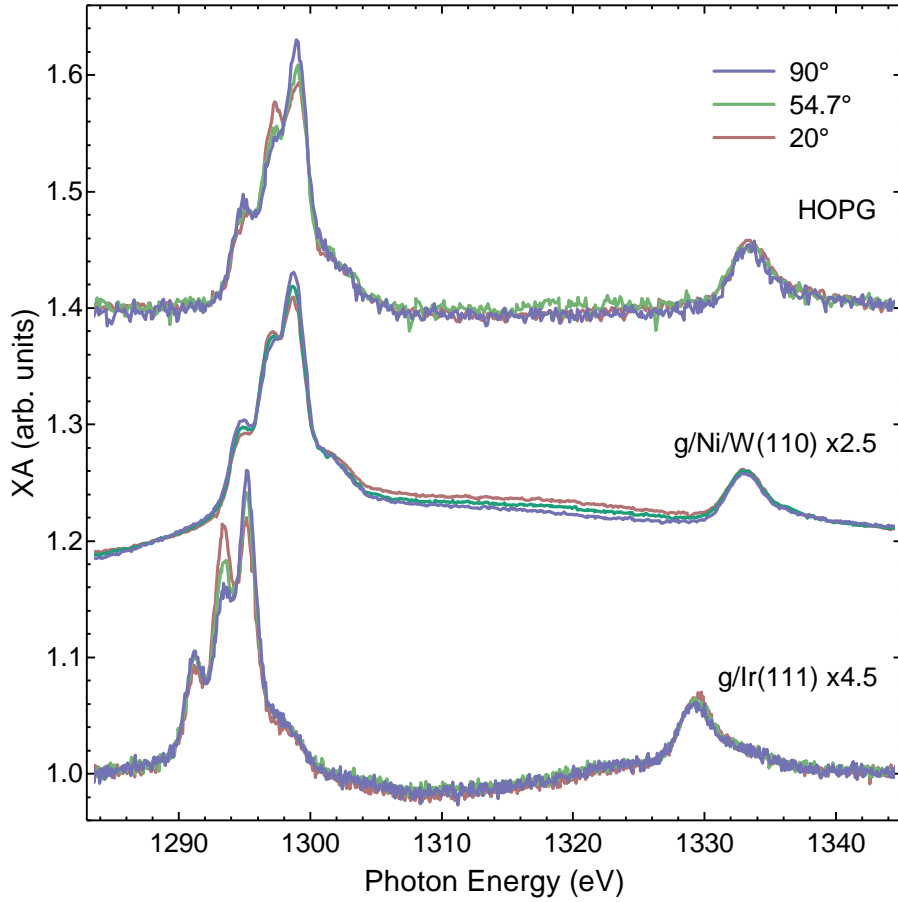


Figure 4.2: XA spectra of the Dy $M_{4,5}$ edges of $Dy(TMHD)_3$ molecules on three different substrates for three angles of incidence of the linearly polarized x-rays. The temperature was 2.4 K for the graphene/Ir(111) substrate, and 7.8 K for the other substrates. The spectra were vertically displaced and stretched when necessary for clarity.

substrates the inhomogeneity of the molecular coverage was more significant. Moreover, on the graphene/Ir(111) substrate there is a significant energy shift in the position of the $M_{4,5}$ edges, usually a strong indication of changes to the ion's oxidation state [81]. The line shape remains largely unchanged when compared to the other substrates and the free ion multiplet calculations, however, suggesting a lower degree of substrate interaction such as substrate/Dy orbitals hybridization, rather than outright charge transfer and ionic reduction. While this experiment was performed on a different beamtime, and it's not unthinkable that this energy shift would be caused by different experimental conditions or equipment calibration, an energy shift of this magnitude (around 4 eV) has not

been observed between other samples studied on the same beamtimes, where a maximum shift in energy of 2 eV was observed. It has been reported [82], for single lanthanide atoms deposited directly on graphene/Ir(111), that the Dy ions adopt the same oxidation state as other lanthanides deposited on that substrate, apart from Tb, among the studied elements. In those experiments, the Dy ion was found to be on a divalent state and was the only lanthanide to show magnetic hysteresis and remanence at 2.5 K. The isolated ion deposition allows for a much stronger substrate and local field interactions, however, and the properties observed in those systems are not likely to be the same as in the Dy(TMHD)₃ molecules.

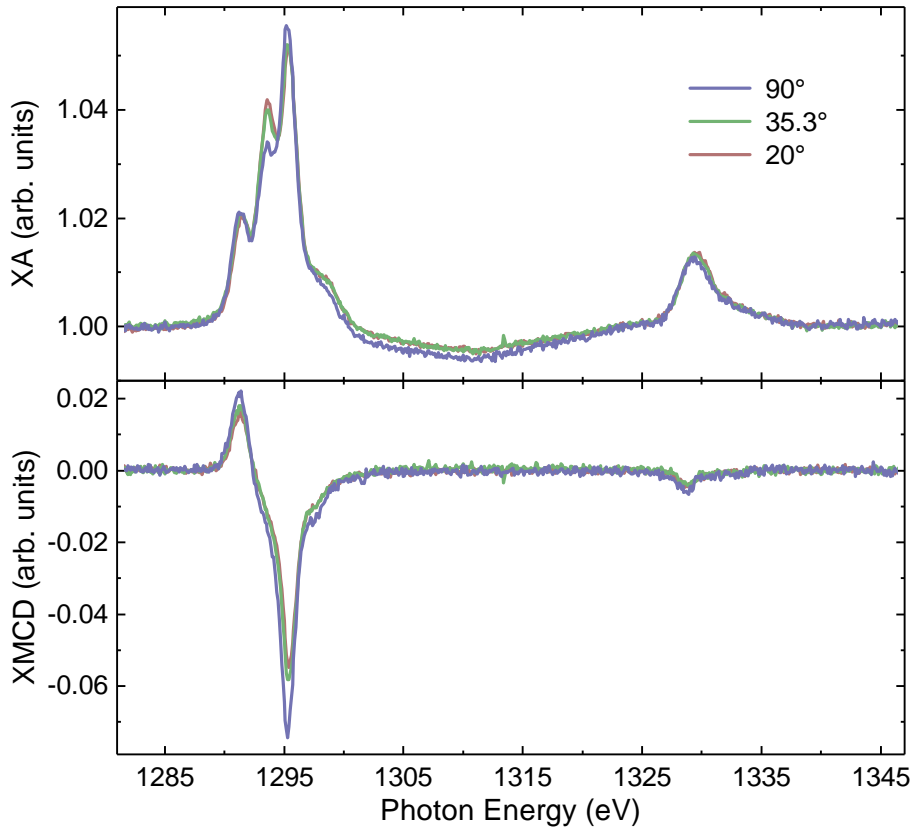


Figure 4.3: XA and XMCD spectra of the Dy $M_{4,5}$ edges of Dy(TMHD)₃ molecules on graphene/Ir(111) for three angles of incidence of the circularly polarized x-rays. The temperature was 2.4 K and the magnetic field was 8 T.

The circularly polarized light absorption spectra and corresponding XMCD for the Dy(TMHD)₃ molecules deposited on graphene/Ir(111) are pictured in Fig. 4.3. A substantial dichroic signal is obtained under all angles of incidence measured,

Table 4.1: Moments obtained from the sum rules for Dy(TMHD)₃ on graphene/Ir(111) at 2.4 K and 8 T.

α	$m_L(\alpha)/\mu_B$	$m_S^{\text{eff}}(\alpha)/\mu_B$
90°	5.5 ± 0.9	4.3 ± 0.9
35.3°	3.6 ± 0.5	2.7 ± 0.6
20°	3.7 ± 0.8	3.0 ± 0.7

with the normal incidence measurement displaying the largest difference. This indicates that the easy direction of magnetization on this system points out of the plane of the substrate, since the magnetic field is aligned with the x-rays in every measurement.

The different angle dependence between the white line of the circularly polarized light and the linearly p-polarized spectra are due to the characteristics of the different types of light polarization. While the normal incidence measurements, either for circular or linear polarization, preferentially probe the orbitals parallel to the plane of the substrate, in the case of the grazing incidence measurements this is not so straightforward. The grazing incidence geometry of linearly polarized light preferentially probes the orbitals that are aligned out of the plane of the substrate, but for the circularly polarized light, this geometry also probes the in-plane orbitals significantly [37]. This results in a relative reduction in the intensity of the peaks mainly associated with out-of-plane orbitals when using circularly polarized light, causing the different line shapes observed in the two grazing-incidence measurements. The very small XMCD signal of the M₄ edge illustrates how significant the orbital moment contribution is to the total magnetic moment of these compounds, and how one should be careful to not simply ignore the orbital moment when modeling the magnetization obtained experimentally, as is usually done for the transition metal complexes.

The small M₄ edge XMCD signal, M_{4,5} edge mixing, and significant substrate-dependent bending of the spectra result in large errors in the sum-rule analysis of the circularly polarized results. They are still valuable in the determination of the magnetic moments of the lanthanide molecules, given the smaller dependence of the spin magnetic moment on the T_z term and the overall greater significance of the orbital magnetic moment of lanthanides when compared to transition metal complexes. The results of the sum rules for the Dy(TMHD)₃ molecules deposited on graphene/Ir(111) are displayed on Table 4.1. For these the Dy(III) state was used, with 9 electrons in the 4f orbitals.

For the magic angle of 35.3°, when the contribution of every orbital to the

total intensity is the same and the magnetic dipole contribution to the spin moment goes to 0, the total moment obtained for the sum-rules is $m_T = 6.3 \mu_B$. This value, as usual, is lower than the theoretical value for Dy(III), when one expects to find $m_T = 10 \mu_B$, and the difference is mainly due to the unsaturated moment measured at 8 T, but also to the large error in the sum-rule calculation described above. A value closer to the theoretical one is obtained later, when the extrapolation to the saturated values is obtained from the parameters of the magnetization curve fitting. Aside from this discrepancy, the sum rules reveal the expected predominance of the orbital moment, on average 30% larger than the spin moment.

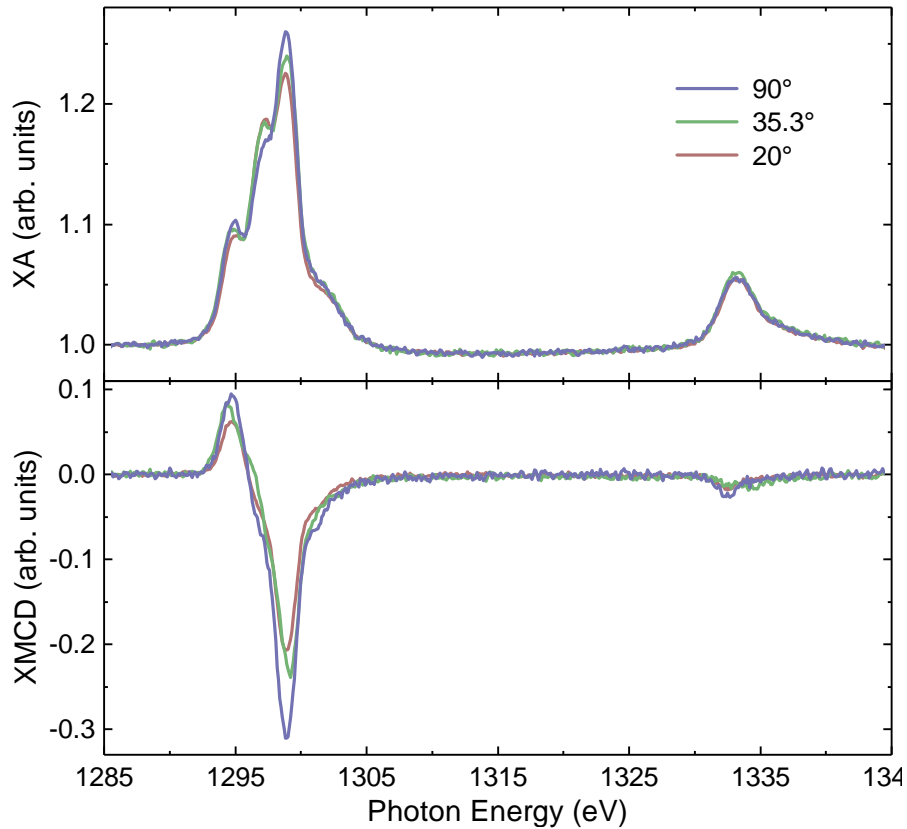


Figure 4.4: XA and XMCD spectra of the Dy $M_{4,5}$ edges of $\text{Dy}(\text{TMHD})_3$ molecules on HOPG for three angles of incidence of the circularly polarized x-rays. The temperature was 7.8 K and the magnetic field was 8 T.

No significant change to the XMCD spectra is observed for the molecules deposited on HOPG when compared to the previous substrate, as seen in Fig. 4.4. This will be the case for the third substrate too, as is expected from the small

Table 4.2: Moments obtained from the sum rules for Dy(TMHD)₃ on HOPG at 7.8 K and 8 T.

α	$m_L(\alpha)/\mu_B$	$m_S^{\text{eff}}(\alpha)/\mu_B$
90°	3.4 ± 0.3	2.4 ± 0.2
35.3°	2.6 ± 0.1	1.8 ± 0.2
20°	2.6 ± 0.1	1.6 ± 0.1

contribution of the crystal field to the orbital occupation. The sum-rules results are presented in Table 4.2.

The values obtained are even lower than the ones of the graphene/Ir(111) substrate. This is initially surprising if one notices that the spectra of the HOPG samples have the lowest degree of bending and edge mixing among the three substrates. The large underestimation, however, is mostly due to the distance from magnetic saturation, itself mainly caused by the higher temperature on this substrate. The ratio between orbital and spin moment is the highest among the three substrates, with an orbital moment in average 50% higher than the spin moment.

The same line shape is repeated for the graphene/Ni/W(110) substrate, as verified in Fig. 4.5. The XMCD was taken at the usual 8 T and at a field close to 0 T, as shown in the figure, in order to verify whether there was a magnetic coupling of the metal ion to the ferromagnetic Ni substrate, as was observed for some of the porphyrin molecules. No XMCD was observed for lower fields, however, evidencing the lack of magnetic coupling. The ferromagnetism of the Ni substrate is confirmed in Fig. 4.6, where the circularly polarized XAS and corresponding XMCD of the Ni L_{2,3} edges for a magnetic field of 50 mT are displayed. The lack of magnetic coupling to the ferromagnetic Ni is no surprise, given the previously mentioned shielding of the 4f orbital of the dysprosium ion. This coupling would be much more likely to occur without the graphene layer, given that the higher reactivity of the Ni metal would likely promote a different adsorption structure, with the central ion possibly closer to the substrate.

The moments obtained from the sum rules for this substrate are displayed in Table 4.3. Once again the value obtained for the total magnetic moment is much lower than the one expected for a Dy(III) ion. In the following discussion of the fitting of the magnetization curves, the parameters required for the extrapolation to magnetization saturation will be obtained and a better agreement to theory will be achieved.

As explained previously, the modeling of the magnetization of these complexes

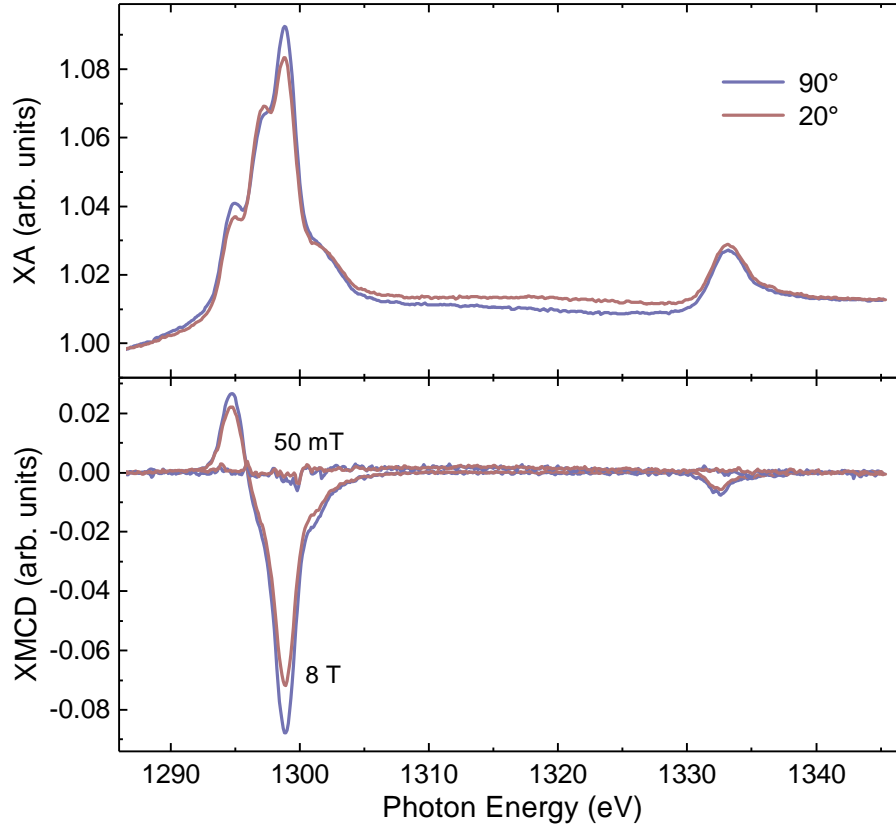


Figure 4.5: XA and XMCD spectra for the Dy $M_{4,5}$ edges of $\text{Dy}(\text{TMHD})_3$ molecules on graphene/Ni/W(110) for two angles of incidence of the circularly polarized x-rays. The temperature was 7.8 K.

Table 4.3: Moments obtained from the sum rules for $\text{Dy}(\text{TMHD})_3$ on graphene/Ni/W(110) at 7.8 K and 8 T.

α	$m_L(\alpha)/\mu_B$	$m_S^{\text{eff}}(\alpha)/\mu_B$
90°	3.6 ± 0.4	2.7 ± 0.3
35.3°	3.0 ± 0.2	2.5 ± 0.1
20°	2.7 ± 0.2	2.3 ± 0.3

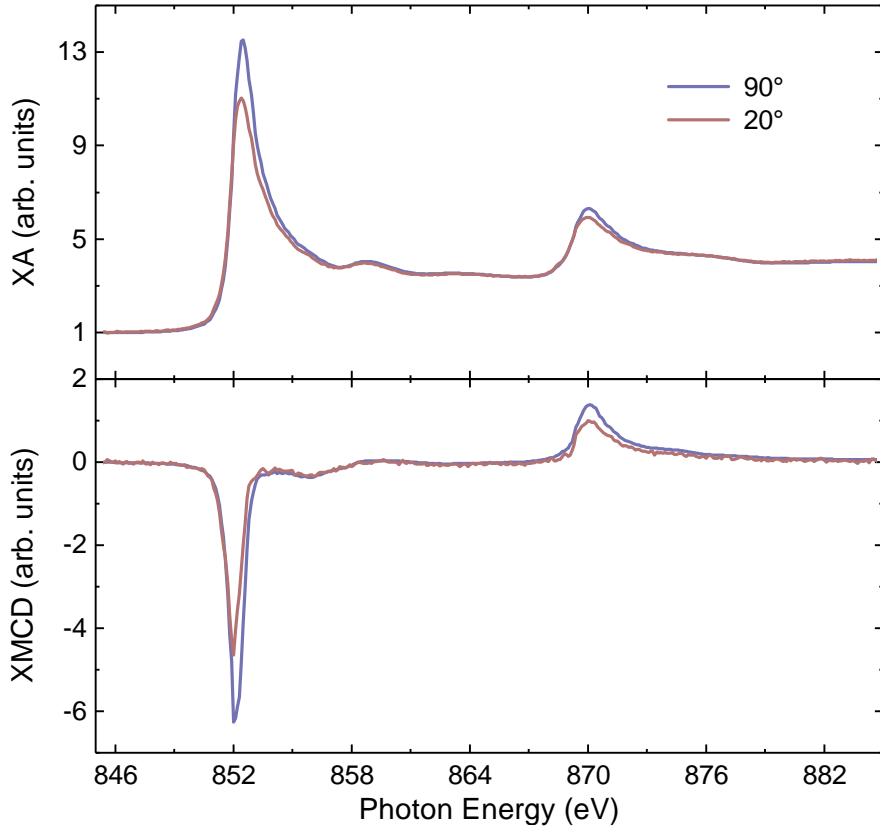


Figure 4.6: XA and XMCD spectra for the Ni $L_{2,3}$ edges of $Dy(TMHD)_3$ molecules on graphene/Ni/W(110) for two angles of incidence of the circularly polarized x-rays. The temperature was 7.8 K and the magnetic field was 50 mT.

cannot follow exactly the same procedure of the transition metal complexes of the previous chapter. Here, the orbital moment cannot be ignored and the total angular momentum J is the quantity that needs to be modeled, as opposed to S . Once again, however, we will consider the axial symmetry model of the moment and fit the z component of the magnetic moment, in the direction of the quantization axis of the 4f orbitals. The Hamiltonian for this system is

$$\mathcal{H} = \mu_B g_J \mathbf{B} \cdot \mathbf{J} + D J_z^2, \quad (4.1)$$

where only the Zeeman and the uniaxial anisotropy energy terms are considered. The first term represents the Zeeman energy: μ_B is Bohr's magneton, the Landé factor (g_J) will depend on the the lanthanide ion and its oxidation state, \mathbf{B} is the external field vector and \mathbf{J} is the total angular momentum vector.

The second term describes the uniaxial anisotropy energy: D is the zero-field-splitting parameter and J_z the total angular momentum component parallel to the quantization axis of the 4f orbitals. The T_z term is ignored, given it has a much lower value for the lanthanides than it does for the transition metals. Due to the high symmetry of this molecule, however, the orientation of the quantization axis of the 4f orbitals is not always perpendicular to the substrate. In fact, it has been verified that for similarly structured Dy molecules deposited on gold substrates, the quantization axis of the 4f orbitals is parallel to the substrate [79]. To account for this, an averaging procedure is introduced to the model in which the mean value for the magnetization on a 360° angle around the surface normal is considered, and the angle between this normal and the quantization axis is obtained as a fit parameter. Using this and the spin-Hamiltonian, we are able to model the results obtained from the XMCD measurements with good accuracy.

Fig. 4.7 shows the XMCD intensity as a function of field and the fit obtained from the model for the $\text{Dy}(\text{TMHD})_3$ molecule on the three different substrates. Since there was no direct measuring of the temperature at the sample position, with the nominal temperature values instead relying on a calibration performed beforehand that uses the temperature of a heat exchanger between the sample and the liquid helium as means of measuring the temperature in real time, the temperature was allowed to be fit as a parameter in our model, as long as the resulting fitted value was within a reasonable range of the nominal temperature obtained from the calibration. Through this procedure the obtained fitted temperatures fell within the range of ± 1 and ± 2 K of the nominal temperature, for measurements performed with and without the sample cooling shield respectively. The temperatures mentioned in the discussion of the magnetization curves are those obtained from the fitting procedure. The experiments were performed by taking the XA intensity of circularly polarized light at the energy of highest XMCD signal while sweeping the magnetic field value from 8 T in one direction to the same value and opposite orientation, then switching the polarization of the x-rays and repeating this procedure. The whole measurement was then repeated for an energy value in the pre-edge region, so that the edge value could be properly normalized. The intensities were further normalized by dividing all data points by the highest recorded value, such that in Fig. 4.7 the maximum intensity is shown as 1.

The experiment performed on the graphene/Ir(111) substrate, shown on the bottom of Fig. 4.7, was the only one in which the magic angle for circular polarization was also taken. Additionally, this measurement was the only one performed under temperatures in the range of 2.4 K, due to the availability of

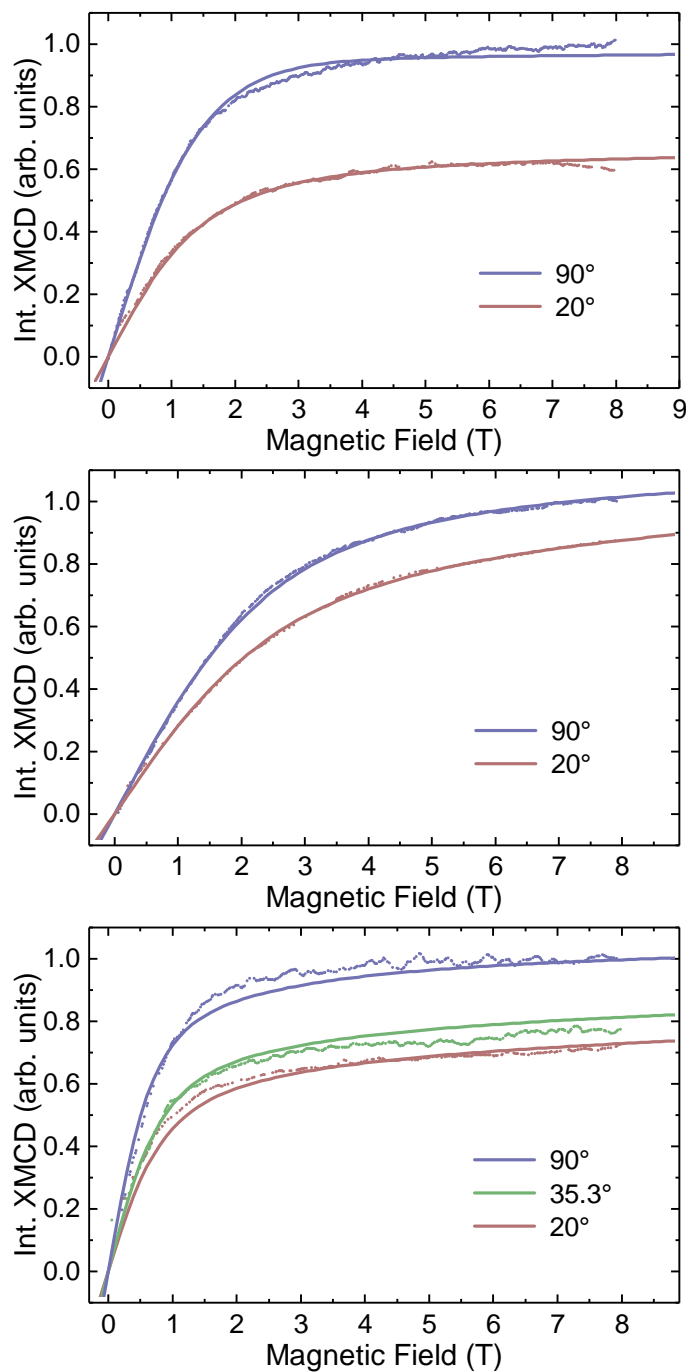


Figure 4.7: XMCD M_5 edge maximum peak intensity as a function of external field for $Dy(TMHD)_3$ molecules deposited on HOPG (top), graphene/Ni/W(110) (center), and graphene/Ir(111) (bottom), displayed as dots. Corresponding spin-Hamiltonian fits are displayed as lines. The temperature was 2.4 K for the graphene/Ir(111) substrate, 7.8 K for the others.

Table 4.4: Fit parameters for the magnetization curves of the Dy(TMHD)₃ molecules.

<i>Substrate</i>	<i>D</i> (meV)	ϕ (°)	<i>T</i> (K)
HOPG	-1.78	45.71	6.8
graphene/Ni/W(110)	0.17	64.54	9.0
graphene/Ir(111)	0.56	87.28	2.4

the sample cooling shield during those experiments. The fit parameters obtained from the model are displayed in Table 4.4. D is the uniaxial anisotropy parameter in Eqn. 4.1, ϕ is the angle between the quantization axis of the ion and the substrate normal, and T is the temperature. The parameters for the total angular momentum ($J = 15/2$) and Landé factor ($g_J = 4/3$) were taken from existing literature [83].

On the graphene/Ir(111) substrate, the fit indicates a quantization axis lying almost completely parallel to the plane of the substrate. As discussed before, this configuration is not unusual, as it has been observed before in similar molecules [79] and is a possible outcome of the highly symmetric shape formed by the molecular ligands around the ion. The value obtained for the uniaxial anisotropy in this system, $D = 0.56$ meV, indicates a substantial anisotropy energy with an easy plane perpendicular to the plane of the substrate, which results in the normal incidence measurement coinciding with the easy direction of magnetization, while the molecular orbitals mainly responsible for the XMCD signal are in-plane 4f orbitals. The temperature obtained from the fit procedure matches the nominal temperature very well for this substrate.

Once the model parameters are obtained from the fit, one can extrapolate the field to very high values to obtain the saturation magnetization of these systems. In the case of the molecules deposited on graphene/Ir(111) it was verified that the moment obtained from the sum rules for the system at 8 T was about 32% lower than the magnetic saturation value under the magic angle of incidence. One can then obtain the final value for the sum-rule calculated total magnetic moment, in this case $m_T = 8.2 \mu_B$. This value corresponds to an error of less than 20% to the expected value of $10 \mu_B$ for Dy(III), which is a very good agreement when one considers the multiple sources of error present in the sum-rules calculation discussed previously.

When the dysprosium ion was deposited directly on graphene/Ir(111) [84], it was verified that there was a ferromagnetic behavior. The hysteresis formed in that case would disappear for higher temperatures (12 K) or even a higher fluence

of the x-rays [82]. The measurements performed for the $Dy(TMHD)_3$ molecules on the graphene/Ir(111) substrate were also in the same temperature range as in the two studies mentioned, but evidence of magnetic bistability is inconclusive. A small remanence is observed in the normal incidence field-dependent scans, but it is not large enough to rule out experimental artifacts. The significant dependence on the photon flux could also help explain the absence of a clear hysteresis in our experiments. The most likely scenario, however, is that in the case of the $Dy(TMHD)_3$ molecules the central ion is essentially further shielded from substrate interaction, helping maintain the trivalent state commonly found for dysprosium ions in nature. Baltic et al. [84, 82] describes the dysprosium ions nestling on individual graphene hollow sites, which likely generates maximum substrate interaction.

While previous discussion has shown great similarities between the XMCD spectra of $Dy(TMHD)_3$ on the three different substrates, Fig. 4.7 clearly shows that this is not the case for the magnetization of the different systems. The molecules deposited on graphene/Ni/W(110) in particular appear to display very different properties as the other two substrates, with an apparently lower anisotropy and relative saturation at 8 T. Only the lower anisotropy is supported by the parameters obtained from the fitting procedure, however. As can be verified in Table 4.4, a low value of $D = 0.17$ is indeed obtained. This anisotropy, about three times lower than the one obtained from the molecule deposited on graphene/Ir(111), is initially surprising, since there is not such a significant difference in the structure of the substrates. Both the Ni(111) surface formed through deposition of Ni atoms on top of W(110) [58] and the Ir(111) surface have the same structure, although the larger radius of the iridium atoms could result in different interactions with dysprosium ions, it is unlikely this would still be significant through the graphene layer and the substrate separation caused by the ligands. It is important to consider, however, that the lattice parameter of graphene differs from the one of the Ir(111) surface by about 10% [85]. This lattice mismatch generates a moiré pattern that is not present in the graphene/Ni/W(110) substrate, since the lattice mismatch between graphene and the Ni(111) surface formed is only about 1%. The large lattice mismatch of the graphene/Ir(111) substrate contributes to a larger graphene-metal distance in this substrate, between 3.4 and 4 Å. For the Ni substrate, this distance is just 2.1 Å. A high degree of interaction is observed between the Ni substrate and the graphene, with hybridization between the π orbitals of the graphene and the d_{z^2} orbitals of the Ni [86]. This situation results in a favored interaction between graphene and dysprosium on the Ni substrate, while a direct Ir-Dy interaction

might be possible on the other sample. In addition to these differences in the electronic configuration of the two graphene substrates studied here, another important factor is the quality of the graphene layer in the two cases. While on the Ni(111) the graphene lattice constant accompanies the contraction of the metal when it is brought to room temperature, because it goes from an expanded to a more relaxed state, on the Ir(111) this doesn't happen, because the graphene on the latter substrate is already close to the lattice constant of graphite and contracts insignificantly when cooled down. This generates a graphene layer that usually contains large wrinkles on Ir(111) but is relatively free of them on Ni(111) [86]. This structural difference could very likely promote distinct adsorption configuration for the (TMHD)₃ ligands. A significant symmetry alteration is then expected for these molecules. This is evidenced by the value obtained from the fit for the direction of the quantization axis of the dysprosium ion's 4f orbitals, which, in the case of the molecules deposited on graphene/Ni/W(110), has an angle of about 65°, as can be verified in Table 4.4.

The saturation value of the magnetization is not much different than in the case of the graphene/Ir(111) substrate, resulting in a value in saturation 29% higher than the magnetic moment obtained from the sum rules of the spectra taken at 8 T. This is surprising, as the lower temperature of the graphene/Ir(111) sample was expected to give a higher relative saturation, but in combination with the other fit parameters, the model produces a saturation value for the magnetization not much higher than what is obtained experimentally at 8 T. The higher angle between quantization axis and the normal to the substrate, in particular, contributes to this result, as the averaging procedure of the model appears to cause an overall stronger reduction in the value obtained for the magnetization in this sample. This results in a saturated magnetic moment given by $m_T = 7.1 \mu_B$ on the graphene/Ni/W(110) substrate. Although greater than the error encountered for the molecules deposited on graphene/Ir(111), the error of less than 30% is still acceptable for the Dy(III) ion, so there is little indication of a change in the valence of the central ion deposited on this substrate.

The uniaxial anisotropy value obtained from the molecules deposited on the HOPG substrate were the highest obtained among all substrates presented here, with a value $D = -1.78$ meV. The negative value of D points to a strong uniaxial anisotropy with an easy axis pointing along the direction of the quantization axis of the 4f orbitals. The angle for this direction, obtained from the fit, is 45°. This is another result unique to the HOPG substrate. This high uniaxial anisotropy is indicative that the interaction with the substrate is responsible for its reduction, given that the HOPG is expected to be the least reactive among the

three substrates. Another consequence of the low substrate interaction on this substrate is the angle between the quantization axis and the surface normal. This is the lowest among the three substrates and indicates a more isotropic molecular symmetry, where the direction of the quantization axis is mostly defined by the surface plane rather than deformation to the molecular ligands.

The results obtained from the fit procedure show the importance of the correct determination of the orientation of the quantization axis of the 4f orbitals. The interplay between this orientation and the magnitude of the uniaxial magnetic anisotropy may result in similar magnetization curves with very different properties, as can be verified in Fig. 4.7 when one compares the HOPG and graphene/Ir(111) curves. Only when the spin-Hamiltonian model is applied one is able to determine more clearly what are the actual values of these parameters. Among the studied substrates, HOPG is the most interesting one, for it promotes the highest magnetic anisotropy in these molecules. This is, however, closely related to the small interaction between the HOPG substrate and the dysprosium ion, which is not necessarily a desirable feature for the application of these molecules in magnetic devices, especially when higher temperature applications are considered and the ligands are not enough to anchor the molecule in a fixed position.

4.3 $\text{Er}(\text{TMHD})_3$

The $\text{Er}(\text{TMHD})_3$ molecules presented here were deposited on two different substrates, graphene/Ni/W(110) and Au(111). The graphene substrate was used to study the differences that take place by the modification of only the central ion of the molecule, while maintaining the same ligands and substrate. The Au(111) substrate was used in order to understand what happens when a more reactive substrate is used. Fig 4.8 shows the spectra of $\text{Er}(\text{TMHD})_3$ deposited on the two substrates under three different angles of incidence. The temperature of the measurements was 7.8 K. Although the same peak structure is observed on the two substrates, the angle dependence is much more significant for the molecules deposited on the gold substrate. If one compares the erbium molecule deposited on graphene with the dysprosium molecule deposited on the same substrate discussed in the previous section, the higher degree of angle dependence of Er is already evident. For the erbium molecules deposited on the gold substrate this angle dependence is even more significant. It was previously stated that a higher degree of interaction between the substrate and lanthanide ion would promote a stronger angle dependence due to lower symmetry of the ligands on

these substrates. This is verified once again for the erbium molecules, where the gold substrate is expected to be much more reactive, generating sharper modifications to the molecules' conformation.

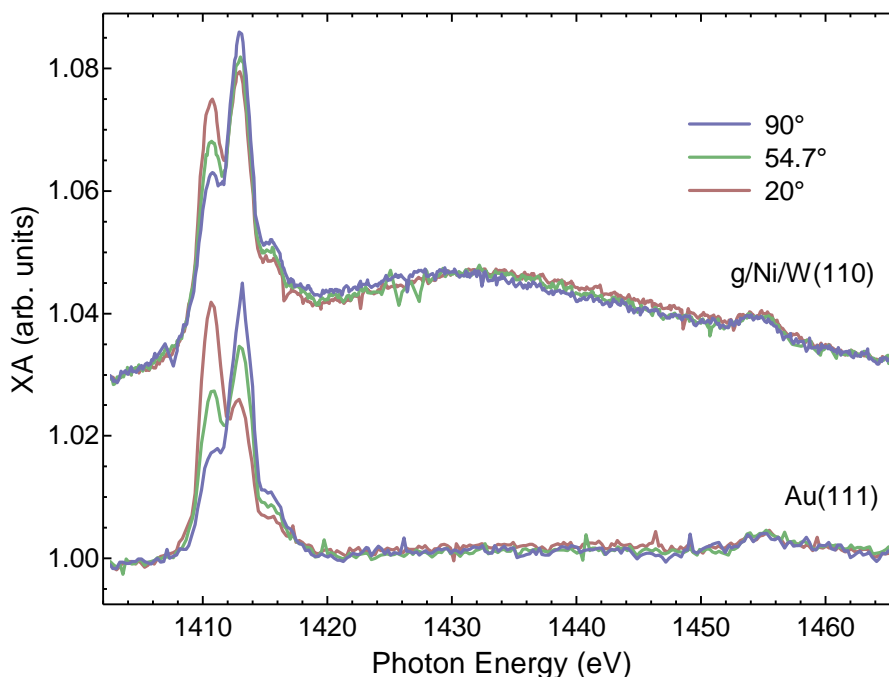


Figure 4.8: XA spectra of the Er $M_{4,5}$ edges of $\text{Er}(\text{TMHD})_3$ molecules on two different substrates for three angles of incidence of the linearly polarized x-rays. The temperature was 7.8 K.

The difference in the line shape of the spectra for the two substrates indicates distinct electronic configurations. Giving the shielded nature of the lanthanides valence orbitals, such variation is unlikely to be the result of mere conformation or electronic changes within the molecule, and is most probably the result of an erbium-substrate interaction. This is supported by the results obtained from the fit of the magnetization curves, to be discussed later, where we get the best fit on the graphene/Ni/W(110) substrate with $J = 15/2$, corresponding to the usual +3 oxidation state of the free molecule, while on Au(111) the best fit is achieved for $J = 8$. This value for J on Au(111) would indicate an oxidation state +4, though, and that is very unusual for Er ions. A more likely scenario is the one in which a valence orbital of the erbium ion hybridizes with the gold substrate. This possibility is further asserted by the high reactivity of the gold substrate, specially when we compare to the other substrates studied here.

Circularly polarized XA and XMCD of $\text{Er}(\text{TMHD})_3$ are presented on Fig. 4.9

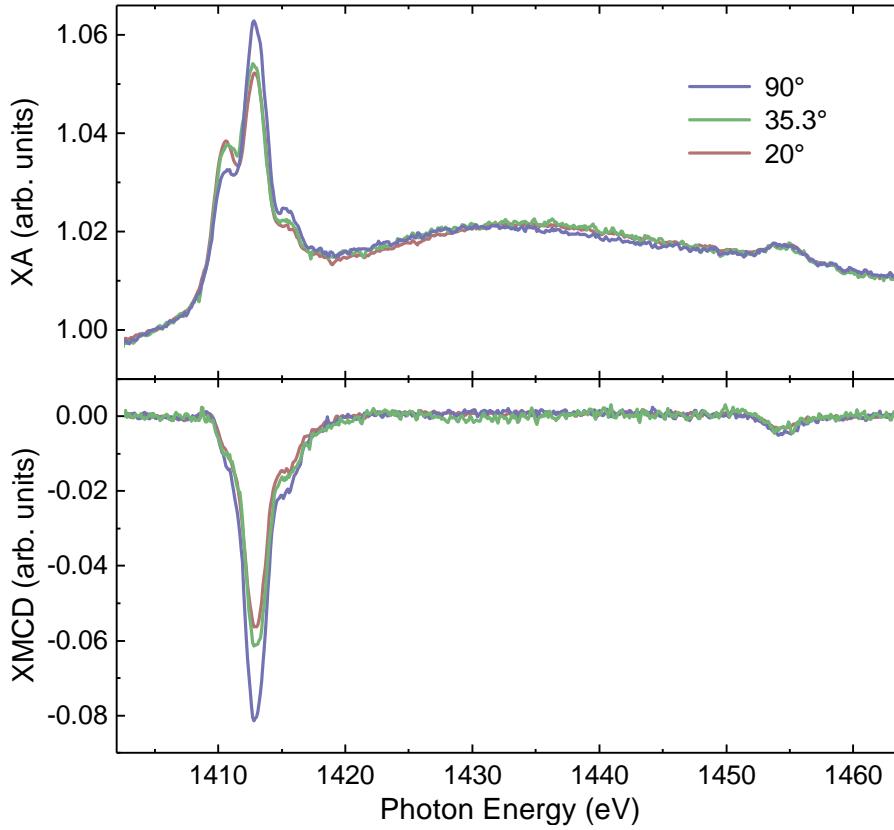


Figure 4.9: XA and XMCD spectra of the Er $M_{4,5}$ edges of $\text{Er}(\text{TMHD})_3$ molecules on graphene/Ni/W(110) for three angles of incidence of the circularly polarized x-rays. The temperature was 7.8 K and the magnetic field was 8 T.

for three angles of incidence on the graphene/Ni/W(110) substrate. The temperature of the measurements was 7.8 K and the external magnetic field along the direction of the x-rays was set to 8 T. The expected total magnetic moment for an Er(III) ion is $m_T = 9 \mu_B$, and a substantial XMCD is indeed observed. Sum rule analysis gives a total moment $m_T = 6.7(7) \mu_B$ (see Table 4.5) for the spectra in Fig. 4.9 under magic angle of incidence and magnetic field. As usual, the most intense XMCD signal is recorded under normal incidence, pointing to an out-of-plane easy axis of magnetization.

There is no significant difference between the XMCD spectra of the $\text{Er}(\text{TMHD})_3$ deposited on graphene/Ni/W(110) and on Au(111), displayed on Fig. 4.10. Even the sum rule analysis, of which the results can be seen in Table 4.6, are very close to the results obtained on the graphene substrate, albeit a bit lower. This would imply a reduction of the total magnetic moment of the erbium ion of the

Table 4.5: Moments obtained from the sum rules for $\text{Er}(\text{TMHD})_3$ on graphene/Ni/W(110) at 7.8 K and 8 T.

α	$m_L(\alpha)/\mu_B$	$m_S^{\text{eff}}(\alpha)/\mu_B$
90°	4.2 ± 0.5	3.4 ± 0.5
35.3°	3.6 ± 0.4	3.1 ± 0.3
20°	3.1 ± 0.4	2.8 ± 0.3

Table 4.6: Moments obtained from the sum rules for $\text{Er}(\text{TMHD})_3$ on Au(111) at 7.8 K and 8 T.

α	$m_L(\alpha)/\mu_B$	$m_S^{\text{eff}}(\alpha)/\mu_B$
90°	4.6 ± 0.9	3.8 ± 0.3
35.3°	3.2 ± 0.5	3.1 ± 0.4
20°	3.0 ± 0.4	2.9 ± 0.5

molecules deposited on Au(111), but further investigation of the magnetization curves is required. The magnetic moment results obtained from the sum rules for normal incidence appear to be a bit higher for the Au samples, but this can be attributed to the experimental error. For the Au(111) substrate samples, the sum rules were calculated for the unusual Er(IV) oxidation state. The total angular momentum of this state produced the best agreement with experiment in the fit of the magnetization curves, to be discussed in the following.

In order to obtain more information regarding the magnetic anisotropy of the samples containing erbium, spin-Hamiltonian fits of the magnetization as a function of external field were performed, using the same model as was done previously for the dysprosium samples. The experimental curves and resulting fits are presented in Fig. 4.11. It is important to mention that, while for the dysprosium samples the best fits were obtained for a total angular momentum value corresponding to $J = 15/2$, the usual value for both Dy(III) and Er(III), only the $\text{Er}(\text{TMHD})_3$ molecule deposited on graphene/Ni/W(110) had the best fit corresponding to this value for the total angular momentum. For the molecules deposited on Au(111), the best fit was obtained for $J = 8$, which would correspond to an oxidation state Er(IV). This is not necessarily the oxidation state of the ion, and further investigation would be required to determine this with more certainty, particularly because erbium is not usually found in this oxidation state. But it could nonetheless indicate a higher level of substrate interaction, expected for this substrate, and would help explain the significant differences observed in

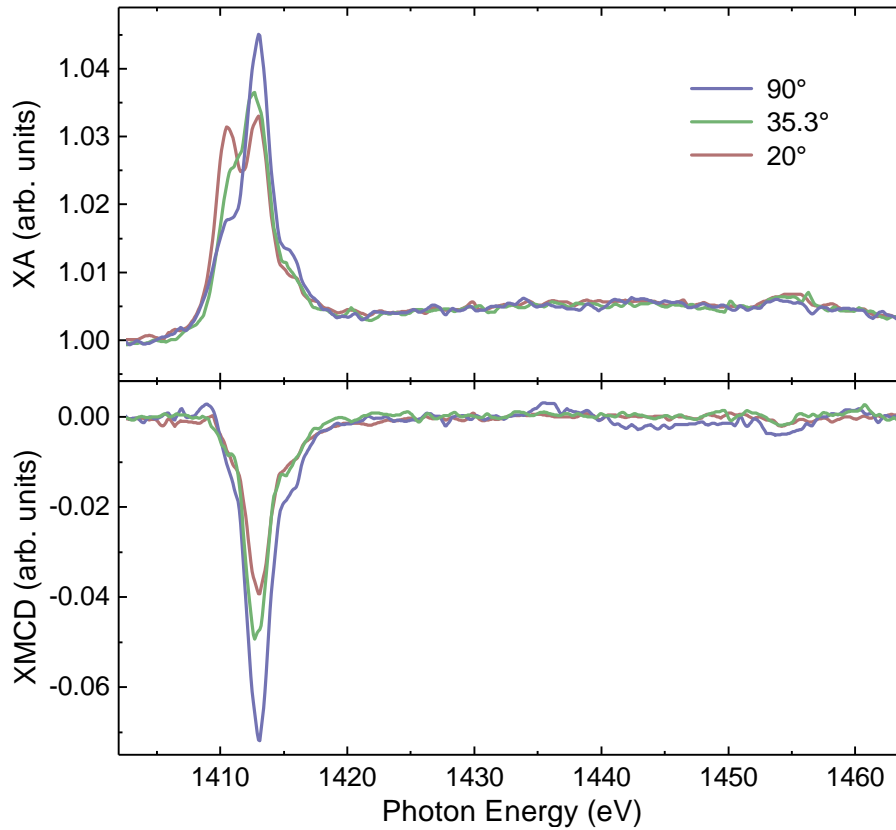


Figure 4.10: XA and XMCD spectra for the Er $M_{4,5}$ edges of $\text{Er}(\text{TMHD})_3$ molecules on Au(111) for three angles of incidence of the circularly polarized x-rays. The temperature was 7.8 K and the magnetic field was 8 T.

the magnetization curves of the two samples.

Although the experimental curves of Fig. 4.11 seem to indicate that the molecules deposited on Au(111) are closer to saturation than the ones deposited on graphene/Ni/W(110), this is not what is obtained from the fit results. The extrapolation of the fit parameter to high magnetic field indicate that the relative saturation of the magnetization of the graphene/Ni/W(110) sample is about 69% at the 8 T field of the experiment, while for the Au(111) sample it is about 61%. To account for the difference in the curvature of the experimental curves under different angles of incidence, the fit procedure relied heavily on the temperature parameter, which was the highest value obtained from all samples in the case of the graphene/Ni/W(110) substrate, and the lowest for Au(111). The fit temperature of the graphene sample is, however, matching the one obtained for the dysprosium molecules deposited on the same substrate. These variation in

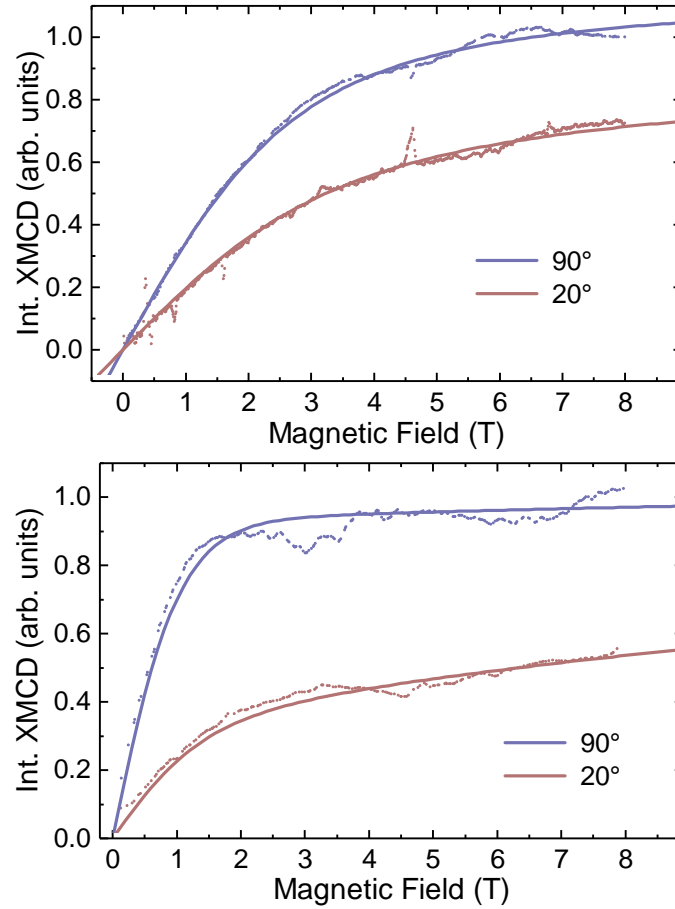


Figure 4.11: XMCD M_5 edge maximum peak intensity as a function of external field for $\text{Er}(\text{TMHD})_3$ molecules deposited on graphene/Ni/W(110) (top), and Au(111) (bottom), displayed as dots. Corresponding spin-Hamiltonian fits are displayed as lines. The temperature was 7.8 K.

the temperature of the sample are reasonable, considering the fact that these different materials have distinct thermal conductances, which may very well result in considerable differences in the minimum temperature achievable by the equipment, as the experiment was trying to reproduce.

Table 4.7 also shows that the easy direction of magnetization on both systems is not parallel to the plane of the substrate. In the case of the molecules deposited on graphene/Ni/W(110), the parameters obtained between the angle of the quantization axis of the 4f orbitals and the substrate normal is 90° , and the uniaxial magnetic anisotropy has a value $D = 0.87$ meV. This significantly high anisotropy is oriented perpendicular to the plane of the substrate. In the case of

Table 4.7: Fit parameters for the magnetization curves of the $\text{Er}(\text{TMHD})_3$ molecules.

<i>Substrate</i>	$D(\text{meV})$	$\phi(^{\circ})$	$T(\text{K})$
graphene/Ni/W(110)	0.87	90	9.4
Au(111)	-0.19	30.18	6.0

the Au(111) substrate, the value of the uniaxial anisotropy is considerably lower in magnitude, $D = -0.19 \text{ meV}$, and this time the negative sign of D indicates an anisotropy along the quantization axis of the 4f orbitals, in this case only about 30° from the substrate normal.

CONCLUSIONS

In this thesis, a study of the electronic and magnetic properties of two classes of metal complexes was presented, namely transition-metal porphyrins and lanthanide molecules. They were investigated by means of x-ray absorption spectroscopy (XAS) and x-ray magnetic circular dichroism (XMCD), with a focus on how the interaction with the substrates on which they are deposited is affected by the choice of substrate, molecular macrocycle, and metallic ion. The transition-metal molecules were additionally subjected to elevated temperatures that induced an intramolecular ring-closure reaction, transforming octaethylporphyrins (OEP) into tetrabenzoporphyrins (TBP) and thus changing the macrocycle that surrounds the metallic ion and the ligand field experienced by it.

The FeOEP molecules were deposited on Au(111) and graphene/Ni/W(110). The molecule exhibited paramagnetism on both substrates and very similar spectra, showing that there is little consequence to the molecules' electronic configurations from the influence of the substrate. The ring closure-reaction is verified with the K edge spectra of the N atoms around the Fe. The closed-ring molecules obtained after the reaction are also similar on the two substrates, exhibiting an increase in the XMCD signal on both. Density functional theory calculations for the molecules deposited on Au(111) predict an increased occupation of the d_{π} orbitals and a larger distance between Fe and substrate, with no change in the magnetic spin moment ($S = 1$) of the molecules after ring-closure, which entails that the increase in the XMCD signal must be caused by variations in the uniaxial and spin-density anisotropies. This is confirmed by the spin-Hamiltonian fit of the magnetization of the Fe ion. The uniaxial magnetic anisotropy is reduced from $D = 1.72$ meV on the FeOEP to $D = 0.36$ meV on the FeTBP, representing an easy plane of magnetization parallel to the substrate. The geometry of the molecule is also predicted to be much flatter after ring closure. While these calculation were not performed for the molecules deposited on the graphene/Ni/W(110) substrate, the similarities in the spectra of the molecules in the two substrates measured lead to the conclusion that similar effects are experienced by the molecules deposited on graphene.

The Co porphyrin molecules were deposited on Au(100), Cu(100), and Cu(111) in addition to the substrates used for the Fe molecule. On the graphene substrate,

Conclusions

the changes to the XAS and XMCD spectra brought by the ring closure are minimal, pointing to much weaker interaction of the ligands and central ion with the substrate in this sample than in the FeOEP, as the changes in the chemical structure of the molecule do not produce significant effects in the properties of the central ion. The graphene layer in this case appears to act as a buffer layer that isolates the central ion from interaction with the Ni layers underneath, something that is not observed in the FeOEP sample. For the molecules deposited on metallic substrates, however, sharp changes are observed in the properties of the Co between different substrates and before and after ring closure. While a significant spin moment is observed in the CoOEP/Cu(100) sample, it is completely quenched in every other metallic substrate used, indicating that a strong interaction with these substrates is responsible for the quenching of the spin moment. After ring closure the spin moment is also quenched on the Cu(100) substrate and the electronic configuration of the Co ion is very similar to that on the Cu(111) sample, leading to the conclusion that the structures and substrate interactions are similar in both cases after the reaction. The fit of the magnetization curves of the CoOEP/Cu(100) sample reveals a very small magnetic anisotropy ($D = 0.04 \text{ meV}$) and the sum rules indicate a spin moment $S = 1$.

The magnetization of the two tris(tetramethylheptanedionate) ((TMHD)₃) molecules investigated, with Dy and Er as lanthanide metal centers, showed strong dependence on the substrate onto which they were deposited. For the Dy(TMHD)₃ deposited on carbon-based substrates (highly-ordered pyrolytic graphite (HOPG), graphene/Ni/W(110), and graphene/Ir(111)), while the changes to the electronic structure of the central ion were not significant, as expected for lanthanides, the orientation and magnitude of the uniaxial anisotropy change substantially. On the graphene/Ni/W(110) substrate, the influence of the ferromagnetic Ni layer appears to be limited, as evidenced by the lack of magnetization observed for zero external field. It is interesting, however, that on this substrate the magnetic saturation and magnitude of the uniaxial anisotropy is lower than in the other two samples. For this molecule, the highest value of magnetic anisotropy was observed on the HOPG substrate, where $D = -1.78 \text{ meV}$. The ligand structure of these molecules is easily distorted by the introduction of the substrate, leading to a strong dependence on its structure that results in the different orientations of the molecules' quantization axis on each substrate. Similar differences are observed for the Er(TMHD)₃ molecules deposited on graphene/Ni/W(110) and Au(111), but here they are more significant due to the higher reactivity of the Au substrate, with noticeable distinctions in the

electronic structure of the ion centers. The quantization axis of the $4f$ orbitals, parallel to the substrate on the graphene substrate, is only about 30° from the surface normal on Au.

The investigation of the molecules presented here on different substrates leads to a better understanding of how the properties of their metallic central ion are affected by the interaction with the atoms of the substrate. The degree of reactivity of the substrates is seen to be an important factor for the metal's magnetism, directly through ion-substrate, and indirectly through ligand-substrate interactions. These findings provide ways to enhance desirable magnetic properties by designing adequate combinations of ligands and substrates in order to fine-tune their interaction. Further investigation of additional ways to affect these properties is necessary, with attractive options being the addition of axial ligands to the molecules, both in their synthesis or post-deposition, and the use of intermolecular reaction as means of modifying the magnetic properties of the central ion.

BIBLIOGRAPHY

- [1] J. M. Manriquez, G. T. Yee, R. S. Mclean, A. J. Epstein, and J. S. Miller, “A Room-Temperature Molecular/Organic-Based Magnet,” *Science*, vol. 252, no. 5011, pp. 1415–1417, 1991.
- [2] K. I. Pokhodnya, D. Pejakovic, A. J. Epstein, and J. S. Miller, “Effect of solvent on the magnetic properties of the high-temperatureV[TCNE]xmolecule-based magnet,” *Phys. Rev. B*, vol. 63, no. 17, p. 174408, 2001.
- [3] B. Li, C.-Y. Kao, J.-W. Yoo, V. N. Prigodin, and A. J. Epstein, “Magnetoresistance in an All-Organic-Based Spin Valve,” *Advanced Materials*, vol. 23, no. 30, pp. 3382–3386, 2011.
- [4] S. Venkataramani, U. Jana, M. Dommaschk, F. D. Sonnichsen, F. Tucek, and R. Herges, “Magnetic Bistability of Molecules in Homogeneous Solution at Room Temperature,” *Science*, vol. 331, no. 6016, pp. 445–448, 2011.
- [5] H. Eguchi, M. Umemura, R. Kurotani, H. Fukumura, I. Sato, J.-H. Kim, Y. Hoshino, J. Lee, N. Amemiya, M. Sato, K. Hirata, D. J. Singh, T. Masuda, M. Yamamoto, T. Urano, K. Yoshida, K. Tanigaki, M. Yamamoto, M. Sato, S. Inoue, I. Aoki, and Y. Ishikawa, “A magnetic anti-cancer compound for magnet-guided delivery and magnetic resonance imaging,” *Scientific Reports*, vol. 5, p. 9194, 2015.
- [6] I. Sato, M. Umemura, K. Mitsudo, H. Fukumura, J.-H. Kim, Y. Hoshino, H. Nakashima, M. Kioi, R. Nakakaji, M. Sato, T. Fujita, U. Yokoyama, S. Okumura, H. Oshiro, H. Eguchi, I. Tohnai, and Y. Ishikawa, “Simultaneous hyperthermia-chemotherapy with controlled drug delivery using single-drug nanoparticles,” *Scientific Reports*, vol. 6, no. 1, 2016.
- [7] M. Ohtake, M. Umemura, I. Sato, T. Akimoto, K. Oda, A. Nagasako, J.-H. Kim, T. Fujita, U. Yokoyama, T. Nakayama, Y. Hoshino, M. Ishiba, S. Tokura, M. Hara, T. Muramoto, S. Yamada, T. Masuda, I. Aoki, Y. Take-mura, H. Murata, H. Eguchi, N. Kawahara, and Y. Ishikawa, “Hyperthermia and chemotherapy using Fe(Salen) nanoparticles might impact glioblastoma treatment,” *Scientific Reports*, vol. 7, no. 1, p. 42783, 2017.

Bibliography

- [8] S. Sanvito, "Molecular spintronics," *Chem. Soc. Rev.*, vol. 40, pp. 3336–3355, 2011.
- [9] G. A. Landrum and R. Dronskowski, "The Orbital Origins of Magnetism: From Atoms to Molecules to Ferromagnetic Alloys," *Angewandte Chemie International Edition*, vol. 39, no. 9, pp. 1560–1585, 2000.
- [10] H. H. Wickman, A. M. Trozzolo, H. J. Williams, G. W. Hull, and F. R. Merritt, "Spin-3/2 Iron Ferromagnet: Its Mössbauer and Magnetic Properties," *Phys. Rev.*, vol. 155, no. 2, pp. 563–566, 1967.
- [11] R. Sessoli, H. L. Tsai, A. R. Schake, S. Wang, J. B. Vincent, K. Folting, D. Gatteschi, G. Christou, and D. N. Hendrickson, "High-spin molecules: $[\text{Mn}_{12}\text{O}_{12}(\text{O}_2\text{CR})_{16}(\text{H}_2\text{O})_4]$," *J. Am. Chem. Soc.*, vol. 115, no. 5, pp. 1804–1816, 1993.
- [12] M. Reiher, "Theoretical Study of the $\text{Fe}(\text{phen})_2(\text{NCS})_2$ Spin-Crossover Complex with Reparametrized Density Functionals," *Inorganic Chemistry*, vol. 41, no. 25, pp. 6928–6935, 2002.
- [13] M. Bernien, J. Miguel, C. Weis, M. E. Ali, J. Kurde, B. Krumme, P. M. Panchmatia, B. Sanyal, M. Piantek, P. Srivastava, K. Baberschke, P. M. Oppeneer, O. Eriksson, W. Kuch, and H. Wende, "Tailoring the Nature of Magnetic Coupling of Fe-Porphyrin Molecules to Ferromagnetic Substrates," *Phys. Rev. Lett.*, vol. 102, no. 4, p. 047202, 2009.
- [14] D. Gatteschi, R. Sessoli, and J. Villain, *Molecular Nanomagnets*. Oxford: Oxford University Press, 2006.
- [15] L. Grill, M. Dyer, L. Lafferentz, M. Persson, M. V. Peters, and S. Hecht, "Nano-architectures by covalent assembly of molecular building blocks," *Nat. Nanotechnol.*, vol. 2, no. 11, pp. 687–691, 2007.
- [16] B. W. Heinrich, G. Ahmadi, V. L. Müller, L. Braun, J. I. Pascual, and K. J. Franke, "Change of the Magnetic Coupling of a Metal–Organic Complex with the Substrate by a Stepwise Ligand Reaction," *Nano Lett.*, vol. 13, no. 10, pp. 4840–4843, 2013.
- [17] G. Franc and A. Gourdon, "Covalent networks through on-surface chemistry in ultra-high vacuum: state-of-the-art and recent developments," *Phys. Chem. Chem. Phys.*, vol. 13, no. 32, pp. 14283–14292, 2011.

- [18] M. Lackinger and W. M. Heckl, "A STM perspective on covalent intermolecular coupling reactions on surfaces," *J. Phys. D: Appl. Phys.*, vol. 44, no. 46, p. 464011, 2011.
- [19] M. Lepper, L. Zhang, M. Stark, S. Ditze, D. Lungerich, N. Jux, W. Hieringer, H.-P. Steinrück, and H. Marbach, "Role of Specific Intermolecular Interactions for the Arrangement of Ni(II)-5, 10, 15, 20-Tetraphenyltetrabenzoporphyrin on Cu(111)," *J. Phys. Chem. C*, vol. 119, no. 34, pp. 19897–19905, 2015.
- [20] C. G. Williams, M. Wang, D. Skomski, C. D. Tempas, L. L. Kesmodel, and S. L. Tait, "Dehydrocyclization of peripheral alkyl groups in porphyrins at Cu(100) and Ag(111) surfaces," *Surf. Sci.*, vol. 653, pp. 130–137, 2016.
- [21] B. Cirera, N. Giménez-Agulló, J. Björk, F. Martínez-Peña, A. Martín-Jimenez, J. Rodríguez-Fernandez, A. M. Pizarro, R. Otero, J. M. Gallego, P. Ballester, J. R. Galan-Mascaros, and D. Eciija, "Thermal selectivity of intermolecular versus intramolecular reactions on surfaces," *Nat. Commun.*, vol. 7, p. 11002, 2016.
- [22] D. Heim, D. Eciija, K. Seufert, W. Auwärter, C. Aurisicchio, C. Fabbro, D. Bonifazi, and J. V. Barth, "Self-Assembly of Flexible One-Dimensional Coordination Polymers on Metal Surfaces," *J. Am. Chem. Soc.*, vol. 132, no. 19, pp. 6783–6790, 2010.
- [23] L. Lafferentz, V. Eberhardt, C. Dri, C. Africh, G. Comelli, F. Esch, S. Hecht, and L. Grill, "Controlling on-surface polymerization by hierarchical and substrate-directed growth," *Nat. Chem.*, vol. 4, no. 3, pp. 215–220, 2012.
- [24] H.-Y. Gao, H. Wagner, D. Zhong, J.-H. Franke, A. Studer, and H. Fuchs, "Glaser Coupling at Metal Surfaces," *Angew. Chem. Int. Ed.*, vol. 52, no. 14, pp. 4024–4028, 2013.
- [25] N. Ballav, C. Wäckerlin, D. Siewert, P. M. Oppeneer, and T. A. Jung, "Emergence of On-Surface Magnetochemistry," *J. Phys. Chem. Lett.*, vol. 4, no. 14, pp. 2303–2311, 2013.
- [26] K. Flechtner, A. Kretschmann, H.-P. Steinrück, and J. M. Gottfried, "NO-Induced Reversible Switching of the Electronic Interaction between a Porphyrin-Coordinated Cobalt Ion and a Silver Surface," *J. Am. Chem. Soc.*, vol. 129, no. 40, pp. 12110–12111, 2007.

Bibliography

- [27] W. Hieringer, K. Flechtner, A. Kretschmann, K. Seufert, W. Auwärter, J. V. Barth, A. Görling, H.-P. Steinrück, and J. M. Gottfried, “The Surface Trans Effect: Influence of Axial Ligands on the Surface Chemical Bonds of Adsorbed Metalloporphyrins,” *J. Am. Chem. Soc.*, vol. 133, no. 16, pp. 6206–6222, 2011.
- [28] C. Isvoranu, B. Wang, E. Ataman, J. Knudsen, K. Schulte, J. N. Andersen, M.-L. Bocquet, and J. Schnadt, “Comparison of the Carbonyl and Nitrosyl Complexes Formed by Adsorption of CO and NO on Monolayers of Iron Phthalocyanine on Au(111),” *J. Phys. Chem. C*, vol. 115, no. 50, pp. 24718–24727, 2011.
- [29] P. Willmott, *An introduction to synchrotron radiation: techniques and applications*. John Wiley and Sons, 2011.
- [30] J. Stöhr, F. Sette, and A. L. Johnson, “Near-Edge X-Ray-Absorption Fine-Structure Studies of Chemisorbed Hydrocarbons: Bond Lengths with a Ruler,” *Phys. Rev. Lett.*, vol. 53, no. 17, pp. 1684–1687, 1984.
- [31] J. H. Hubbell, “Photon Cross Section Compilation Activity in the U.S. in the Range 1 keV to 100 GeV,” *Le Journal de Physique Colloques*, vol. 32, no. C4, pp. C4–14–C4–20, 1971.
- [32] H. Haken and H. C. Wolf, *Molecular Physics and Elements of Quantum Chemistry*. New York: Springer, 2004.
- [33] J. Stöhr, *NEXAFS Spectroscopy*. New York: Springer-Verlag, 1996.
- [34] F. de Groot and A. Kotani, *Core Level Spectroscopy of Solids*. Boca Raton: CRC Press, 2008.
- [35] M. Bernien, *X-Ray Absorption Spectroscopy of Molecular Magnetic Switches on Surfaces*. Habilitation thesis, Freie Universität Berlin, 2017.
- [36] J. Stöhr and H. C. Siegmann, *Magnetism – From Fundamentals to Nanoscale Dynamics*. New York: Springer-Verlag, 2006.
- [37] M. Bernien, *X-Ray absorption spectroscopy of Fe complexes on surfaces: Electronic interactions and tailoring of the magnetic coupling*. PhD thesis, Freie Universität Berlin, 2009.
- [38] J. Stöhr, “X-ray magnetic circular dichroism spectroscopy of transition metal thin films,” *J. Electron Spectrosc. Relat. Phenom.*, vol. 75, pp. 253–272, 1995.

- [39] F. Nickel, *Switching of Photochromic Molecules on Surfaces*. PhD thesis, Freie Universität Berlin, 2018.
- [40] J. Stöhr, “Exploring the microscopic origin of magnetic anisotropies with X-ray magnetic circular dichroism (XMCD) spectroscopy,” *J. Magn. Magn. Mater.*, vol. 200, no. 1-3, pp. 470–497, 1999.
- [41] B. T. Thole, P. Carra, F. Sette, and G. van der Laan, “X-ray circular dichroism as a probe of orbital magnetization,” *Phys. Rev. Lett.*, vol. 68, no. 12, pp. 1943–1946, 1992.
- [42] P. Carra, B. T. Thole, M. Altarelli, and X. Wang, “X-ray circular dichroism and local magnetic fields,” *Phys. Rev. Lett.*, vol. 70, no. 5, pp. 694–697, 1993.
- [43] C. T. Chen, Y. U. Idzerda, H.-J. Lin, N. V. Smith, G. Meigs, E. Chaban, G. H. Ho, E. Pellegrin, and F. Sette, “Experimental Confirmation of the X-Ray Magnetic Circular Dichroism Sum Rules for Iron and cobalt,” *Phys. Rev. Lett.*, vol. 75, no. 1, pp. 152–155, 1995.
- [44] Y. Teramura, A. Tanaka, B. Thole, and T. Jo, “Effect of Coulomb Interaction on the X-Ray Magnetic Circular Dichroism Spin Sum Rule in Rare Earths,” *J. Phys. Soc. Jpn.*, vol. 65, no. 9, pp. 3056–3059, 1996.
- [45] J. Stöhr and H. König, “Determination of Spin- and Orbital-Moment Anisotropies in Transition Metals by Angle-Dependent X-Ray Magnetic Circular Dichroism,” *Phys. Rev. Lett.*, vol. 75, no. 20, pp. 3748–3751, 1995.
- [46] O. Šipr, J. Minár, and H. Ebert, “On the importance of the magnetic dipole term T_z in analyzing X-ray magnetic circular dichroism spectra of clusters,” *Europhys. Lett.*, vol. 87, no. 6, p. 67007, 2009.
- [47] G. L. Miessler, P. J. Fischer, and D. A. Tarr, *Inorganic Chemistry*. Pearson, 2014.
- [48] C. J. Ballhausen, *Introduction to Ligand Field Theory*. New York: McGraw-Hill, 1962.
- [49] Y. Jean, *Molecular Orbitals of Transition Metal Complexes*. New York: Oxford, 2003.
- [50] X. Chen, L. Zhang, and S. Chen, “Large area CVD growth of graphene,” *Synthetic Metals*, vol. 210, pp. 95 – 108, 2015. Reviews of Current Advances in Graphene Science and Technology.

Bibliography

- [51] J. Coraux, A. T. N'Diaye, M. Engler, C. Busse, D. Wall, N. Buckanie, F.-J. M. zu Heringdorf, R. van Gastel, B. Poelsema, and T. Michely, "Growth of graphene on Ir(111)," *New Journal of Physics*, vol. 11, no. 2, p. 023006, 2009.
- [52] H. Ibach, *Physics of Surfaces and Interfaces*. Heidelberg: Springer, 2006.
- [53] F. Huttmann, N. Rothenbach, S. Kraus, K. Ollefs, L. M. Arruda, M. Bernien, D. Thonig, A. Delin, J. Fransson, K. Kummer, N. B. Brookes, O. Eriksson, W. Kuch, T. Michely, and H. Wende, "Europium Cyclooctatetraene Nanowire Carpets: A Low-Dimensional, Organometallic, and Ferromagnetic Insulator," *J. Phys. Chem. Lett.*, vol. 0, no. 0, pp. 911–917, 2019.
- [54] K. Heister, M. Zharnikov, M. Grunze, L. S. O. Johansson, and A. Ulman, "Characterization of X-ray Induced Damage in Alkanethiolate Monolayers by High-Resolution Photoelectron Spectroscopy," *Langmuir*, vol. 17, no. 1, pp. 8–11, 2001.
- [55] L. R. Milgrom, *The Colours of Life*. Oxford: Oxford University Press, 1997.
- [56] D. Voet, J. G. Voet, and C. W. Pratt, *Fundamentals of Biochemistry – Life at the Molecular level*. Wiley, 2016.
- [57] D. van Vörden, M. Lange, M. Schmuck, J. Schaffert, M. C. Cottin, C. A. Bobisch, and R. Möller, "Communication: Substrate induced dehydrogenation: Transformation of octa-ethyl-porphyrin into tetra-benzo-porphyrin," *J. Chem. Phys.*, vol. 138, no. 21, p. 211102, 2013.
- [58] C. F. Hermanns, *X-ray absorption studies of metalloporphyrin molecules on surfaces: Electronic interactions, magnetic coupling, and chemical switches*. PhD thesis, Freie Universität Berlin, 2013.
- [59] M. Stark, S. Ditze, M. Thomann, D. Lungerich, N. Jux, H.-P. Steinrück, and H. Marbach, "Reversible thermally induced phase transition in ordered domains of Co(II)-5, 10, 15, 20-tetrakis-(3, 5-di-tert-butylphenyl)-porphyrin on Cu(111)," *Surf. Sci.*, vol. 650, pp. 255–262, 2016.
- [60] C. Piamonteze, P. Miedema, and F. M. F. de Groot, "Accuracy of the spin sum rule in XMCD for the transition-metal L edges from manganese to copper," *Phys. Rev. B*, vol. 80, no. 18, p. 184410, 2009.
- [61] S. Stepanow, P. S. Miedema, A. Mugarza, G. Ceballos, P. Moras, J. C. Cezar, C. Carbone, F. M. F. de Groot, and P. Gambardella, "Mixed-valence

- behavior and strong correlation effects of metal phthalocyanines adsorbed on metals,” *Phys. Rev. B*, vol. 83, no. 22, p. 220401, 2011.
- [62] H. C. Herper, M. Bernien, S. Bhandary, C. F. Hermanns, A. Krüger, J. Miguel, C. Weis, C. Schmitz-Antoniak, B. Krumme, D. Bovenschen, C. Tieg, B. Sanyal, E. Weschke, C. Czekelius, W. Kuch, H. Wende, and O. Eriksson, “Iron porphyrin molecules on Cu(001): Influence of adlayers and ligands on the magnetic properties,” *Phys. Rev. B*, vol. 87, no. 17, p. 174425, 2013.
- [63] L. Floreano, A. Cossaro, R. Gotter, A. Verdini, G. Bavdek, F. Evangelista, A. Ruocco, A. Morgante, and D. Cvetko, “Periodic Arrays of Cu-Phthalocyanine Chains on Au(110),” *J. Phys. Chem. C*, vol. 112, no. 29, pp. 10794–10802, 2008.
- [64] J. Uihlein, H. Peisert, H. Adler, M. Glaser, M. Polek, R. Ovsyannikov, and T. Chassé, “Interface between FePc and Ni(111): Influence of Graphene Buffer Layers,” *J. Phys. Chem. C*, vol. 118, no. 19, pp. 10106–10112, 2014.
- [65] H. Peisert, J. Uihlein, F. Petraki, and T. Chassé, “Charge transfer between transition metal phthalocyanines and metal substrates: The role of the transition metal,” *J. Electron Spectrosc. Relat. Phenom.*, vol. 204, pp. 49–60, 2015.
- [66] H. Wende, M. Bernien, J. Luo, C. Sorg, N. Ponpandian, J. Kurde, J. Miguel, M. Piantek, X. Xu, P. Eckhold, W. Kuch, K. Baberschke, P. M. Panchmatia, B. Sanyal, P. M. Oppeneer, and O. Eriksson, “Substrate-induced magnetic ordering and switching of iron porphyrin molecules,” *Nat. Mater.*, vol. 6, no. 7, pp. 516–520, 2007.
- [67] C. F. Hermanns, K. Tarafder, M. Bernien, A. Krüger, Y.-M. Chang, P. M. Oppeneer, and W. Kuch, “Magnetic Coupling of Porphyrin Molecules Through Graphene,” *Adv. Mater.*, vol. 25, no. 25, pp. 3473–3477, 2013.
- [68] J. Miguel, C. F. Hermanns, M. Bernien, A. Krüger, and W. Kuch, “Reversible Manipulation of the Magnetic Coupling of Single Molecular Spins in Fe-Porphyrins to a Ferromagnetic Substrate,” *J. Phys. Chem. Lett.*, vol. 2, no. 12, pp. 1455–1459, 2011.
- [69] Y. Bai, M. Sekita, M. Schmid, T. Bischof, H.-P. Steinrück, and J. M. Gottfried, “Interfacial coordination interactions studied on cobalt octaethyl-

Bibliography

- porphyrin and cobalt tetraphenylporphyrin monolayers on Au(111),” *Phys. Chem. Chem. Phys.*, vol. 12, no. 17, p. 4336, 2010.
- [70] Y. Bai, F. Buchner, I. Kellner, M. Schmid, F. Vollnhals, H.-P. Steinrück, H. Marbach, and J. M. Gottfried, “Adsorption of cobalt(II) octaethylporphyrin and 2H-octaethylporphyrin on Ag(111): new insight into the surface coordinative bond,” *New J. Phys.*, vol. 11, no. 12, p. 125004, 2009.
- [71] S. Tognolini, S. Ponzoni, F. Sedona, M. Sambì, and S. Pagliara, “Role of the Substrate Orientation in the Photoinduced Electron Dynamics at the Porphyrin/Ag Interface,” *J. Phys. Chem. Lett.*, vol. 6, no. 18, pp. 3632–3638, 2015.
- [72] B. D. Cullity and C. D. Graham, *Introduction to Magnetic Materials*. Piscataway: Wiley, 2009.
- [73] C. Ederer, M. Komelj, J. W. Davenport, and M. Fähnle, “Comment on the analysis of angle-dependent X-ray magnetic circular dichroism in systems with reduced dimensionality,” *J. Electron Spectrosc. Relat. Phenom.*, vol. 130, no. 1-3, pp. 97–100, 2003.
- [74] M. Nakamura, R. Imai, N. Hoshi, and O. Sakata, “Interfacial structure of Co porphyrins on Au(111) electrode: Interaction of porphyrin molecules with substrate,” *Surf. Sci.*, vol. 606, no. 19-20, pp. 1560–1564, 2012.
- [75] B. Chilukuri, U. Mazur, and K. W. Hipps, “Effect of dispersion on surface interactions of cobalt(II) octaethylporphyrin monolayer on Au(111) and HOPG(0001) substrates: a comparative first principles study,” *Phys. Chem. Chem. Phys.*, vol. 16, no. 27, pp. 14096–14107, 2014.
- [76] C. Benelli and D. Gatteschi, *Introduction to Molecular Magnetism – From Transition Metals to Lanthanides*. Weinheim: Wiley-VCH, 2015.
- [77] R. Skomski, *Simple Models of Magnetism*. Oxford: Oxford University Press, 2008.
- [78] D. N. Woodruff, R. E. P. Winpenny, and R. A. Layfield, “Lanthanide Single-Molecule Magnets,” *Chem. Rev.*, vol. 113, no. 7, pp. 5110–5148, 2013. PMID: 23550940.
- [79] P. Stoll, M. Bernien, D. Rolf, F. Nickel, Q. Xu, C. Hartmann, T. R. Umbach, J. Kopprasch, J. N. Ladenthin, E. Schierle, E. Weschke, C. Czekelius,

- W. Kuch, and K. J. Franke, "Magnetic anisotropy in surface-supported single-ion lanthanide complexes," *Phys. Rev. B*, vol. 94, p. 224426, 2016.
- [80] J. B. Goedkoop, B. T. Thole, G. van der Laan, G. A. Sawatzky, F. M. F. de Groot, and J. C. Fuggle, "Calculations of magnetic x-ray dichroism in the 3d absorption spectra of rare-earth compounds," *Phys. Rev. B*, vol. 37, pp. 2086–2093, 1988.
- [81] M. Kubin, M. Guo, T. Kroll, H. Löchel, E. Källman, M. L. Baker, R. Mitzner, S. Gul, J. Kern, A. Föhlisch, A. Erko, U. Bergmann, V. Yachandra, J. Yano, M. Lundberg, and P. Wernet, "Probing the oxidation state of transition metal complexes: a case study on how charge and spin densities determine Mn L-edge X-ray absorption energies," *Chem. Sci.*, vol. 9, no. 33, pp. 6813–6829, 2018.
- [82] R. Baltic, F. Donati, A. Singha, C. Wäckerlin, J. Dreiser, B. Delley, M. Pivetta, S. Rusponi, and H. Brune, "Magnetic properties of single rare-earth atoms on graphene/Ir(111)," *Phys. Rev. B*, vol. 98, p. 024412, 2018.
- [83] J. D. Rinehart and J. R. Long, "Exploiting single-ion anisotropy in the design of f-element single-molecule magnets," *Chem. Sci.*, vol. 2, pp. 2078–2085, 2011.
- [84] R. Baltic, M. Pivetta, F. Donati, C. Wäckerlin, A. Singha, J. Dreiser, S. Rusponi, and H. Brune, "Superlattice of Single Atom Magnets on Graphene," *Nano Lett.*, vol. 16, no. 12, pp. 7610–7615, 2016. PMID: 27779891.
- [85] R. Brako, D. Šokčević, P. Lazić, and N. Atodiresei, "Graphene on the Ir(111) surface: from van der Waals to strong bonding," *New J. Phys.*, vol. 12, no. 11, p. 113016, 2010.
- [86] C.-M. Seah, S.-P. Chai, and A. R. Mohamed, "Mechanisms of graphene growth by chemical vapour deposition on transition metals," *Carbon*, vol. 70, pp. 1–21, 2014.

LIST OF ACRONYMS

AEY	Auger electron yield
APPLE	advanced planar polarized light emitter
BESSY	Helmholtz-Zentrum Berlin für Materialien und Energie (formerly Berliner Elektronenspeicherring-Gesellschaft für Synchrotronstrahlung mbH)
CFT	crystal field theory
CVD	chemical vapor deposition
DFT	density functional theory
DFT+ <i>U</i>	DFT with additional strong Coulomb correlation
DOS	density of states
EBE	electron-beam evaporator
EXAFS	extended x-ray absorption fine structure
GGA	generalized gradient approximation
HOMO	highest occupied molecular orbital
HOPG	highly ordered pyrolytic graphite
LCA	linear combination analysis
LEED	low-energy electron diffraction
LFT	ligand field theory
LINAC	linear accelerator
LUMO	lowest unoccupied molecular orbital
MCP	multichannel plate
MEED	medium-energy electron diffraction
ML	monolayer
MOKE	magneto-optic Kerr effect
NEXAFS	near edge x-ray absorption fine structure
OEP	octaethylporphyrin
Pc	phthalocyanine
PEY	partial electron yield
phen	1,10-phenanthroline
Py	pyridine
QMS	quadrupole mass spectrometer
RF	radio frequency
Salen	N,N'-bis(salicylidene)ethylenediamine

List of Acronyms

SCO	spin crossover
SMM	single-molecule magnet
STM	scanning tunneling microscopy
TBP	tetrabenzoporphyrin
TCNE	tetracyanoethylene
TEY	total electron yield
TMHD	tetramethylheptanedionate
UHV	ultra-high vacuum
VEKMAG	vectorial magnet
VTI	variable temperature insert
XA	x-ray absorption
XAS	x-ray absorption Spectroscopy
XMCD	x-ray magnetic circular dichroism
XNLD	x-ray natural linear dichroism
XPS	x-ray photoemission spectroscopy
ZFS	zero-field splitting

LIST OF PUBLICATIONS

L. M. Arruda, Md. E. Ali, M. Bernien, F. Nickel, J. Kopprasch, C. Czekelius, P. M. Oppeneer, and W. Kuch, "Modifying the Magnetic Anisotropy of an Iron Porphyrin Molecule by an On-Surface Ring-Closure Reaction," *J. Phys. Chem. C* (accepted).

F. Huttmann, N. Rothenbach, S. Kraus, K. Ollefs, L. M. Arruda, M. Bernien, D. Thonig, A. Delin, J. Fransson, K. Kummer, N. B. Brookes, O. Eriksson, W. Kuch, T. Michely, and H. Wende, "Europium Cyclooctatetraene Nanowire Carpets: A Low-Dimensional, Organometallic, and Ferromagnetic Insulator," *J. Phys. Chem. Lett.*, 10(5):911–917, 2019.

L. Kipgen, M. Bernien, S. Ossinger, F. Nickel, A. J. Britton, L. M. Arruda, H. Naggert, C. Luo, C. Lotze, H. Ryll, F. Radu, E. Schierle, E. Weschke, F. Tuczek, and W. Kuch, "Evolution of cooperativity in the spin transition of an iron(II) complex on a graphite surface," *Nat. Commun.*, 9(1):2984, 2018.

F. Nickel, M. Bernien, D. Krüger, J. Miguel, A. J. Britton, L. M. Arruda, L. Kipgen, and W. Kuch, "Highly Efficient and Bidirectional Photochromism of Spirooxazine on Au(111)," *J. Phys. Chem. C*, 122(14):8031–8036, 2018.

S. Ossinger, H. Naggert, L. Kipgen, T. Jasper-Toennies, A. Rai, J. Rudnik, F. Nickel, L. M. Arruda, M. Bernien, W. Kuch, R. Berndt, and F. Tuczek, "Vacuum-Evaporable Spin-Crossover Complexes in Direct Contact with a Solid Surface: Bismuth versus Gold," *J. Phys. Chem. C*, 121(2):1210–1219, 2017.

F. Nickel, M. Bernien, K. Kraffert, D. Krüger, L. M. Arruda, L. Kipgen, and W. Kuch, "Reversible Switching of Spiropyran Molecules in Direct Contact With a Bi(111) Single Crystal Surface," *Adv. Funct. Mater.*, 27(48):1702280, 2017.

L. Kipgen, M. Bernien, F. Nickel, H. Naggert, A. J. Britton, L. M. Arruda, E. Schierle, E. Weschke, F. Tuczek, and W. Kuch, "Soft-x-ray-induced spin-state switching of an adsorbed Fe(II) spin-crossover complex," *J. Phys.: Condens. Matter*, 29(39):394003, 2017.

List of Publications

F. Nickel, M. Bernien, M. Herder, S. Wrzalek, P. Chittas, K. Kraffert, L. M. Arruda, L. Kipgen, D. Krüger, S. Hecht, and W. Kuch, "Light-induced photoisomerization of a diarylethene molecular switch on solid surfaces," *J. Phys.: Condens. Matter*, 29(37):374001, 2017.

H. Naggert, J. Rudnik, L. Kipgen, M. Bernien, F. Nickel, L. M. Arruda, W. Kuch, C. Näther, and F. Tuzek, "Vacuum-evaporable spin-crossover complexes: physicochemical properties in the crystalline bulk and in thin films deposited from the gas phase," *J. Mater. Chem. C*, 3(30):7870–7877, 2015.

M. Bernien, H. Naggert, L. M. Arruda, L. Kipgen, F. Nickel, J. Miguel, C. F. Hermanns, A. Krüger, D. Krüger, E. Schierle, E. Weschke, F. Tuzek, and W. Kuch, "Highly Efficient Thermal and Light-Induced Spin-State Switching of an Fe(II) Complex in Direct Contact with a Solid Surface," *ACS Nano*, 9(9):8960–8966, 2015.

ACKNOWLEDGMENTS

This thesis would not be possible without the guidance and support of Prof. Dr. Wolfgang Kuch. I am greatly indebted to him and thankful for his kindness and willingness to help his students with his knowledge. It was an incredible pleasure to be a part of his group. Thank you very much for this great opportunity.

Many coworkers were essential in the development of this thesis. Thanks to Matthias Bernien, who was my main source of knowledge in the first years of my PhD, every time I had questions or needed help with some problem in the chamber I went to him. Fabian Nickel was the most important of the more experienced PhD students. He was a great help during beamtimes, and I went to him whenever I couldn't get a hold of Matthias. Yasser Shokr was another one of the more experienced PhD students that has helped me a lot. While we never went to a beamtime together, he was always willing to help at the university with any questions I had. Lalmin Kipgen started this journey almost at the same time as I did and we went through most of it together. Thank you for the partnership, the help, and the discussions. The person I worked most closely with was Andrew Britton in the VEKMAG project. Thank you for going through all the problems with me and figuring out ways to make things work. Marion Badow was a wonderful help with all the intricacies of the PhD daily management and always a very fun person to talk to. Thanks to Uwe Lipowski for the design of several UHV components that are implemented in the VEKMAG. Prof. Dr. Peter Oppeneer and Prof. Dr. Ehesan Ali provided a great contribution with theoretical calculations. Thanks to Prof. Dr. Katharina Franke and members of her group, especially Dr. Nino Hatter, for the STM images. Thank you to all the other members of the group, including Oliver Sandig, Bin Zhang, Jiaming Song, Ismet Gelen, Tauqir Shinwari, Ivar Kumberg, Evangelos Golias, Sangeeta Thakur, Jorge Miguel, Jorge Torres, Rahil Hosseinifar, Karl Frischmuth, Dennis Krüger, and Kai Kraffert. You all deserve some credit for the completion of this work. Thank you to everyone else that I should have mentioned.

Finally, I want to thank my family, whom I have missed tremendously. My father Elmar, my mother Célia, my brother Juliano, and my sister Suzana. Although they were far away during this period, they always sent me their love and support with frequent messages and conversations over the Internet, and much needed words of encouragement. Thank you.

SELBSTSTÄNDIGKEITSERKLÄRUNG

Hiermit versichere ich, die vorliegende Dissertation eigenständig und ausschließlich unter Verwendung der angegebenen Quellen und Hilfsmittel angefertigt zu haben. Die vorliegende Arbeit ist in dieser oder anderer Form zuvor nicht als Prüfungsarbeit zur Begutachtung vorgelegt worden.

Berlin, den

Lucas Machado Arruda